Ana Carolina Gonçalves Seabra

Development and characterization of a miniaturized ultrasound transceiver to measure blood pressure

Development and characterization of a miniaturized ultrasound transceiver to measure blood pressure

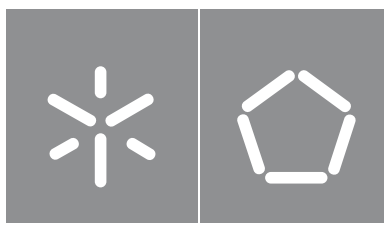Ana Carolina Gonçalves Seabra

UMinho | 2021

Erasmus+

outubro de 2021

Universidade do Minho
Escola de Engenharia

Ana Carolina Gonçalves Seabra

Development and characterization of a miniaturized ultrasound transceiver to measure blood pressure

DIREITOS DE AUTOR E CONDIÇÕES DE UTILIZAÇÃO DO TRABALHO POR TERCEIROS

Este é um trabalho académico que pode ser utilizado por terceiros desde que respeitadas as regras e boas práticas internacionalmente aceites, no que concerne aos direitos de autor e direitos conexos.

Assim, o presente trabalho pode ser utilizado nos termos previstos na licença abaixo indicada.

Caso o utilizador necessite d permissão para poder fazer um uso do trabalho em condições não previstas no licenciamento indicado, deverá contactar o autor, através do RepositóriUM da Universidade do Minho.

Licença concedida aos utilizadores deste trabalho

ACKNOWLEDGEMENTS

I would like to thank Prof Dr-Ing Thomas Stieglitz for offering me this research challenge as an ERASMUS master thesis, welcoming me to the chair, and taking the time to grade this work.

Most of this work's success is due to Belén's top-level guidance and constant support throughout the project. This has been an exponential learning and research experience. It would have been very difficult without the many hours of discussion and feedback.

Although in a different country, Prof Alexandre was an invaluable asset at every meeting. His outside view provided a refreshing perspective that was and continues to be very much appreciated. I welcomed every recommendation he made and take much pride in being one of his students.

Of course, all the BMT crew and the lovely work environment made it very easy to adjust to a new country and scientific setting. Every day was and continues to be a laugh and I couldn't wish for a more supportive group. Out of the BMT crew, I would like to say the last months would not have been as sane as they were without Sira, my borrowed thinktank buddy. The days were long, the months felt short, but even "slow progress is progress". I appreciate our glass wall.

And to my longest-lasting thinktank buddy, who heard me talk about pressure on a daily basis and prevailed – I'll be there for you too, also with homemade cookies, loads of coffee and ready to theorize.

I am also very, very grateful for the existence of pretzels, much of the work here was done after one or two were gulped down.

Lastly, I would like to thank my parents for all the support throughout my academic path (and life). And my siblings, even though they are not as nice as me. This is all thanks to you.

STATEMENT OF INTEGRITY

I hereby declare having conducted this academic work with integrity. I confirm that I have not used plagiarism or any form of undue use of information or falsification of results along the process leading to its elaboration.

I further declare that I have fully acknowledged the Code of Ethical Conduct of the University of Minho.

RESUMO

Actualmente, as doenças cardiovasculares são das mais proeminentes, sendo vital uma monitorização contínua da pressão arterial, acessível a todos, não invasiva e confortável. Um dispositivo de alta precisão, usado à volta do pulso, capaz de derivar a pressão arterial a partir de curvas de parâmetros arteriais hemodinâmicos, pode ser a chave para a telemonitorização de informação anatómica e funcional da saúde arterial. A utilização da tecnologia de ultrassons é muito promissora como método de medição de tais parâmetros arteriais críticos.

As alterações na forma da onda de pressão ao longo da árvore arterial requerem um modelo de pressão arterial específico para cada local de medição. Este trabalho investiga o melhor método para obter valores de pressão precisos em medições não invasivas, utilizando um sensor de ultrassons incorporado num dispositivo desenhado para uso no pulso. Os modelos de pressão existentes foram analisados e comparados qualitativamente; foram extraídos parâmetros arteriais relevantes (tais como a área luminal e as velocidades do fluxo e da onda de pulso) de 729 indivíduos de uma base de dados simulada que serviram de entrada para os modelos. Neste estudo inovador *in-silico*, o modelo linear foi o mais preciso para a artéria radial.

Foi projectado um sistema electrónico para a aquisição do diâmetro em distensão de um vaso, que toma como princípio de funcionamento o rastreio de eco das paredes internas do vaso. O sinal de eco dos ultrassons é amplificado e filtrado, simplificando o procedimento de pós-processamento; foi, igualmente, desenvolvido um algoritmo específico para extrair a forma da onda do diâmetro do vaso, a partir do sinal de eco de ultrassons, e aplicar a consequente conversão para uma curva de pressão.

O melhor modelo para a artéria radial foi validado *ex-vivo*, na qual foi utilizada uma artéria de porco conjuntamente com o sistema electrónico desenvolvido (amostragem temporal de 0,5 ms). As medições experimentais da pressão *ex-vivo* comprovaram a alta precisão do modelo linear, calibrado com base na pressão arterial média, com valores de erro médio muito baixos de (0,544±2,315) mmHg.

Este estudo realça a necessidade de considerar, para medições de alta precisão, modelos de pressão arterial específicos e adaptados ao local, e introduz a prova de conceito de um dispositivo baseado em ultrassons para medição contínua e não invasiva da pressão arterial.

Palavras-chave: dispositivo desenhado para uso, medição contínua e não invasiva da pressão arterial, modelos de pressão arterial, monitorização da hipertensão, sensor de ultrassons.

ABSTRACT

As cardiovascular diseases are one of the most prominent illnesses, a continuous, non-invasive, and comfortable monitoring of blood pressure becomes indispensable. A highly accurate wrist-worn device that derives the blood pressure curve from hemodynamic pulse waves could be the key for telemonitoring anatomical and functional information about arterial health. The use of ultrasound technology holds great promise as a method of measuring critical arterial parameters.

The changes in the pressure waveform through the arterial tree enforce a site-specific blood pressure model and calibration. This work investigates the best method for obtaining highly accurate blood pressure values in non-invasive measurements when using an ultrasound sensor designed for use via a wrist-worn device. State-of-the-art blood pressure models were analysed and qualitatively compared. Relevant arterial parameters such as luminal area, flow velocity and pulse wave velocity, of 729 subjects were extracted from a computer-simulated database and served as input parameters for the proposed wearable ultrasound device. In the novel *in-silico* study, the linear model was the most accurate at the radial artery.

An electronic system was designed to acquire the distending diameter of a vessel through echo tracking of the inner walls. The ultrasound echo signal was amplified and filtered, simplifying the post-processing procedure. A specific algorithm was developed to extract the diameter waveform from the ultrasound echo signal and consequent conversion to a pressure waveform.

The best model for the radial artery was validated in an *ex-vivo* experiment, where a porcine artery, combined with a heart-like pump, and the developed electronic system (temporal sampling of 0.5 ms) were used. The *ex-vivo* experimental pressure measurements demonstrated the high accuracy of the linear model based on the mean arterial pressure calibration with extremely low mean error values of (0.544 ± 2.315) mmHg.

This study emphasizes the need to consider site-specific blood pressure models and calibration procedures for high accuracy measurements, while also introducing proof-of-concept of an ultrasound-based device for continuous and non-invasive measurement of blood pressure.

Keywords: blood pressure models, continuous and non-invasive blood pressure measurement, hypertension monitoring, ultrasound sensor, wearable device.

TABLE OF CONTENTS

LIST OF FIGURES

LIST OF TABLES

NOMENCLATURE

Formula symbols

Variable	Meaning	Unit
SBP	Systolic blood pressure	mmHg
DBP	Diastolic blood pressure	mmHg
MAP	Mean arterial pressure	mmHg
PP	Pulse pressure	mmHg
FF	Form factor of the pressure waveform	-
CC	Compliance coefficient	$m^2 \cdot Pa^{-1}$
ΔP	Difference in pressure	mmHg
ΔA	Difference in area	m^2
DC	Distensibility coefficient	Pa^{-1}
A	Area	m^2
β	Stiffness parameter	-
D_D	Diameter of the artery at DBP	m
D_s	Diameter of the artery at SBP	m
E_{inc}	Incremental elastic modulus	Pa
h	Vessel's wall thickness	m
ΔD	Difference in diameter	m
ρ	Density	$kg \cdot m^{-3}$
PWV_L	Local pulse wave velocity	$m \cdot s^{-1}$
PWV_R	Regional pulse wave velocity	$m \cdot s^{-1}$
Δt	Time difference	s

Variable	Meaning	Unit
L	Segment length between the two sites	m
$D(t)$	Diameter waveform	mm
$\overline{D}$	Mean arterial diameter	mm
k	Conversion factor	mmHg·m^{-1}
b	y-intercept	mmHg
$A(t)$	Cross-sectional area waveform	m^2
α	Vessel rigidity coefficient	-
A_D	Area of the artery at DBP	m^2
A_S	Area of the artery at SBP	m^2
α_i, α_{i+1}	Iterative rigidity coefficient	-
$P_i(t)$	Iterative pressure waveform	mmHg
$\overline{P_i}$	Mean pressure of $P_i(t)$	mmHg
dR	Infinitesimal variation of the lumen radius	m
dP	Infinitesimal variation of the lumen pressure	Pa
R	Radius of the artery	m
R_D	Radius of the artery at DBP	m
$\overline{P}$	Mean of the waveform pressure	mmHg
P_{end}	Pressure at the end of a cycle	mmHg
r	Pearson's linear correlation coefficient	-
m	Calibrating factor	-
dA	Infinitesimal variation of the lumen area	m^2
Δv	Difference in velocity	m·s^{-1}
f_r	Resonance frequency	Hz

Variable	Meaning	Unit
λ	Wavelength	m
c	Speed of sound	$m \cdot s^{-1}$
f	Frequency	Hz
Za	Acoustic impedance	Rayl
I_r	Reflection coefficient intensity	-
I_t	Transmitted coefficient intensity	-
Za_1	Acoustic impedance of the propagating medium	Rayl
Za_2	Acoustic impedance of the reflecting medium	Rayl
TOF	Time of flight	s
d	Distance	m
a_n	Incident propagating wave at port n	$V \cdot \Omega^{-0.5}$
b_n	Reflected propagating wave at port n	$V \cdot \Omega^{-0.5}$
Z_0	Nominal impedance	Ω
V_n	Voltage at port n	V
Z_n	Impedance at port n	Ω
Γ_n	Reflection coefficient at port n	-
z	Nominalized impedance	-
Z	Impedance	Ω
k_1	Stiffness of small arteries	$g \cdot s^{-2} \cdot cm^{-1}$
k_2	Transition point between larger and smaller arteries	cm^{-1}
k_3	Stiffness of large arteries	-
R	Resistance	Ω
C	Capacitance	F

Variable	Meaning	Unit
w_c	Angular frequency	rad·s^{-1}
$P_{applied}$	Pressure applied in the sensor	psi
V_{out}	Voltage output	V
f_s	Sampling frequency	Hz
f_a	Anti-resonance frequency	Hz
$Z_{null-phase}$	Impedance with zero phase	Ω
G	Gain	-
f_m	Mid-frequency	Hz
Q	Quality factor	-
A_m	Gain at mid-frequency	-

Abbreviations

Abbreviation	Meaning
BoM	Bill of Materials
BP	Blood pressure
CV	Cardiovascular
CVD	Cardiovascular diseases
DI	Distilled
DUT	Device under test
EIMN	Electrical impedance matching network
ISO	International Organization for Standardization
MK	Moens-Korteweg

Abbreviation	Meaning
O	Origin
OC	Open circuit
OpAmp	Operational amplifier
OSL	Open, short and load
PCB	Printed circuit board
PPG	Plethysmography
PRF	Pulse repetition frequency
PTT	Pulse transit time
PUT	Piezoelectric ultrasound transducer
PW	Pulse wave
PWV	Pulse wave velocity
RQ	Research question
rpm	Revolutions per minute
SC	Short circuit
SD	Standard deviation
SNR	Signal to noise ratio
US	Ultrasound
VNA	Vector network analyser

1 INTRODUCTION

This dissertation describes the work developed in the scope of the fifth year of the Integrated Master's in Biomedical Engineering, at the University of Minho, during the academic year of 2020-2021. The project was developed within an annual Erasmus+ programme at the Laboratory for Biomedical Microtechnology, Department of Microsystems Engineering, University of Freiburg, Germany. The partnership between the universities allowed combined supervision of the work by Dr-Ing Ana Belén Amado-Rey and Prof Dr-Ing Thomas Stieglitz from the University of Freiburg, and Prof Dr Alexandre Silva from the University of Minho.

1.1 Motivation and problem statement

Hypertension is the most common cause of cardiovascular diseases (CVD) worldwide. The higher the blood pressure (BP), the higher the risk of damage to the heart and blood vessels in the major organs. Hypertension is known as the "silent killer", because most people might not even show any symptoms, causing around half of all deaths from CVD (World Health Organization, 2021), and remaining the leading cause of death globally, accounting for 10.4 million deaths per year (Stanaway & GBD 2017 Risk Factor Collaborators, 2018). Therefore, the need for a continuous monitoring of BP in daily life is evident. In a clinical context, hypertension can be diagnosed when multiple readings of systolic blood pressure (SBP) and/or diastolic blood pressure (DBP) are above 140 mmHg and 90 mmHg, respectively (Unger et al., 2020). Moreover, the BP waveform presents a wealth of information in the cardiovascular system, providing remarkable insights for CVDs diagnosis and prognosis at an early stage. The gold standard for non-invasive BP measurement is sphygmomanometry at the brachial artery, which besides being uncomfortable when used for long periods due to the periodic inflation and deflation of the cuff, only provides discrete values of SBP and DBP. Contrarily, invasive BP measurement is continuous and accurate but attains a high risk as it requires the insertion of a catheter in the artery of the patient and should only be used in an intensive care unit. The ideal BP sensor for continuous measurement should allow long-term monitoring, be non-invasive, and be easily embedded into a remote healthcare system.

Several sensor-based techniques try to answer the requirements listed above, such as the tonometer method, vascular unloading, plethysmography (PPG), pulse transit time (PTT), and ultrasound (US) echo tracking   (Arakawa, 2018;   Mukherjee et al., 2018;   Peng et al., 2021;   Peter et al., 2014;

Sharma et al., 2017). The tonometer method is based on the measurement of back-force at contact when the device is placed over a superficial vessel, which requires a stiff or bony structure as support. The change in pressure of the flow is measured while the static pressure is applied. Due to the need for accurate positioning over the measuring site, and of controlled force to avoid the occlusion of the blood vessel, a specialist is usually needed to do the measurement. Furthermore, applanation tonometry cannot be applied to obese subjects, as it needs lean skin to avoid cushioning the pressure values. The vascular unloading method relies on a finger PPG sensor that adjusts pressure in a small finger cuff and keeps the optically measured blood flow constant. The varying adjusted cuff pressure can then be correlated to the intra-arterial BP. Continuous measurement of pressure is possible with this method, but the cuff is uncomfortable for long time periods and there is a risk of venous congestion for the patient. PTT is the time it takes for a pulse wave (PW) to travel between two locations of the cardiovascular system. The configuration that gives the most accurate SBP and DBP values is a PTT obtained between an electrocardiogram and a finger PPG. Compared to the previously presented methods, PTT does not need to partly occlude a vessel, but comes with an increase in the system's complexity, as it adds a second PW measuring site (Ding & Zhang, 2019). Assessment of the BP waveform via US technique utilizes a high-speed acoustic probe to capture the pulsation of arteries. On the one hand, echo signals and the Doppler shift principle have been used in this technique to detect the arterial wall displacement and blood flow, which with a mathematical model and signal conditioning reveal good accuracy in arterial measurements and is, therefore, convenient to use. On the other hand, it is necessary to maintain stable contact between the probe and the measuring site to achieve a reliable acoustic coupling interface (Mukherjee et al., 2018). Taking the indicated advantages and disadvantages into account, the US-based method is feasible in most vascular sites and it is also cost-effective. US is highly promising as indirect, non-invasively, continuous, and comfortable means of obtaining arterial pressure waveforms, when a stable acoustic coupling is achieved.

Every method records a PW that can be translated to BP through a calibration procedure. Up to now, non-invasive standard BP measurements for extraction of the calibration values are performed in the brachial artery with a cuff. Although DBP and mean arterial pressure (MAP) do not change significantly through the arterial tree (Pauca et al., 2001), it is known that the pressure waveform changes at each artery. Intra-radial BP can present differences higher than 15 mmHg in comparison to the intra-brachial BP (Armstrong et al., 2019). Use of calibration values taken from a different artery (i.e., brachial artery)

than the artery under study (e.g., radial artery) is generally accepted but leads to inaccurate readings and wrong clinical prognoses.

Although US echo tracking has been studied as a method for measuring BP non-invasively, there is no standard mathematical model that takes as input the arterial wall displacement and/or blood flow and transforms it into a pressure reading. Over the years, different BP models have been proposed that relate hemodynamic pulse waves to pressure through mathematical formulas, from simple to complex transformations. Never before has a comparison study between BP models been made, or analysis of the models at different arterial sites.

BP is one of the fundamental vital parameters for health assessment. However, non-invasive BP measurement is still based on the sphygmomanometer method, and continuous BP measurement must rely on invasive approaches with catheters. The development of a non-invasive, continuous, wrist wearable device for the measurement of BP is a complex endeavour due to the high specificity of the pressure waveform at each measuring site and the need for highly accurate measurements.

1.2 Goals and research questions

This thesis aimed to design and develop a prototype of a wrist-worn device that would allow a continuous, non-invasive, comfortable and highly accurate measurement of BP. As it is a proof-of-concept, the feature of being wrist-worn solely focus on projecting the design to the radial artery (wrist artery). This work proposes the use of a US approach as a non-invasive method to measure BP continuously, which lies in the correlation of hemodynamic arterial changes, such as diameter distension and blood flow velocity, with BP. Considering the validity of the previous statement and bearing in mind that the pressure waveform changes through the arterial tree, the following hypothesis emerges: can an electronic system be developed to measure BP through this approach? To achieve the main goal and validate the hypothesis, the following Research Questions (RQs) were identified and researched:

- RQ1: How to indirectly measure BP through US at the wrist? As it is known that the BP waveform changes through the arterial tree, the need for a site-specific model is evident. The first RQ is addressed in Chapter 3, and its discussion is focused on three topics:
    - How site-specific are the BP models?
    - Which are the limitations of the models?
    - What is the standardization status for a mathematical-model-based BP device?

- RQ2: What are the necessary characteristics of an electronic system, in order to implement the BP model in the measuring device? After determining the best model at the radial artery (wrist artery) and defining the working principle of the proposed device, the second RQ is approached in Chapter 5.

- RQ3: How to validate the system in a preliminary approach? The task of validation is addressed in Chapter 6.

1.3 Methodology

This work introduces a pilot study for the measurement of continuous and non-invasive BP at the radial artery through a site-specific BP model that correlates hemodynamic properties (measured with US) to BP. The methodology employed in this work is described in Figure 1.1. The developed system aims to demonstrate the feasibility of the approach.
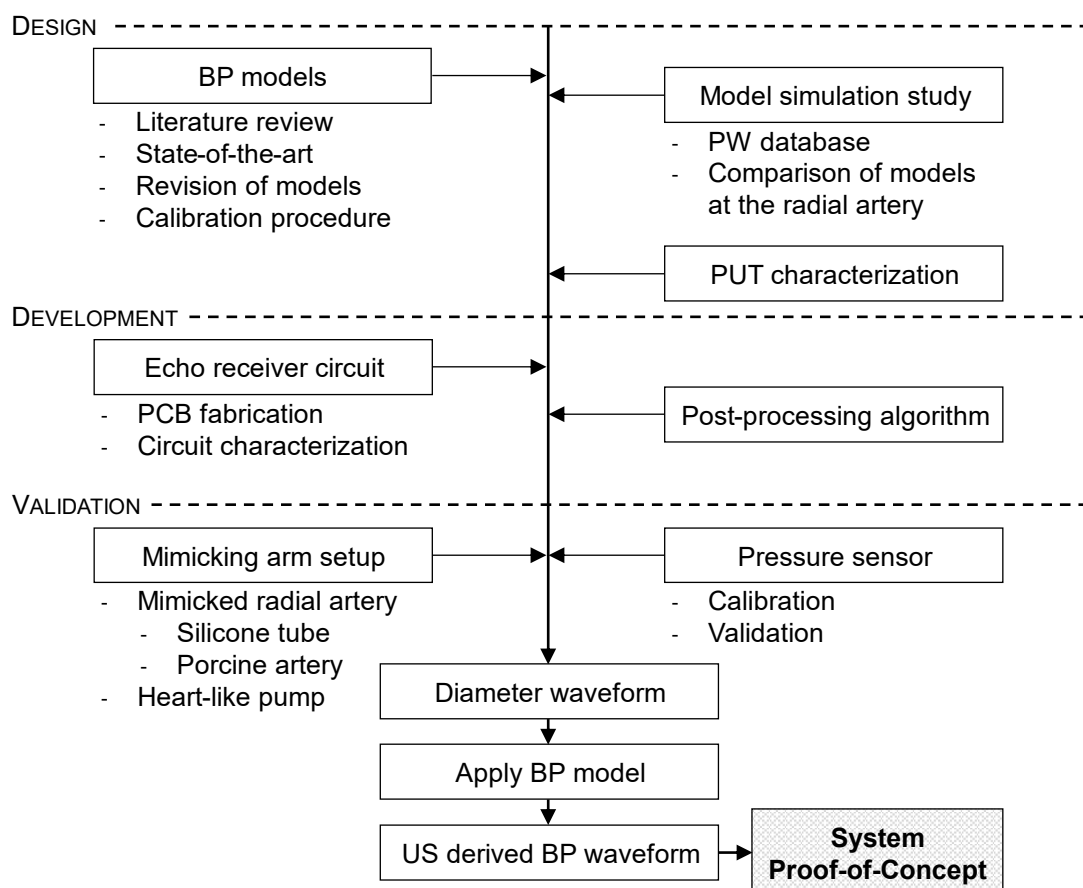
Figure 1.1: Methodology of the work. The US derived BP waveform is achieved by selecting the best BP model at the radial artery and the development of an electronic system and specific post-processing algorithm for the measurement of the diameter waveform of a vessel. System proof-of-concept is achieved through validation in a mimicking arm setup.

First, the best blood pressure model at the radial artery was determined, and therefore assessing how to indirectly measure BP indirectly and non-invasively. This work performs an analytical analysis and comparative study between different models based on their physical principles, with their assumptions and simplifications explained. A computer-simulated arterial PW database (Charlton et al., 2019) was used to demonstrate how the pressure values vary between different arteries and to compare the response to the models at different measuring sites. In the *in-silico* study, the accuracy of the different mathematical models applied to the radial artery was investigated through parameters derived from the database. At this stage, the RQ1 has been answered.

Second, an electronic system was developed to measure a vessel's diameter waveform through US. The system includes a previously fabricated piezoelectric ultrasound transducer (PUT) and a custom-made echo receiver circuit. The received echo signals were amplified and filtered by the circuit, which provided an easier calculation and post-processing. The development of the signal conditioning electronic circuit addresses RQ2. A specific algorithm was constructed for the determination of time of flight (TOF) between the maximum of the echoes of each inner vessel wall and consecutive diameter calculation. With the diameter waveform determined, the best BP mathematical model at the radial artery is applied and a pressure waveform is calculated.

Third, a similar physiological environment to the body was implemented for testing the system. Three mimicking arm setups were developed, and the final proof was done with a porcine artery as a mimicked radial artery. A centrifugal pump was introduced to simulate the pumping of the heart. Additionally, a commercial piezoresistive pressure sensor was introduced in the setup for calibration, comparison, and determination of the accuracy of the measurements. The design of the arm phantoms and testing setup undertakes the approach to RQ3.

Fourth, validation of the concept was performed. The distending diameter of the mimicked radial artery was measured through the US-based method. The best BP model was applied to the diameter waveform, deriving a pressure waveform. Analysis of the results determine the validity of the initial hypothesis: can an electronic system be developed to measure BP through this approach? As there are no standardized protocols for device validation regarding model use, a comparison of results was made to the ISO standard for automated sphygmomanometers.

1.4 Contribution to knowledge

In this work, a literature review and comparative study of the different mathematical models that correlate blood flow and/or artery distension with the BP waveform is carried out. A custom ultrasound transceiver is studied, and the signal conditioning system, including the analogue circuitry and signal post-processing, are developed and characterized. Validation of the best performing model and the developed acquisition system is accomplished by experimental studies with a silicone (*in-vitro*) and a porcine artery (*ex-vivo*). Both approaches are analysed and compared, and important conclusions are extracted. In this thesis, the challenges of how to develop an accurate wrist device to monitor blood pressure are investigated, from which new insights into blood pressure measurements are formulated. Therefore, the main contributions of this dissertation to knowledge are:

- Novel analysis and comparison of the different blood pressure models at the carotid, brachial and radial artery in a variable dataset.

- Development of a site-specific approach for the measurement of BP at the radial artery.

- Design, development, and characterization of an electronic system that enables US echo-tracking of a vessel's inner walls.

- Design and analysis of an algorithm for the calculation of the distending diameter of a vessel.

- Design and development of an arm phantom.

- Proof-of-concept of a non-invasive, continuous and highly accurate wearable device for the measurement of BP.

1.5 Publications

The research performed during this dissertation contributed to the following article papers:

Amado-Rey, A. B., Goncalves Seabra, A. C., Becker, F. J., Fournelle, M., & Stieglitz, T. (2021). Extraction of Radial-Artery Strain and Stiffness by using Non-invasive Ultrasound and a Low-Power Peak Detector. *IEEE Sensors Letters*, *5*(8), Article 7002904. https://doi.org/10.1109/LSENS.2021.3096640

- See Appendix A1.1 for more information.

<u>Gonçalves Seabra, A. C.</u>, Da Ferreira Silva, A., Stieglitz, T., & Amado Rey, A. B. (2021). Blood Pressure Models for Wearable Sensors. Article currently under review for *IEEE Sensors J.*, submitted on 06.08.2021, pre-published at TechRxiv. https://doi.org/10.36227/techrxiv.15073383.v2

- See Appendix A1.2 for more information.

1.6 Thesis outline

This dissertation is organized into 7 chapters, as follows:

- Chapter 2 introduces the theoretical fundamentals necessary during the developed work. First, insights into cardiovascular physiology are presented. Second, state-of-the-art of BP models is performed, with each calibration procedure clarified. Third, fundamentals of US propagation, the pulse-echo technique and diameter assessment is presented. Fourth and last, essential electrical circuit characterization at high frequencies is introduced.

- Chapter 3 describes the comparative study of the different mathematical models in a variable simulated database. In this chapter, the best BP model at the radial artery is determined and the working principle of the device is theorized.

- Chapter 4 introduces the characterization of the custom PUT used as the sensory element during this work. Additionally, the design and characterization of an electrical impedance matching network are included.

- Chapter 5 depicts the design and characterization of the echo receiver circuit developed for conditioning the raw US echo signals into the desired signal for post-processing.

- Chapter 6 begins with defining the pressure acquisition setup. First, the ultrasound sensor complex, the signal acquisition protocol, and the offline post-processing algorithm that make up the setup are described. Second, the results are presented. Third and fourth, an individual analysis of the diameter and pressure acquisition is introduced. Last, the offline post-processing algorithm is discussed.

- Chapter 7 concludes this dissertation, with final remarks, the answer to the initial hypothesis, and proposals on how to improve the developed system, the outlook of this project, and BP research.

2 FUNDAMENTALS

In this chapter, essential terminology, and a clarification of topics necessary to understand the methodology of this work are introduced. First, a description of the blood pressure waveform, its propagation through the arterial tree and the vessel's hemodynamic properties are made. Second, state-of-the-art blood pressure models are presented and analysed. Third, the fundamentals of a PUT and its working principle are covered. Fourth, circuit characterization at high frequencies (range in which ultrasounds for medical diagnostic are transmitted) is approached.

2.1 Fundamentals of the cardiovascular physiology

This section provides a foundation to understand the basics and the propagation of arterial pressure through the body.

2.1.1 Arterial pressure waveform

The arterial pressure waveform is the result of the dynamic interactions between the volume of blood ejected by the left ventricle through the aortic valve and to the aortic artery, and it is influenced by many important cardiovascular factors such as the pulse rate, the artery and blood composition, the distensibility of the vessel and also the velocity at which the blood travels through the arterial tree (Nirmalan & Dark, 2014). The BP curve presents a characteristic waveform with three main parts, as depicted in Figure 2.1:

i. *Systolic phase.* This phase begins when the aortic valve opens, and blood is ejected from the left ventricle into the aorta. It is characterized by a rapid increase in pressure, followed by a rapid decrease. The arteries expand and store an amount of blood (increase in pressure) until blood starts to be driven forward at a higher rate than the influx from the ventricle (decrease in pressure). The pressure peak corresponds to the SBP.

ii. *Dicrotic notch.* The meaning of the notch depends on the position in the arterial tree where the pressure waveform is being measured. When the pressure is measured close to the heart, it represents the closure of the aortic valve and precedes a secondary dicrotic wave (Esper & Pinsky, 2014; Ewy et al., 1969). When measurements are taken towards the periphery, the notch is associated with several reflected waves.

iii.   *Diastolic phase.* The arterial vessels recover their resting diameter and drive the remaining blood to peripheral arteries. This phase is characterized by a continuous pressure downstroke until the end-diastolic pressure, generally nominated DBP.
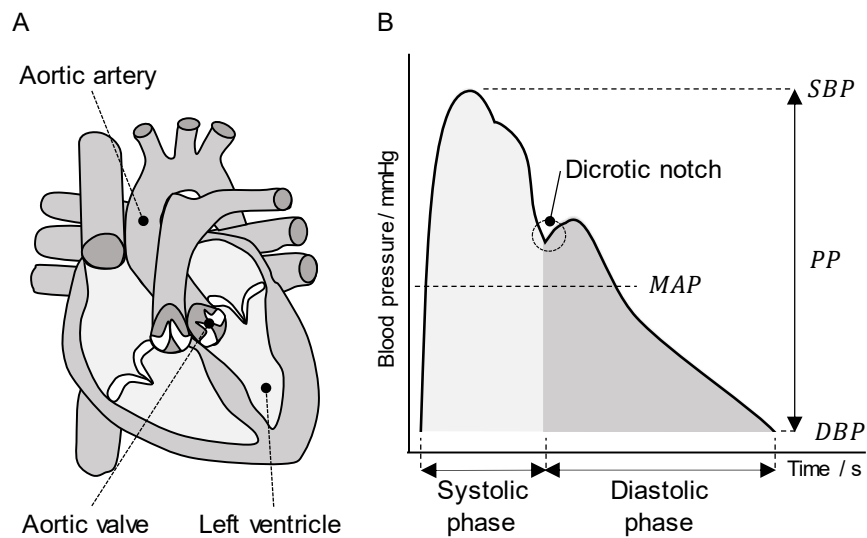
Figure 2.1: Illustration of the heart and of the blood pressure waveform. (A) The left ventricle, aortic valve and aortic artery are indicated in the heart illustration (adapted from (Mtcv, 2008), licensed under CC BY-SA 3.0). (B) The pressure waveform is divided into two phases (systolic phase and diastolic phase) by the dicrotic notch. SBP, DBP, MAP and PP (pulse pressure) are also indicated.

Blood pressure measurements are expressed in mmHg and are represented by three values, SBP, DBP and MAP. Additionally, pulse pressure (PP) is derived from the difference between SBP and DBP (Equation 2.1).

$$PP = SBP - DBP \qquad (2.1)$$

The MAP is determined by integrating the pressure waveform during a cardiac cycle and relates PP to DBP through the "form factor" (FF) ratio. MAP can be estimated by Equation 2.2.

$$MAP = FF \cdot PP + DBP \qquad (2.2)$$

As the blood pressure waveform changes through the arterial tree, the wave's FF should be site-dependent (Westerhof et al., 2010). In recent studies, a form factor of 0.412 has been proved to derive more accurate MAP values (Kiers et al., 2008; Mahieu et al., 2010; Papaioannou et al., 2016). However, the classic form factor (FF=0.3) is generally accepted in the medical community and is widely used for MAP estimation.

2.1.2 Propagation through the arterial tree

The arterial tree is composed of vessels with a viscoelastic behaviour and different elastin/collagen proportions. At the central artery (aorta artery), the main arterial wall is composed of elastin, providing a higher elastic behaviour. Towards the periphery, the collagen to elastin ratio increases, becoming the predominant component in peripheral arteries (e.g., brachial, femoral and radial artery), and increasing the vessel's stiffness (Harkness et al., 1957; Tucker et al., 2021). Furthermore, due to the reflection phenomenon and non-constant vessel resistance, the shape of the pressure waveform changes through the arterial tree and is amplified as it moves away from the heart. Reflected waves are created at bifurcations and arterial resistance mismatch sites. The reflected waves return in the opposite direction, resulting in a backwards flow (reflected wave), adding to the forward pulses, and amplifying the signal. The amplification is higher at the periphery, due to the higher amount of bifurcations and stiffer arteries (Koelwyn et al., 2012). Additionally, it is worth noting that DBP and MAP remain almost constant through the arterial tree (Pauca et al., 2001).

2.1.3 Hemodynamic properties of the vascular system

The viscoelasticity of the arterial wall is determined by the stress/strain relationship. Stress is the internal resistive force to the deformation per unit area, whilst strain is the percentage of deformation and is dimensionless. On one hand, the compliance coefficient (CC) is the variation of lumen area (ΔA) for a given change in pressure (ΔP), as seen in Equation 2.3. The distensibility coefficient (DC), on the other hand, considers the initial dimension of the artery (A) and is known as the relative change in area in response to a change in pressure, as shown in Equation 2.4 (Baltgaile, 2012; Hoeks et al., 1999; Koelwyn et al., 2012).

$$CC = \frac{\Delta A}{\Delta P} \tag{2.3}$$

$$DC = \frac{\Delta A / A}{\Delta P} \tag{2.4}$$

Another important arterial parameter is the stiffness parameter (β), introduced to access the local stiffness (Hayashi et al., 1980; Reneman et al., 2005). The pressure-independent parameter is presented in Equation 2.5, where ΔD is the variation of the vessel's diameter ($D_S - D_D$), D_D and D_S are the artery's diameter at DBP and SBP, respectively.

$$\beta = \frac{D_D \cdot ln(SBP/DBP)}{\Delta D} \tag{2.5}$$

Young's modulus, or incremental elastic modulus (E_{inc}), defined in Equation 2.6, quantifies the vessel's wall stress/strain relationship by also considering the wall thickness (h) (Sun, 2013).

$$E_{inc} = \frac{\Delta P \cdot D_D{}^2}{2 \cdot h \cdot \Delta D} \tag{2.6}$$

Pulse wave velocity (PWV) is the gold standard for the measurement of arterial stiffness (Luc M. van Bortel et al., 2016). The Moens-Korteweg (MK) equation was the first formula introduced to extract the PWV (Bramwell & Hill, 1922), determining the velocity at which the pulse travels through the arterial tree (Equation 2.7, where ρ is the blood density). The formula is site-dependent and is, therefore, used for local PWV (PWV_L) calculation. The stiffness of an arterial segment can be determined by the regional PWV (PWV_R), and is calculated through Equation 2.8, where Δt is the time it takes for a pulse to travel from the proximal to the distal site and L is the segment length (McDonald, 1968).

$$PWV_L = \sqrt{\frac{E_{inc} \cdot h}{D \cdot \rho}} \tag{2.7}$$

$$PWV_R = \frac{L}{\Delta t} \tag{2.8}$$

2.2 Pressure waveform models: State-of-the-Art

US sensors that conform to the wrist wearable device do not record blood pressure directly but indirectly instead, via vessel diameter and blood flow. Thus, pressure models that rely on the measurements of arterial pulses are reviewed.

2.2.1 Model 1 (M1): Linear relationship

The diameter waveform, $D(t)$, can be transformed through a direct conversion to a pressure waveform (Meinders & Hoeks, 2004; L. M. van Bortel et al., 2001). The diastolic and mean arterial diameter, D_D and $\overline{D}$, are calibrated to the brachial DBP and MAP, deriving the conversion factor k shown in Equation 2.9. The diameter waveform is then converted to the pressure waveform $P(t)$ by the

factor k (slope) and the y-intercept b calculated at the diastolic pressure. The linear relationship is described in Equation 2.10.

$$k = \frac{MAP - DBP}{\overline{D} - D_D} \tag{2.9}$$

$$P(t) = D(t) \cdot k + b \tag{2.10}$$

Although a study revealed that this method of assessing BP might, on average, only underestimate invasive PP by only 1.6 mmHg (L. M. van Bortel et al., 2001), this is not expected if the measurement is taken in the periphery. In normotensive subjects, the diameter of elastic arteries changes linearly with pressure, while peripheral arteries exhibit saturation at near-systolic pressure (Hoeks, 1993; Hoeks et al., 1999; Reneman et al., 2005).

2.2.2 Model 2 (M2): Exponential relationship

Many researchers have studied the exponential relationship between arterial diameter distension and BP (Gavish & Izzo, 2016; Hoeks, 1993; Meinders & Hoeks, 2004; Sun, 2013; Wang et al., 2018). It is assumed that the arteries are rotationally symmetrical due to the high transmural pressure, and thus the arterial vessel cross-section area $A(t)$ is obtained from $D(t)$ (Equation 2.11). Consequently, the BP waveform can be calculated by Equation 2.12, where α, calculated through Equation 2.13, is the vessel rigidity coefficient, A_D is the diastolic luminal area and A_S the systolic luminal area.

$$A(t) = \frac{\pi \cdot D(t)^2}{4} \tag{2.11}$$

$$P(t) = DBP \cdot e^{\alpha\left(\frac{A(t)}{A_D} - 1\right)} \tag{2.12}$$

$$\alpha = \frac{A_D \cdot ln\left(SBP/DBP\right)}{A_S - A_D} \tag{2.13}$$

To accurately determine α, it is worth noting that SBP and DBP must be obtained at the same location as the diameter waveform. If SBP and DBP are unknown, brachial sphygmomanometer measurement could be done. Researchers at the Massachusetts Institute of Technology (Massachusetts, USA) designed an ultrasonic device that uses the brachial calibration method with a measurement precision higher than 2 mmHg (Wang et al., 2018). However, it is known that SBP changes drastically through the arterial tree

(differences can reach 15 mmHg between the brachial and radial artery) due to arterial stiffening and wave reflection phenomenon. Therefore, brachial SBP should not be used for calibration in other measuring sites, especially if changes between systolic pressures are expected, as is the case between the brachial and radial artery (Armstrong et al., 2019).

To deal with this issue, an iterative correction of α was proposed by researchers at the Maastricht University (Maastricht, The Netherlands) (Meinders & Hoeks, 2004). For the first iteration, the rigidity coefficient, α_i with i=1, is calculated as indicated in Equation 2.13, where SBP and DBP correspond to brachial SBP and DBP. After determining $P_i(t)$, the measured mean pressure $\overline{P_i}$ is compared to the MAP determined at the brachial artery. If $|\overline{P_i} - MAP|$ is higher than 0.01 mmHg, a new α_{i+1} is calculated until the mean pressure of the extracted waveform converges to brachial MAP. The iterative α_{i+1} is calculated by Equation 2.14.

$$\alpha_{i+1} = \alpha_i \cdot \frac{MAP}{\overline{P_i}} \tag{2.14}$$

2.2.3 Model 3 (M3): Laplace's law + Moens-Korteweg equation

An US-based method for the assessment of the blood pressure waveform built on the integration of pressure over the cardiac cycle was introduced by researchers at Columbia University (New York, USA) (Vappou et al., 2011). This technique relies on the measurement of local distension waveforms using US signals, together with the extraction of PWV leading to an estimation of the local stiffness. The theoretical principle combines Laplace's law and MK equation (Equation 2.7). As indicated in Equation 2.15, Laplace's law relates an infinitesimal variation of the lumen radius (dR) to the variation of internal fluid pressure (dP), where R is the artery's luminal radius.

$$dP = \frac{E_{inc} \cdot h \cdot dR}{R^2} \tag{2.15}$$

By replacing the elasticity factor in Equation 2.15 with E_{inc} calculated from Equation 2.7 (MK equation), and integrating it over the cardiac cycle, the pressure waveform is obtained (Equation 2.16), where $\Delta P = P(t) - DBP$, and R_D corresponds to the diastolic value of artery radius. As in most indirect BP measurement models, the methodology (Vappou et al., 2011) only determines the ΔP, with DBP unknown. A conversion to absolute BP measurement is done by adding the DBP measured at the brachial artery to the ΔP calculated in Equation 2.16.

$$\Delta P = 2\rho \cdot PWV_L{}^2 \cdot log\left(\frac{R(t)}{R_D}\right) \tag{2.16}$$

In the study (Vappou et al., 2011), a linear waveform calibration to brachial DBP and MAP was proposed. The calibration procedure takes the model's mean pressure $\bar{P}$ (integrated over a cardiac cycle) and P_{end} (pressure at the end of the cardiac cycle), to calculate the calibration factor, m, as shown in Equation 2.17. The pressure waveform is then multiplied by the calibration factor, and the y-intercept b (calculated for $P(t) = MAP$) is added.

$$m = \frac{MAP - DBP}{\bar{P} - P_{end}} \tag{2.17}$$

In a study with 11 subjects (Vappou et al., 2011), a very strong linear positive correlation of 0.94<r<0.98 and a Bland-Altman positive bias of (4.70±4.45) mmHg were found between the PP measured through radial tonometry using a commercially available system and the PP obtained through the method described above.

2.2.4 Model 4 (M4): Bramwell-Hill equation

Professor of medicine and cardiologist, Dr Bramwell improved the MK equation such that the formula is independent of Young's modulus E_{inc} and thickness h of the vessel wall, inversely relating PWV_L to the compliance dA/dP as shown in Equation 2.18 (Bramwell & Hill, 1922).

$$PWV_L = \sqrt{\frac{A(t) \cdot dP}{\rho \cdot dA}} \tag{2.18}$$

By rearranging Equation 2.18 and assuming that PWV remains relatively constant during a cardiac cycle, the pressure waveform can be expressed in terms of PWV_L and change in cross-sectional area, as indicated in Equation 2.19 (Seo et al., 2015).

$$\Delta P = \rho \cdot PWV_L{}^2 \cdot ln\left(\frac{A(t)}{A_D}\right) \tag{2.19}$$

It ought to be noted that the PWV_L in Equation 2.19 is dependent on the compliance and area of an artery and it should be determined at the site of diameter distension measurement. The same calibration procedure as in M3 was applied in this model.

2.2.5 Model 5 (M5): Joukowsky's equation + PWV

A different BP model, developed by researchers at the Tarbiat Modares University (Tehran, Iran), assumes that blood is an incompressible fluid travelling through a flexible tube and that pressure can be determined through the fundamental water hammer phenomenon (Soleimani et al., 2017). Consequently, the water hammer principle was extrapolated to the arterial vascular system, where the opening and closing of cardiac valves correspond to mechanical valves in a hydraulic piping system. The water hammer equation, known as Joukowsky's equation and presented in Equation 2.20, measures the change in pressure of a fluid as a result of the variation in the fluid's velocity. Equation 2.20 considers the blood's density and local PWV, in which ΔP and Δv are changes in pressure and velocity, respectively, relative to the initial value.

$$\Delta P = \rho \cdot PWV_L \cdot \Delta v \qquad (2.20)$$

By solving Equation 2.20 with Equation 2.18, and applying the increment of pressure and area instead of its derivative, the pressure waveform M5 is obtained in Equation 2.21.

$$\Delta P = \rho \cdot (\Delta v)^2 \cdot \frac{A(t)}{\Delta A} \qquad (2.21)$$

The brachial DBP is then added to the measured pressure and the absolute blood pressure is determined. The researchers (Soleimani et al., 2017) developed a subject-specific calibration procedure based on the correlation between $\bar{P}$ calculated from the proposed model and $\bar{P}$ calculated from tonometry measurements at the radial artery. The calibrated model was validated on 20 male subjects via a standard sphygmomanometer, revealing a PP linear correlation of 0.91 and mean absolute difference of (1.333±6.548) mmHg.

2.2.6 Comparison between models

It is worth noting the similarities between models M3 and M4. Both Equation 2.16 and Equation 2.19 are derived from the Bramwell-Hill equation that relates the MK equation to Laplace's Law. However, when integrating over a cardiac cycle, M3 (Vappou et al., 2011) is applied with the decimal logarithm, whilst the direct integration of the Bramwell-Hill equation applies the natural logarithm. Although it is expected that both models produce similar responses, the raw, non-calibrated BP values derived from Equation 2.19 are higher than the ones obtained from Equation 2.16. The differences between M3 and

M4 are non-existent after applying the corresponding MAP and DBP calibration, where both calibrated models exhibit the same curve and are equivalent. Therefore, from here on, M3/4 refers to both calibrated models M3 and M4.

Table 2.1 summarizes the different model equations and the implemented calibration methods. All models were calibrated with brachial DBP and MAP. In M2, the first iteration is additionally calibrated with SBP. Calibrating values DBP, SBP and MAP were taken from brachial sphygmomanometer measurements.

.1: Pressure model equations and calibration procedure.

el eviation	Model name	Equation	Calibration	Ref.
	Linear relationship	$P(t) = D(t) \cdot k + b$	$k = \dfrac{MAP - DBP}{\overline{D} - D_D}$	(Meinders & Hoeks, 2004)
	Exponential relationship	$P(t) = DBP \cdot e^{\alpha\left(\frac{A(t)}{A_D}-1\right)}$	$\alpha_1 = \dfrac{A_D \cdot ln\left(SBP/_{DBP}\right)}{A_S - A_D};$ $\alpha_{i+1} = \alpha_i \cdot \dfrac{MAP}{\overline{P_i}}$	(Meinders & Hoeks, 2004)
	Laplace's Law + MK equation	$\Delta P = 2\rho \cdot PWV_L{}^2 \cdot log\left(\dfrac{R(t)}{R_D}\right)$	$P(t)$ calibrated to $m = \dfrac{MAP - DBP}{\overline{P} - P_{end}}$	(Vappou et al., 2011)
	Bramwell-Hill equation	$\Delta P = \rho \cdot PWV_L{}^2 \cdot ln\left(\dfrac{A(t)}{A_D}\right)$		(Seo et al., 2015)
	Joukowsky's equation + PWV	$\Delta P = \rho \cdot (\Delta v)^2 \cdot \dfrac{A(t)}{\Delta A}$	correlation between M5 $\overline{P}$ and tonometry $\overline{P}$ at the radial artery	(Soleimani et al., 2017)

P, SBP and MAP calculated from brachial sphygmomanometer.

2.3 Piezoelectric ultrasound transducer

A piezoelectric ultrasound transducer (PUT) generates sound waves from electrical pulses by extensional vibrations of the piezoelectric material or vice versa. The material exhibits its best performance at the resonance frequency, f_r, which is defined by the thickness of the transducer.

A generic PUT consists of three main components: *(i)* a piezoelectric material, the functional block of the PUT where the electro-mechanical energy conversion occurs, *(ii)* a matching layer situated in front of the piezoelectric material, responsible for efficient sound transfer and reduction of the reflections between the interface of the transducer and the surrounding medium, and *(iii)* a backing material applied to the back of the piezoelectric plate, which acts as a damping block for the back-propagating ultrasound waves and can be adjusted for a broader bandwidth (Jensen, 1986).

The acoustic impedance matching provided by the matching layer increases the electrical impedance, which results in a mismatch between the transducer and the interface device and causes waveform degradation and loss in signal. However, the mismatch can be minimized by electrical impedance matching between the probe and receiving device, leading to an increment in the energy transmission (Rathod, 2019).

In medical diagnostic at arm arteries, a frequency range between (5-10) MHz is the most appropriate (Schäberle, 2011). The axial resolution, along the beam axis, is determined by the product of wavelength and the number of waves sent on each pulse (Ng & Swanevelder, 2011; Rumack, 2005). The relation between the wavelength, λ, wave propagation velocity, c, and the frequency, f, is given by Equation 2.22. A higher frequency, and therefore, lower wavelength, provides a better resolution. A constant sound velocity of 1540 m/s in soft tissues can be assumed, as it is commonly done in medical US applications (Feldman et al., 2009).

$$\lambda = {}^c\!/_f \qquad\qquad (2.22)$$

2.3.1 Ultrasound propagation

An ultrasound wave travelling through a body is affected by physical processes which depend on two acoustic wave characteristics: the medium in which it travels and the boundaries of the medium. Every tissue has a specific acoustic impedance, Za, equal to the product of the speed of sound and density of the medium (examples of acoustic impedances in Appendix A1). Wave reflection and refraction occurs at

an acoustic interface. For normal incidence, the intensity of the reflection coefficient, I_r, and the transmitted (refracted) coefficient, I_t, are given by Equation 2.23 and Equation 2.24, respectively, where Za_1 is the acoustic impedance of the propagating material and Za_2 is the one of the reflecting material. If $Za_2 > Za_1$, the reflected wave is in phase with the incident wave and the interface is termed "hard boundary"; if $Za_2 < Za_1$, a reflection happened at a "soft boundary" and the reflected wave is 180° out of phase (Dukhin & Goetz, 2010). Furthermore, the US wave is attenuated as it propagates through the body, namely by the conversion of energy to heat, a process called absorption. The US wave is attenuated in body tissues at an average rate of 1 dB/mHz/cm, with a much larger impact at high frequencies than at low frequencies (Schäberle, 2011).

$$I_r = \frac{(Za_2 - Za_1)^2}{(Za_2 + Za_1)^2} \qquad (2.23)$$

$$I_t = \frac{4Za_2 \cdot Za_1}{(Za_2 + Za_1)^2} \qquad (2.24)$$

2.3.2 Pulse-echo technique

The pulse-echo technique is the basic methodology for most diagnostic ultrasound procedures. It relies on applying pulsed excitation signals to the PUT, from which an ultrasound wave is generated through the piezoelectric effect. As the beam travels through the body, part of the signal gets reflected to the transducer when it reaches acoustic mismatches. Once again, the piezoelectric effect comes into play by converting the received echoes into electrical signals. The distance d to a reflecting surface is proportional to the speed of sound c and TOF between the transmitted signal and the detection of the reflected echo. As the TOF includes the signal's round-trip time, the distance must be divided by the factor 2, as shown in Equation 2.25 (Schäberle, 2011).

$$d = \frac{TOF \cdot c}{2} \qquad (2.25)$$

2.3.3 Diameter assessment

The pulse-echo technique can be used to determine the arterial diameter and its distension waveform. Measurement of a vessel's diameter is commonly done through a B-mode US image (where callipers are manually positioned on the screen and the distance is displayed) or edge-detecting software is

employed (Koelwyn et al., 2012). However, these processes depend on B-mode images' post-processing and do not result in a distension waveform.

By analysing the ultrasound echo signals directly, the distance between the reflections of the vessel's anterior and posterior wall can be calculated and the arterial diameter can be measured (Hoeks, 1993). At the beginning of a measurement, observation windows are positioned at both walls and a point of reference within the windows is used to measure the distance to the probe over time. Subtraction between walls' distances determines the arterial diameter waveform. Different tracking algorithms can be used to determine the point of reference. Its discussion is beyond the scope of this work (for a detailed report refer to (Hoeks, 1993)).

2.4 Electrical circuit characterization

A common method during circuit design and characterization is to treat the device under test (DUT) as a two-port network. The component or subcircuit is seen as a black box where only the input and output ports are accessible, and characterization is made through the relationship between the measured input and output signals.

2.4.1 S-parameters

S-parameters (from *scattering* parameters) are used to describe the dynamic relationship between the input and output signals at the n-ports of a device as a function of frequency (Huang & Bednorz, 2014). The incident (a_n) and reflected (b_n) propagating waves are normalized to the nominal impedance Z_0 (50 Ω), and can be defined as in Equation 2.26, where V_n is the voltage at port n (Tofighi et al., 2017). For a two-port configuration, the scattering matrix can be defined as presented in Equation 2.27.

$$a_n = \frac{V_n^+}{\sqrt{Z_0}} \text{ and } b_n = \frac{V_n^-}{\sqrt{Z_0}}$$
(2.26)

$$\begin{bmatrix} b_1 \\ b_2 \end{bmatrix} = \begin{bmatrix} S_{11} & S_{12} \\ S_{21} & S_{22} \end{bmatrix} \cdot \begin{bmatrix} a_1 \\ a_2 \end{bmatrix}$$
(2.27)

S_{11} and S_{22} are the reflection coefficients of the input and output ports, whilst S_{12} and S_{21} represent the reverse transmission coefficient and forward transmission coefficient of the DUT. A typical two-port network for S-parameters analysis is shown in Figure 2.2.
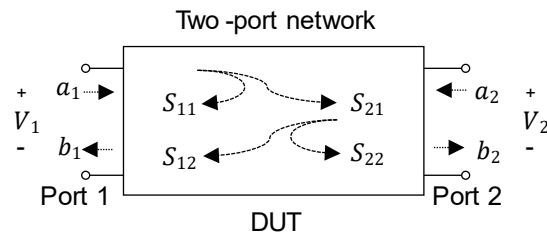
Figure 2.2: A two-port network for S-parameters analysis. Representation of the S-parameters path, the voltage (V_n) and the normalized incident (a_n) and reflected (b_n) waves at port n are indicated.

The port impedance Z_n, which describes the impedance at each port of the DUT over a range of frequencies, can be determined through the nominal impedance and the reflection coefficient (with Z_1, Γ_1, S_{11} for impedance at the input, and with Z_2, Γ_2, S_{22} for impedance at the output), in Equation 2.28 (Huang & Bednorz, 2014).

$$Z_n = Z_0 \cdot \frac{1 + \Gamma_n}{1 - \Gamma_n}$$

(2.28)

The four S-parameters can be measured by a vector network analyser (VNA), which is a device that acquires the phase and gain ratio between two input signals (Poole & Darwazeh, 2015).

2.4.2 Smith chart

The Smith chart represents the complex plane of the reflection coefficient or impedances for a large range of frequencies. The normalized impedance z, determined through Equation 2.29, is defined by its imaginary and real part as $z = r + jx$. If the Smith chart is viewed in terms of impedance coordinates, the normalized impedance is given by the intersection of an $r - x$ circle. In Figure 2.3, a basic Smith chart is shown. In the longitudinal axis are the normalized resistances. An open circuit (OC) happens at (Γ=1, $z\rightarrow\infty$), a short circuit (SC) at (Γ=-1, z=0) and a matched impedance (O) at (Γ=0, z=1). The upper half of the chart is capacitive (impedances' positive imaginary part) and the lower half is inductive (impedances' negative imaginary part). By plotting a frequency-varying reflection coefficient or impedance, an impedance mismatch can be easily perceived. A matched system to the nominal impedance at a specific frequency is plotted at (r=1, x=0) and has no reflections (Poole & Darwazeh, 2015).

$$z = \frac{Z}{Z_0} \qquad\qquad (2.29)$$
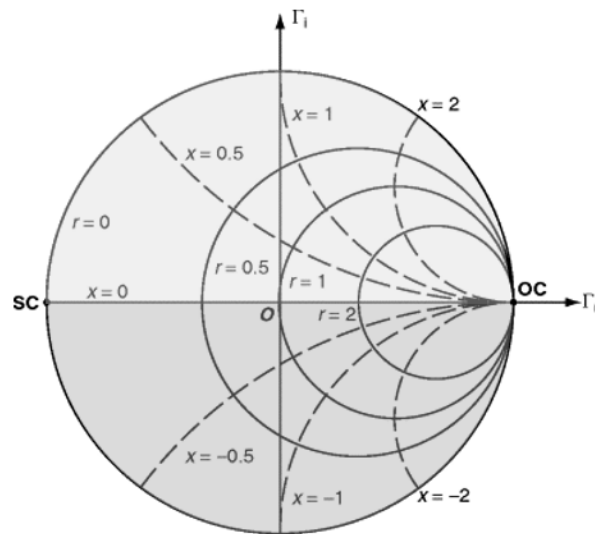
Figure 2.3: Basic construction of the Smith chart. Inductive region ($Im(z)$>0) is represented by a light grey area and capacitive region ($Im(z)$<0) by a dark grey area. Resistance circles (straight line) are plotted with values of r and reactance circles (dashed line) with values of x. SC=short circuit, O=origin/matched impedance, OC=open circuit. Adapted from (W.-K. Chen, 2005).

2.4.3 Electrical impedance matching network

An electrical mismatch causes the reduction of electrical energy and signal to noise ratio (SNR) due to loss in signal amplitude. For maximum power transfer and minimal signal reflection between the source and load, the load impedance needs to be a complex conjugate of the source impedance. Impedance matching can be optimized by introducing an electric impedance matching network (EIMN) between devices, as seen in Figure 2.4. The matching network can be performed through transformers, a shunt capacitor or inductor, or through a simple LC circuit in L-configuration (Rathod, 2019). When using an LC-based network, the components are uniquely determined, whose dimensions depend on the mismatch level and can be manually calculated through extensive mathematical expressions or determined with a computer-aided design method (Rathod, 2019).
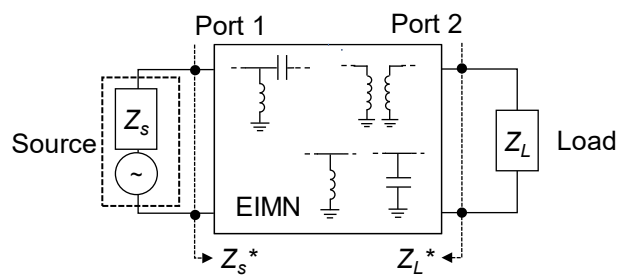
Figure 2.4: Schematic of EIMN examples. Block diagram of a two-port network showing the complex conjugate of source and load impedance with the two ports when using an EIMN.

3 BLOOD PRESSURE MODEL STUDY

To develop a BP device to measure with high accuracy hemodynamic properties via US, a comparison study of different BP models that rely on the measurement of blood flow and/or arterial distension of the arterial segment was implemented. For the benchmarking of the different pressure models, the arterial pulse waves available in the open-source simulated database, developed by researchers at King's College (London, UK) (Charlton et al., 2019), were used as input parameters and as ground truth.

3.1 Pulse wave database description

The open-source database is composed of multiple PWs at different ages (25- to 75-year-olds, 10-year increment) with variable cardiovascular (CV) conditions (e.g., heart rate, stroke volume, arterial diameters), representative of a sample of healthy subjects. The computational model consists of an arterial network simplified in three main steps, based on Dr Alastruey's work (Alastruey et al., 2012). First, the arterial tree is decomposed into arterial segments modelled as thin viscoelastic tubes of constant length and linearly tapered diameter. Then, a periodic inflow waveform is introduced at the aortic root. Third, three-element Windkessel boundary conditions are imposed at the outlets of peripheral arterial segments, modelling vascular beds. The database, composed of 4,374 virtual subjects, was validated by the comparison of PWs and hemodynamic characteristics with *in-vivo* data (Charlton et al., 2019). A visual representation of the pulse wave propagation model and simulated pulse waves is shown in Figure 3.1.

In this work, the primary parameters (flow velocity and luminal area) that can be directly extracted from US measurements were taken from the database and then simulated in the MATLAB® environment (The Mathworks Inc, 2021) for a comparative realistic analysis of the different five models. One of the most important simulations performed consisted of the compliance curves (arterial pressure versus luminal area), as they provide valuable information about the viscoelasticity properties of the arteries. Figure 3.2 shows the compliance curves at the carotid, brachial and radial artery, derived from the baseline of a 25-year-old virtual subject simulated with the age-specific mean values for all CV properties. The viscoelasticity of the arterial walls leads to the hysteresis seen in the compliance curves. As seen in Figure 3.2, there is a change in compliance and relationship between arterial pressure and area through the arterial tree, so that the carotid artery presents an approximately linear behaviour, whilst towards the periphery, in the radial artery, the hysteresis is much more accentuated due to the collagen content.

When performing blood pressure measurements readings with ultrasound in the arterial tree, changes through the different arteries are expected. Therefore, specific models and on-site stiffness coefficients should be applied to each local peripheral artery in the cardiovascular system.
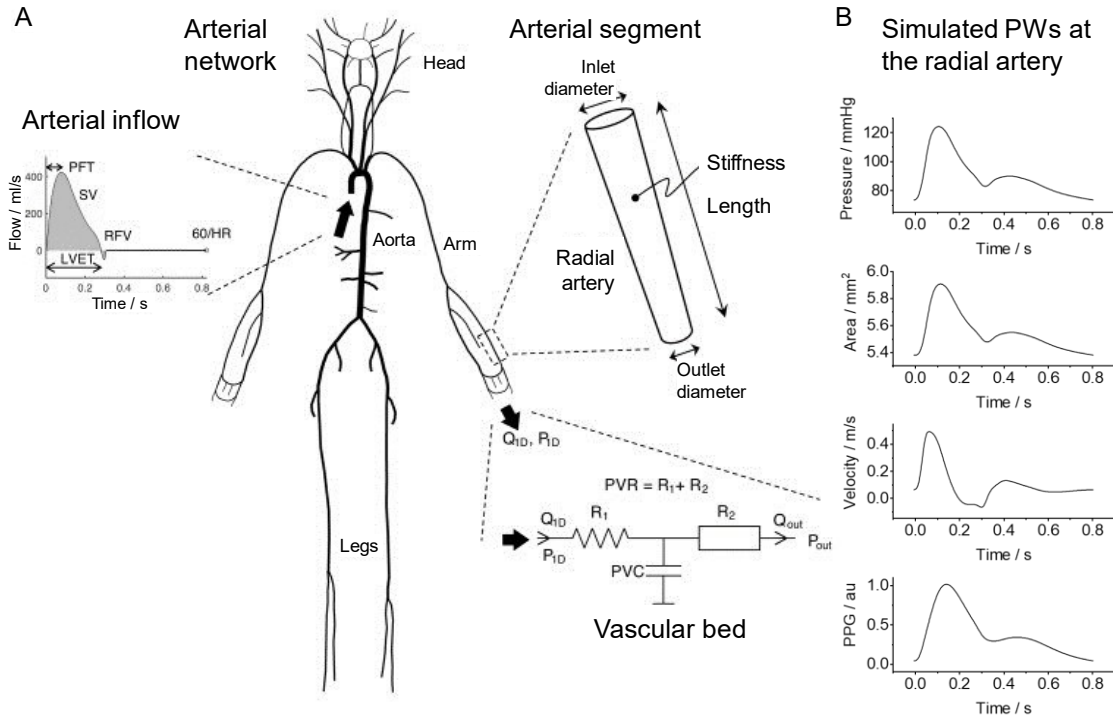
Figure 3.1: Pulse wave database model. (A) The propagation pulse wave model consists of an arterial network composed of arterial segments and linearly tapered diameter, an aortic inflow waveform introduced at the aortic root, and vascular beds at the end of each arterial segment introducing boundary conditions. (B) The simulated pressure, luminal area, flow velocity, and PPG pulse waves at the radial artery for the baseline 25-year-old subject are depicted. Adapted from (Charlton et al., 2019).
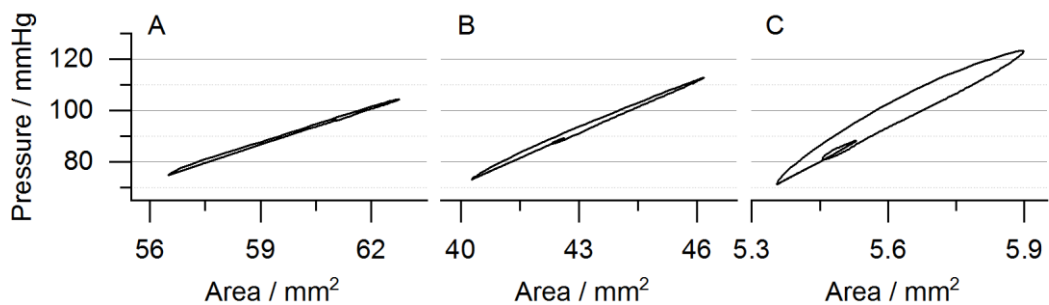
Figure 3.2: Arterial compliance curves towards the periphery. The increase in hysteresis and PP from the carotid artery (A) and brachial artery (B) towards the radial artery (C) due to an increase in arterial stiffness is noticeable.

3.2 Methods

To evaluate and analyse the changes in the hemodynamic parameters in the arterial tree, five BP models (M1, M2, M3, M4 and M5, described in Section 2.2) were studied at three main peripheral arteries: carotid, brachial and radial.

3.2.1 Hemodynamic data extraction

For each measuring site, luminal area PW, in combination with *(i)* PWV_L for M3 and M4, and *(ii)* flow velocity PW for M5, were extracted from the database and applied to each model. Luminal area, flow velocity and pressure PWs were extracted directly from the database for each subject at each arterial site. However, since the database only provided specific segments of PWV values, calculation of the PWV was necessary at the studied sites.

The estimation of the subjects' PWV was based on the description presented in the work of Dr Charlton (Charlton et al., 2019). The diastolic radius, R_D, is related to the incremental elastic modulus, E_{inc}, wall thickness, h, and empirical variables, k_1, k_2 and k_3, through Equation 3.1. In the equation, k_1 determines the stiffness of smaller arteries and was set to $3 \cdot 10^6$ g·s^{-2}·cm^{-1}, k_2 determines the point of transition between larger and smaller arteries and was set to -13.5 cm^{-1} and k_3 determines the stiffness of larger arteries and was calculated by Equation 3.2. PWV was determined by Equation 2.7 with blood density assumed constant and equal to 1,060 kg·m^{-3}.

$$E_{inc} \cdot h = R_D \cdot (k_1 \cdot e^{k_2 \cdot Rd} + k_3) \qquad (3.1)$$

$$k_3 \approx 430{,}118 - 187.3 \cdot age + 244.11 \cdot age^2 \qquad (3.2)$$

3.2.2 Models' calibration procedure

Every model studied has a specific calibration procedure, which is indicated and summarized in Table 2.1. As DBP and MAP do not change significantly through the arterial tree, calibration was made to the simulated brachial DBP and MAP values of each subject (additionally to SBP in the case of M2). The aim of calibrating the curves to the brachial values is to approximate the simulation to a practical situation where calibration of the measured hemodynamic PWs and values would be done using a brachial sphygmomanometer.

The researchers that developed the M5 BP model (Soleimani et al., 2017) proposed a calibration procedure through the correlation between M5 $\bar{P}$ and tonometry $\bar{P}$ at the radial artery over a group of cardiac cycles. However, as the database only consists of a cardiac cycle per subject at each arterial site, the subject-specific calibration was done with the calibration values provided by the researcher's work (Soleimani et al., 2017).

Furthermore, in the sense of maintaining real-life application plausibility, brachial MAP was not calculated from the integration of the BP curve over a cardiac cycle, but through Equation 2.2, which correlates SBP and DBP to MAP. The applied FF was chosen between 0.3 and 0.412 by studying the error of ground truth MAP and FF-derived MAP at the carotid, brachial, and radial artery in the 25-year-old baseline subject.

3.2.3 Models' comparison, analysis, and selection

The hemodynamic data extraction procedure was applied to the 729 virtual 25-year-old subjects available at the database and served as input for the five BP models under study. Model-specific calibration procedures were applied. Next, the resulting models PP were compared and correlated to the ground truth PP, which was extracted from the pressure waveform supplied by the database. At this point, low precision models were discarded, and only the best performing models continued to be studied. Then, error boxplots for SBP, mean BP pulse wave and its standard deviation (SD) were calculated between the models and the database. The overall best performing model at the radial artery was chosen for the device application.

3.3 Results

The selection of the blood pressure model consisted of understanding which is the most accurate model to apply at the radial artery. Every model is calibrated to a MAP brachial reading. Therefore, a study was performed over the MAP FF and its findings were used in each models' calibration procedure. The model selection is then possible.

3.3.1 Mean arterial pressure form-factor study

The pressure waveforms of the 25-year-old baseline subject at the carotid, brachial and radial artery are shown in Figure 3.3, with each MAP indicated by the gold standard, with FF=0.3 and a FF=0.412.
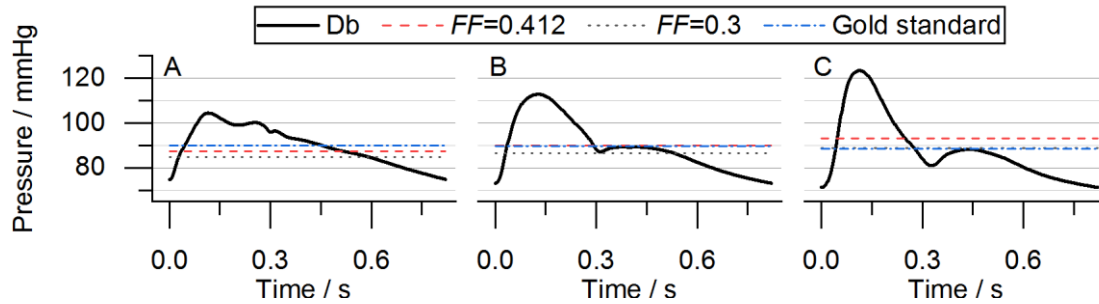
Figure 3.3: Comparison of MAP form factors at different arteries. MAP is derived with a FF of 0.3 (dotted line) and 0.412 (dashed line) and compared with the gold standard (dashed-dotted line, determined through the pressure waveform integration over a cardiac cycle) at the (A) carotid, (B) brachial, and (C) radial artery. The pressure waveforms (Db, straight line) correspond to the baseline subject at each arterial site.

The MAP derived through the gold standard (integration of the pressure curve during one cardiac cycle) at the carotid and brachial artery is around 90 mmHg, whist at the radial artery the mean pressure decreases to 89 mmHg. At the carotid artery, neither of the FFs studied (FF of 0.412 and 0.3) can derive a correct MAP estimation, having both assessments an error higher than 2.5 mmHg. Whilst the commonly used FF of 0.3 estimates a mean pressure at the radial artery with an error lower than 0.1 mmHg, FF=0.412 can derive a MAP at the brachial artery with similar accuracy. Furthermore, an error increment of more than 3.3 mmHg is obtained when using FF=0.3 at the brachial artery or FF=0.412 at the radial artery. As the pressure models' calibration is performed with MAP estimated at the brachial artery (to approximate the calibration to a real-life scenario) a FF=0.421 was selected for calculation of the brachial MAP.

3.3.2 Pressure models' waveform profile

The blood pressure curve of the 25-year-old baseline subject was calculated using the five models previously described. Figure 3.4 shows the performance of the models at the carotid, brachial, and radial artery. Note that after calibration, M3 and M4 exhibit the same waveform and thus only one curve is shown in each graph (curve M3/4).
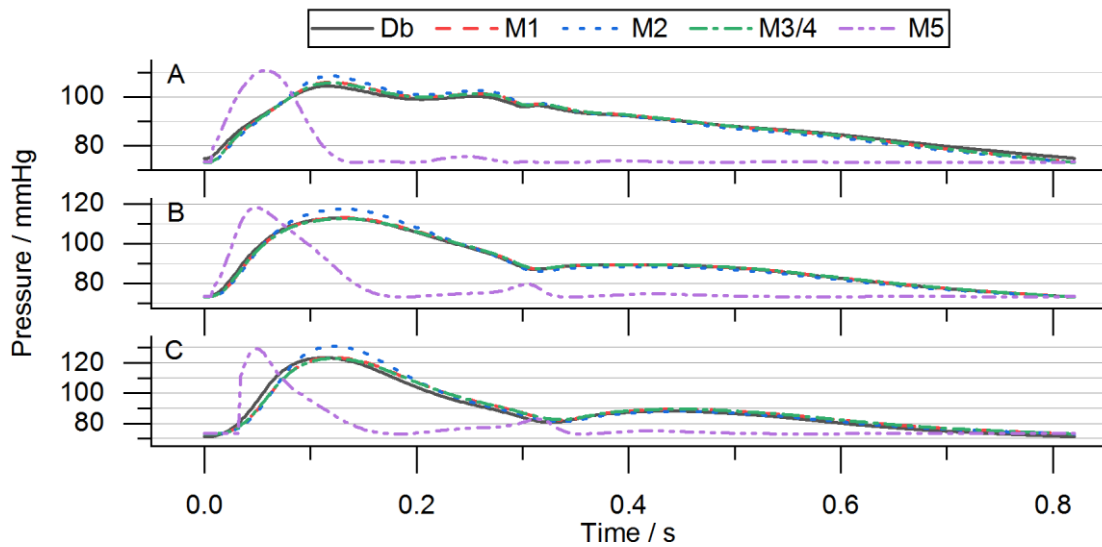
Figure 3.4: BP models performance for the baseline subject. The models were studied at the (A) carotid, (B) brachial, and (C) radial artery. Notice that M1 and M3/M4 overlap. Curve Db (straight line) refers to the pressure waveform from the database and is considered the ground truth.

Except for M5, all models are in good agreement with the pressure waveform from the database. Only a slight underestimation during diastole is appreciated. The waveform profile for M5 is not following the rest of the models, as it is modelled from the blood flow velocity profile, and not only from the arterial distension waveform. Overestimation of SBP (and consequently, PP) is seen in M2 and M5 (SBP overestimation at the radial artery: M2=7.645 mmHg, M5=6.046 mmHg). Due to the calibration procedure done with brachial DBP, underestimation and overestimation of DBP are seen at the carotid artery and radial artery, respectively. An increase in the time delay between the ground truth (the database's pressure waveform) and the models' waveform is seen towards the periphery (time delay at the first ground truth MAP: carotid and brachial artery=4 µs and radial artery=7 µs).

3.3.3 Pressure models' linear correlation

Pearson's linear correlation r and mean difference PPs obtained from the models were compared based on PPs extracted from the database. The results of the study, with a population of 25-year-old subjects (n=729), are included in Table 3.1, Table 3.2 and Table 3.3 at each studied artery. The best results were highlighted in each table.

Table 3.1: Statistical analysis of the models' PP at the carotid artery. Pearson's linear correlation and the mean difference between models' PP and ground truth PP (n=729).

Model abbreviation	r-Pearson	Mean difference (mmHg)
M1	0.979	3.459±1.560
M2	0.970	6.317±1.887
M3'	0.571	-17.758±6.233
M3/4	**0.980**	**3.167±1.558**
M4'	0.571	-1.475±6.238
M5'	0.917	-12.179±3.457
M5	0.917	-7.791±3.459

Table 3.2: Statistical analysis of the models' PP at the brachial artery. Pearson's linear correlation and the mean difference between models' PP and ground truth PP (n=729).

Model abbreviation	r-Pearson	Mean difference (mmHg)
M1	**0.989**	**0.080±1.719**
M2	0.985	4.665±1.511
M3'	0.485	-23.578±7.545
M3/4	**0.989**	-0.428±1.806
M4'	0.485	-1.907±8.053
M5'	0.812	-14.525±5.061
M5	0.812	5.529±5.059

Table 3.3: Statistical analysis of the models' PP at the radial artery. Pearson's linear correlation and the mean difference between models' PP and ground truth PP (n=729).

Model abbreviation	r-Pearson	Mean difference (mmHg)
M1	**0.978**	**-2.134±2.477**
M2	0.969	5.661±2.837
M3'	0.818	-30.665±7.315
M3/4	**0.978**	-2.655±2.572
M4'	0.818	-2.032±5.810
M5'	0.490	-16.318±8.985
M5	0.485	3.853±9.030

As expected, there is a remarkable improvement of the calibrated models in comparison to the uncalibrated models (MX') that is appreciable by the high increment of r. Notice that only uncalibrated M3', M4' and M5' were introduced, as M1 and M2 calibration procedure is intrinsic to the model. In all the measuring sites, M5 is always the least accurate, followed by M2. At the carotid artery, M3/4 exhibits a slightly better performance in r and mean difference, whilst at the brachial and radial artery, the r is the same between models M1 and M3/4. Moreover, when comparing M1 and M3/4 at the radial artery, it is seen that for M1 the mean difference is slightly lower than M3/4. Summarizing, M1 is the best

performing model at the radial artery, revealing a correlation of 0.978 and a mean difference of (-2.134±2.477) mmHg.

3.3.4 Models error study

After rejecting M5 because of its high error and low correlation with the PP extracted from the database, further error studies between the best performing models were completed. DBP and MAP error studies were not introduced, as they display the same error profile between the remaining models because the models were calibrated to the same values (brachial DBP and MAP). The results of the error studies for 729 subjects are depicted in the boxplots in Figure 3.5, where mean PW error, its SD, and SBP error were included.
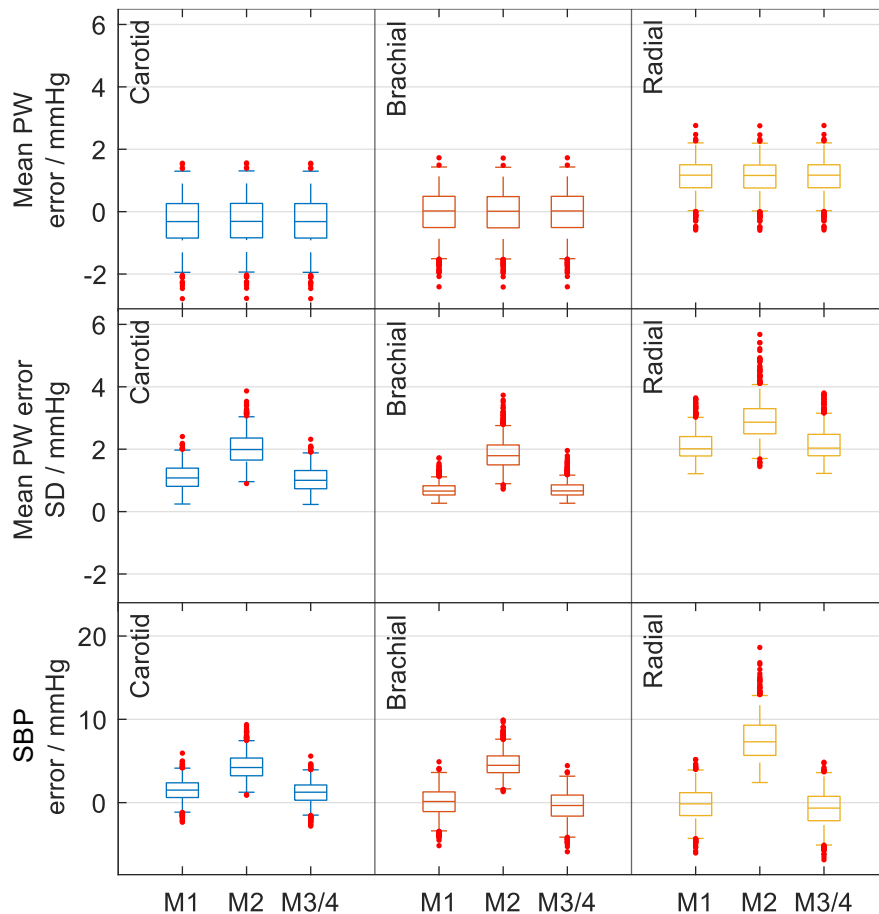
Figure 3.5: Study of the BP models' error. Sample of 25-year-old subjects (n=729) at the carotid, brachial and radial artery for the best models (M1, M2 and M3/M4). The first and second row illustrates the mean pulse wave error and its standard deviation, respectively. SBP error is shown on the third row.

The mean PW error is the same in M1 and M3/4 at all sites (-0.31 mmHg for the carotid artery, 0.023 mmHg in the brachial artery, and 1.170 mmHg for the radial artery). The SD and SBP errors are

higher in M2 than in the other models. In the carotid artery, M3/4 has a smaller SBP error than M1 (SD error difference less than 0.25 mmHg). However, at the brachial and radial artery M1 has a lower SD and SBP error than M3/4. Thus, it is corroborated that in a 729 subject-study, M1 is the most accurate model for the radial artery with a mean PW SD error of 2.013 mmHg and SBP error of –0.151 mmHg. In contrast, for applications that require measurements at the carotid artery, the M3/M4 models should be applied.

3.4 Discussion

Several models have been proposed that relate hemodynamic variables indirectly to BP. In the present work, five models that ultimately take the distending luminal area were studied *in-silico* through an arterial PW simulated database. To the best of my knowledge, this was the first time a comparison study of BP models was done in a large (n=729) and variable database.

All the studied models rely on the physical assumption that the luminal area is circular, neglecting the possibility of an irregular and asymmetric area and, therefore, excluding the cases of highly tortuous arteries. Additionally, the models assume linear elasticity, meaning that pressure and luminal area PWs have the same temporal profile. However, due to the natural viscoelasticity of arteries, this is known not to be true, and it is corroborated in this study with the compliance curves and the early-systolic underestimation between the ground truth pressure and the calculated PW from the different models. The time delay is larger at the radial artery, due to the increase in collagen content and, consequently, viscoelasticity.

Another common limitation between the models is that all non-invasively acquired arterial pressure waveforms require calibration to a known BP, imposing potential sources of measurement errors. It is generally accepted that DBP and MAP do not change considerably through the arterial tree, however, there are small changes, as seen in this study (see Figure 3.4), introducing over- and underestimation in DBP at the carotid and radial artery, respectively, when calibrated to brachial DBP. Furthermore, it is known that every MAP that uses a form factor (FF) to quantify the change in the shape of the blood pressure waveform and relates its mean pressure to SBP and DBP has flaws. As the shape of BP changes along the artery tree due to propagation and reflection phenomena, it is understandable that a common MAP equation is not possible. Whilst a FF of 0.3 might be closest to the invasively measured MAP at the radial artery, the same could not be said about the brachial artery. A study by

Dr Papaioannou (Papaioannou et al., 2016) demonstrated that the estimation of MAP using the FF value of 0.412 provides results that are more accurate to invasive brachial MAP calculation when compared with MAP determined by the traditional formula, which uses FF=0.3. In the current work, FF=0.412 was used to best approximate brachial MAP to its true value.

The M5 pressure profile shown in Figure 3.4 converges to the one displayed by the results presented in the researchers' work (Soleimani et al., 2017), which is characterized by a distinct and separate two-peak waveform. All models except for M5 were able to approximate the shape of their BP waveform to the ground truth. The differences between the shapes can be appointed to M5 taking the flow velocity profile into account, while for the other models the only time-dependent variable is the change in the luminal area and its shape is similar to the pressure waveform. Additionally, it is worth noting that the calibration procedure proposed by the authors, that correlates a subject MAP values from their proposed method and values measured from the radial artery by tonometry over a group of cardiac cycles, could not be applied in the current study, as the database only supplies one cardiac cycle per subject. This underlying impracticability may have resulted in an increased pressure error, as the subject specific calibration was done with the values supplied by the researchers' work (Soleimani et al., 2017).

The simulation study showed a slight difference in the best applicable model (M1) at different measuring sites. While in theory the carotid artery exhibits a more linear compliance behaviour than the radial artery, M3/4 (logarithmic model) proved to have a lower error value than M1 (linear model). The contrary was seen at the radial artery, where although there is higher viscoelasticity and arterial rigidity, M1 turned out to be the model with the lowest error. Nonetheless, the differences in error between M1 and M3/4 are quite small (less than 0.6 mmHg).

The International Organization for Standardization (ISO) recommends a maximum mean difference of ±5 mmHg and a standard deviation of ±8 mmHg between the standard and the novel automated sphygmomanometers measurements (ISO 810-602:2018, 2018). As there are no standardized protocols for device validation regarding BP model use, this ISO was used for comparison and validation of the results. Taking the database's pressure waveform as standard, M1 and M3/4 accomplished this requirement, whilst M2 and M5 did not comply with the recommendations, introducing a higher mean difference and variability of (5.661±2.8379) mmHg for M2 and (3.853±9.030) mmHg for M5, when applied at the radial artery. As the exponential relationship is the most used model for extracting pressure

waveform from ultrasound measurements of arterial wall distensibility in known literature review (Gavish & Izzo, 2016; Meinders & Hoeks, 2004; Wang et al., 2018), it was expected that M2 would reveal a better accuracy than M1 (linear model), but that was not the case. Whereas the linear model (M1) follows the ISO recommendations and has the best results in the brachial and radial artery, the exponential model (M2) metrics are above the recommended values and is the second worst performing model in the present study.

3.5 Key findings and working principle

The first research question (RQ1), "How to indirectly measure BP through US at the wrist?", can be answered. As referred previously, the hemodynamic properties of a vessel can be correlated to pressure by mathematical transformations. What remained to be studied was which state-of-the-art BP model (introduced in Section 2.2) was the most accurate for measurements at the wrist, through recordings of hemodynamic properties at the radial artery. This *in-silico* study revealed that the linear model is the most accurate for measurements at the radial artery, which simply takes the luminal distension of the artery and linearly correlates it to a BP waveform through a DBP and MAP calibration. Therefore, BP measurement through US at the wrist can be accomplished by recording the distending diameter waveform and applying a mathematical model which transforms the waveform into a pressure reading.

The pulse-echo principle and diameter assessment through US has been introduced in Section 2.3.2 and Section 2.3.2, respectively. To summarize and clarify, Figure 3.6 represents the working principle of one diameter reading, after one electrical pulse has been introduced at the US transducer. Through the piezoelectric effect, the electrical signal is converted to a US wave. At each acoustic interface, the US is partially reflected to the transducer creating echoes along the wave propagation path. The reflected US waves are then converted back to an electrical signal by the piezoelectrical effect at the transducer. To each pulse introduced at the PUT, a corresponding frame of echoes are acquired. By determining the TOF of the maximum voltage of the echoes corresponding to the inner anterior and posterior of the vessel, the inner diameter of the artery can be determined. At this point, the corresponding BP is calculated by applying the most accurate model at the radial artery, the linear model.
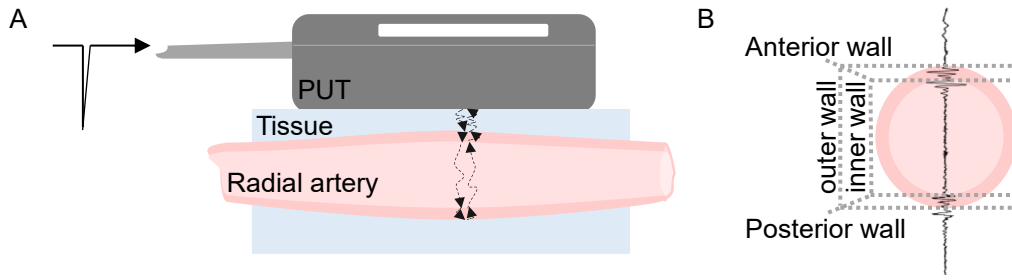
Figure 3.6: Working principle of a diameter reading. (A) An electrical pulse is introduced at the PUT and converted into a US wave. At each acoustic interface, an echo is created and reflected to the PUT. (B) Characteristic schematic of a raw electrical signal originated from the US echoes produced from one electrical pulse.

4 PIEZOELECTRIC ULTRASOUND TRANSDUCER

A custom-made PUT composed of three rectangular piezoelectric elements in an isosceles trapezium arrangement (aperture angle of 24.5°) was used as the US transducer. Each piezoelectric element is made of Lead Zirconate Titanate (PZT) with a dimension of 10×5 mm². The backing material, to which the ceramic materials are glued, is made of Obomodulan 500, which has a very low acoustic impedance, allowing for backward wave damping and broader piezo bandwidth. Furthermore, a layer of polyurethane is included for acoustic impedance matching on top of the piezoelectric elements. A printed board circuit (PCB) is inserted on the bottom of the backing material for signal routing, to which an RJ45 cable is connected. The three PZTs are enclosed in a 3D-printed housing. A schematic of the transducer, with the PUT's interior structure, is depicted in Figure 4.1A. A photograph of two similar packaged ultrasound sensors is shown in Figure 4.1B.
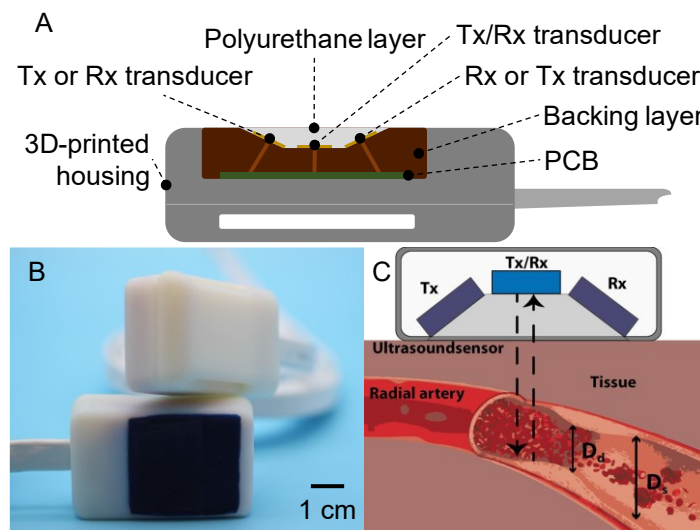
Figure 4.1: Piezoelectric ultrasound transducer. (A) Schematic of the interior structure, (B) package of two sensors, and (C) application of the Tx/Rx transducer. Figures (B) and (C) are adapted from (Amado-Rey et al., 2021).

As represented in Figure 4.1C, the middle transducer functions both as sender and receiver (Tx/Rx) of the acoustic signal, granting a perpendicular reading of the vessel wall echoes. This piezoelectric element serves as the measuring tool for the distending arterial diameter through the TOF between the anterior and posterior wall echoes.

The lateral transducers act independently as transmitter (Tx) and receiver (Rx) sensors, and although the function (Tx or Rx) can be interchangeable between them, one sensor is always the transmitter and the

other the receiver. The two lateral transducers are meant to be used for flow velocity measurement through the Doppler Effect. However, this functionality was not studied in the scope of this project, and only the middle transducer was used.

For later integration with the acquisition system, it is important to perform acoustic and electrical characterization of the PUT. Acoustic measurements of the sensor were supplied by the manufacturers and electrical characterization was performed in this work.

4.1 Acoustic characterization

The xz (lateral distance-focal depth) and yz (elevation distance-focal depth) acoustic pressure field of the piezo element, shown in Figure 4.2, were measured with a Hydrophone RP 50s (RP Acoustics, Leutenbach, Germany) by Fraunhofer IBMT (Saarland, Germany). The focus distance of 21.1 mm has been determined by the Near Field Length equation that depends on the geometry and frequency of a single-element transducer. The pressure field manifests a broad bandwidth of -4 dB in the xyz-plane for a focal depth deeper than 30 mm, encompassing the calculated focus distance (21.1 mm).
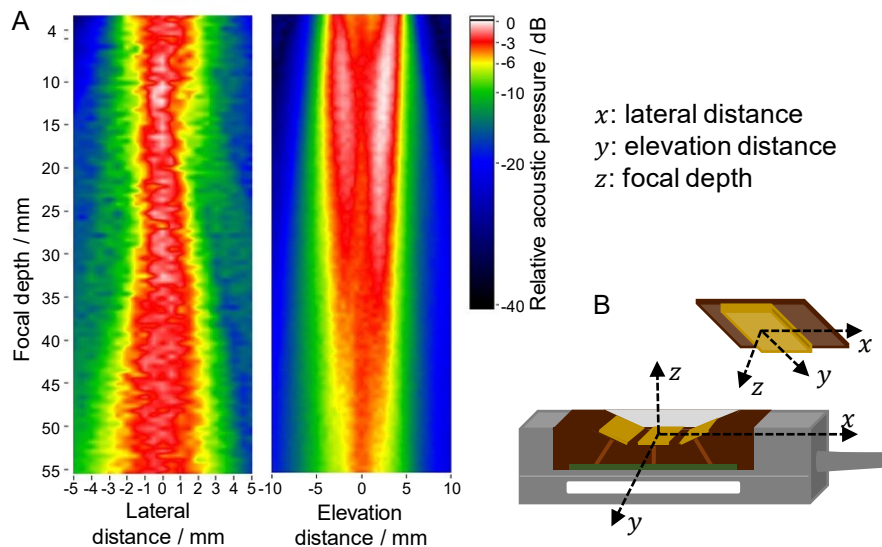
Figure 4.2: Acoustic characterization of the Tx/Rx transducer. (A) Representation of the acoustic field in the xz-plane (lateral distance-focal depth) and the yz-plane (elevation distance-focal depth) adapted from (Amado-Rey et al., 2021) with (B) clarification of the planes in the transducer schematic.

4.2 Electrical characterization

Electrical characterization was made through reflection, impedance, and phase measurements in a broad frequency range (100 kHz – 20 MHz) with a VNA. The device used was the Bode100 (OMICRON

electronics GmbH, Klaus, Austria), depicted in Figure 4.3A. Before performing any measurement with the VNA, an open, short and load (OSL) calibration process was completed in the frequency measurement range. The calibration procedure is of high importance and has the purpose of removing the effect of the BNC cable used in the measurement (OMICRON electronics, 2017; Tofighi et al., 2017). With the cable connected to the output of the VNA, open calibration is performed by leaving the distal end of the BNC cable unconnected, followed by connecting it to BNC short circuit (Figure 4.3B) and BNC 50 Ω load (Figure 4.3C) for short and load calibration, respectively. The electrical characterization measurements were performed by connecting the output of the VNA to the PUT with the calibrated BNC cable, using an RJ45-BNC adapter enclosed in a custom-made faraday cage. The reflection coefficients (S_{11}-parameter) file was saved in one-port touchstone format (*.s1p) for network matching design.
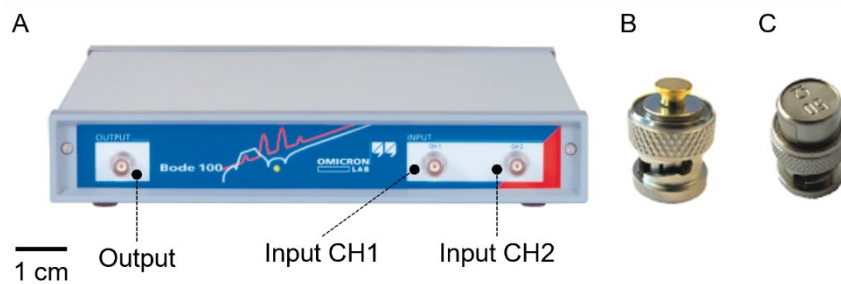
Figure 4.3: VNA device used for electrical characterization. (A) Bode100 with frontal connecting ports identified, (B) BNC short circuit connector and (C) BNC 50 Ω load connector for BNC cable calibration. Adapted from (OMICRON electronics, 2017).

Impedance and phase measurements of the Tx/Rx piezoceramic are illustrated in Figure 4.4. The first resonance frequency (f_r) was measured at 4.121 MHz (14.175 Ω, -22.544°) and anti-resonance frequency (f_a) at 5.443 MHz (52.627 Ω, -8.185°), both identified in the graph. The frequency at which the phase of the impedance is cancelled out ($Z_{null-phase}$=51.496 Ω) is at 5.336 MHz. At 5 MHz the system is characterized by an impedance of (36.916 Ω,19.834°).
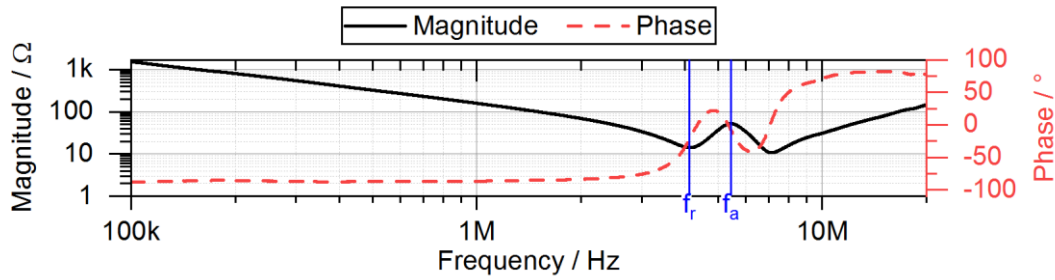
Figure 4.4: Electrical characterization of the Tx/Rx transducer. Impedance and phase characterization in a broadband range (1 kHz - 20 MHz). The first resonance frequency (f_r=4.121 MHz) and anti-resonance frequency (f_a=5.443 MHz) are indicated.

4.3 Electrical impedance matching network

For the application under study, matching the PUT to a chosen frequency and towards the usual circuitry impedance of 50 Ω is desirable. PUT adaptation to this impedance allows for a versatile transducer-EIMN assembly matched to 50 Ω applications, instead of focusing on a specific electronic device impedance.

4.3.1 Circuit design

QucsStudio (Michael Margraf, 2021) simulator was used for the EIMN design. A simple circuit was created with a 50 Ω impedance source, representing the acquisition device, and a 1-port S-parameter file, which simulates the load. The 1-port block takes as input the Tx/Rx transducer's S_{11}-parameter file (reflection coefficients acquired during electric characterization of the Tx/Rx transducer, see Section 4.2) in touchstone format (.s1p). After running the S-parameter simulation, the reflection coefficients were plotted in the Smith Chart diagram and electric impedance matching was done to the chosen frequency. As the maximum power transfer frequency was desired to be at 5 MHz, the EIMN was designed by selecting 5 MHz in the S_{11}-parameter curve on the Smith Chart diagram. The simulation resulted in a EIMN in L-configuration with a capacitor (0.948 nF) in series and an inductor (2.717 µH) in parallel, as seen in Figure 4.5.

For EIMN validation, the matching network circuit was introduced between the 50 Ω impedance source and the 1-port S-parameter file device (similarly to the circuit in Figure 4.5) and a new S-parameter simulation was made.

The EIMN circuit was adapted to commercially available values (inductor dimension set to 2.7 µH and capacitor dimension set to 1 nF), and its behaviour was simulated in QucsStudio.
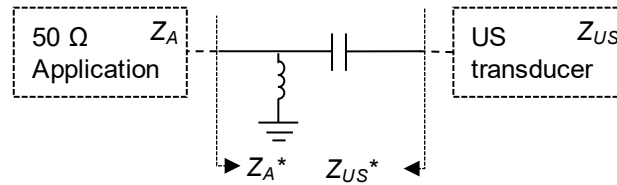
Figure 4.5: Schematic of the simulated EIMN design. The electrical impedance matching is accomplished by an EIMN in L-configuration between the US transducer and a 50 Ω application.

After circuit validation, an L-configuration PCB was designed with the tuned components. Two SMA connectors are introduced at the input and output of the board for simple connection to the acquisition device and US transducer. The EAGLE software (Autodesk Inc, 2020) was used for schematic and board design. Figure 4.6 shows the final probe's matching network, with the PCB total area of 25×20 mm^2.
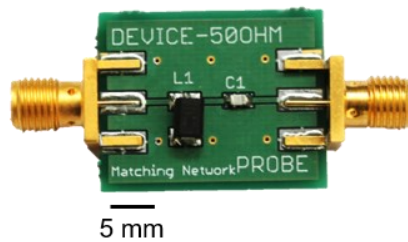
Figure 4.6: Photograph of the probe's matching network board.

4.3.2 Circuit characterization

For the validation of the introduced matching network, the 50 Ω impedance matched transducer, composed of the US-probe followed by the EIMN, was electrically characterized. An impedance measurement was performed in a broad frequency range (100 kHz - 20 MHz) with the Bode100, following the process described in Section 4.2.

The normalized impedance (normalization to 50 Ω) of the piezoelectric transducer before and after the matching networks is represented in a Smith Chart in Figure 4.7. Symbols are used on each normalized impedance curve to indicate the point in which 5 MHz is represented. The optimal impedance at 5 MHz (at the simulated optimal EIMN) was purely resistive 50 Ω (see the star symbol in the centre of the graph). The simulated impedance of the probe with the implemented EIMN board at 5 MHz was (48 Ω, 1.57°). A small decrease in impedance to (46.6 Ω, 3.52°) was measured when using the probe with the EIMN

PCB and comparing it to the simulated value, but a much better matching to 50 Ω was provided than when using the probe without the matching network (36.916 Ω, 19.834°).
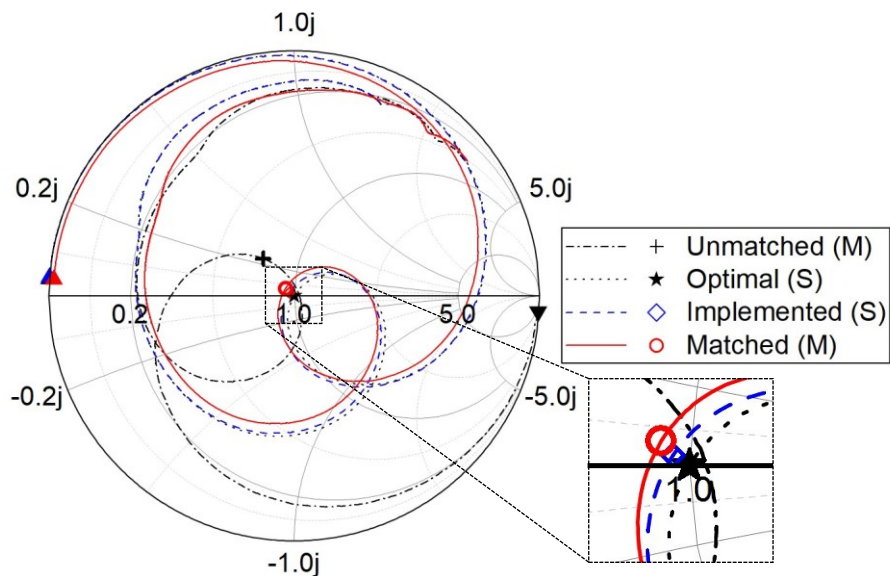
Figure 4.7: Influence of the EIMN in the PUT's impedance. The probe's impedance is represented by the unmatched curve (dashed-dotted line). The simulation of the probe's impedance with the optimal and implemented matching network is represented by the dotted and dashed line, respectively. The measurement of the probe's impedance with the matching network is represented by the straight line. The impedance at 5 MHz is identified by each curve's symbol. (S) stands for the simulation and (M) for the measurement of the normalized impedances. Smith chart normalized to 50 Ω. Impedance curves plotted from 100 kHz to 20 MHz with a triangle at 100 kHz indicating the direction of the sweep (increase in frequency).

4.4 Discussion

The PUT is characterized by an impedance of (36.916 Ω,19.834°) at 5 MHz. The maximum response of the piezoelectric element depends not only on its characteristics but also on those to which the transducer is connected, e.g., the source or acquisition device. For a maximum power transfer, the transducer's impedance at the desired working frequency should be the complex conjugate of the source's/acquisition device's impedance. To establish a better impedance matching between the transducer and connected devices, an EIMN was designed and developed at 5 MHz for 50 Ω applications.

It is easily understood that after implementing an optimal EIMN to 50 Ω at 5 MHz, the normalized impedance at 5 MHz of the unmatched probe (identified with a cross symbol in the graph in Figure 4.7) is converted to the origin of the smith chart (identified with a star symbol), where the phase is null and the normalized impedance is 1. The dimensions of the components of the developed EIMN board were tuned to commercially available values (instead of the simulated values), and therefore the simulated implemented impedance curve was slightly different than the optimal. The small difference

(-1.4 Ω, 1.95°) between the simulated and measured impedance of the implemented matching network with the probe can be dismissed. The introduction of the matching network between the probe and a device changes the probe's impedance from (36.916 Ω, 19.834°) to (46.6 Ω, 3.52°) at 5 MHz. The EIMN introduction between the probe and a 50 Ω application device would improve the power transfer and decrease by 23 % the reflection coefficient (calculations with Equation 2.28).

Unfortunately, due to experimental scheduling, the development of said EIMN was only accomplished after the experimental tests for the extraction of diameter and consequent pressure derivation. Further studies should be implemented in which the EIMN is used during the experimental tests.

5 ECHO RECEIVER CIRCUIT DEVELOPMENT

During this work, diameter assessment was employed by determining the point of time when the highest peak occurs at each reflection window, followed by the calculation of TOF. RQ2 enquiries the necessary characteristics of an electronic system in order to achieve the working principle of the proposed device. To address this question, the signal derived from the reflections of the vessel's walls was assessed.

The reflected signal is expected to have a small amplitude (in the order of 30 mV), due to attenuation of the ultrasounds whilst travelling through the tissue. Hence, an amplification of 20 dB is suitable. Furthermore, as the reflected signal is characterized by a 5 MHz gaussian curve, bandpass filtering at this frequency is needed. Due to the high working frequency of the US probe (5 MHz), the circuit must have a high-speed response (slew-rate) to alternating signals. A high-speed peak detector circuit was developed to amplify, filter, and simplify the post-processing of the receiving reflections of the artery's walls.

5.1 Circuit design

The echo receiver circuit consists of four stages, as seen in Figure 5.1. At the input, the received echo signal is amplified by a non-inerting amplifier. Next, the signal passes through a buffer needed for impedance matching to the next stage of the circuit: a bandpass filter. After filtering, the signal reaches the core of the echo receiver circuit, an amplitude-modulated peak detector, where the maximum of the signal is extracted through a half-wave rectifier.

The operational amplifier (OpAmp) used in the first three stages of the circuit was the LM7171 (Texas Instruments, 2014), chosen due to its high-speed response to alternating signals. The integrated circuit is characterized by a very high slew rate of 950 V/μs and a wide unit-gain bandwidth of 125 MHz (at the bias-supply voltage of ±5 V).

A common power supply of ±5 V was applied to the three OpAmps. Power supply bypass was necessary to guarantee low DC-impedance and high-impedance response for the AC working frequency (Texas Instruments, 2014). Two AC-blocking capacitors were introduced at both the negative and positive power supply pins, a 0.01 μF ceramic capacitor connected directly to the power supply pins and a 2.2 μF tantalum capacitor close to the power supply pins. For simplicity reasons, the bypassing capacitors are not shown in the schematic (Figure 5.1).
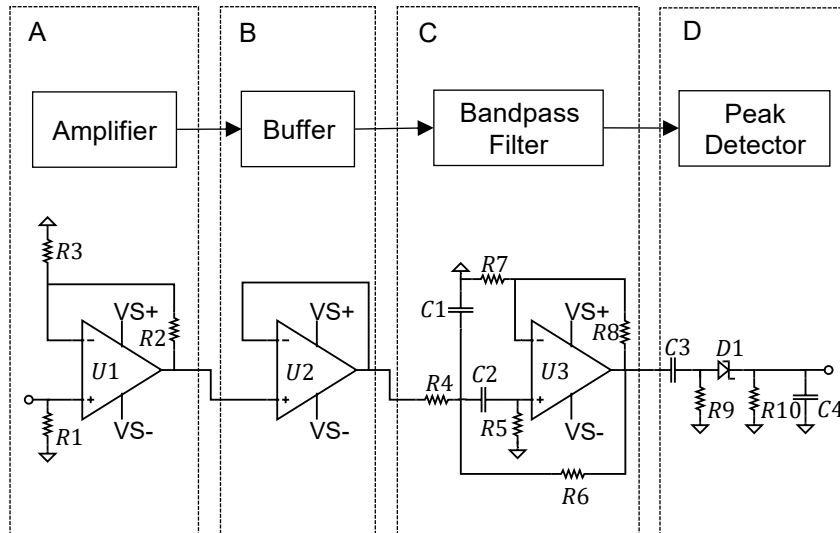
Figure 5.1: Schematic of the echo receiver circuit. The circuit is composed of four stages: (A) amplifier, (B) buffer, (C) bandpass filter, and (D) peak detector.

Table 5.1 lists the bill of materials (BoM) of the developed echo receiver circuit, only including the components represented in Figure 5.1. For the complete list of materials of the developed board see Appendix A4.

Table 5.1: BoM of the developed echo receiver circuit. Bypassing capacitors not listed.

Resistors		Resistors		Capacitors		Others	
Part	Value (Ω)	Part	Value (Ω)	Part	Value (F)	Part	Component
$R1$	180	$R6$	820	$C1$	4.8 p	$U1$	LM7171
$R2$	470	$R7$	16.2 k	$C2$	10 p	$U2$	LM7171
$R3$	47	$R8$	2.49 k	$C3$	1 μ	$U3$	LM7171
$R4$	10 k	$R9$	150	$C4$	2 n	$D1$	ZHCS1000
$R5$	30 k	$R10$	150				

Non-inverting amplifier

The first stage of the echo receiver is composed of a non-inverting power amplifier (Figure 5.1A), with $R2$=470 Ω and $R3$=47 Ω. As the gain of a non-inverting amplifier is given by Equation A.1 (in Appendix A3.1) it would be expected a gain at this stage of 20.83 dB.

Buffer

A buffer (Figure 5.1B) was introduced between the non-inverting amplifier and the bandpass filter for impedance matching between the two stages.

Bandpass filter

The third stage of the echo receiver circuit is a second-order bandpass filter, shown in Figure 5.1C, with a Sallen-Key topology (Ron Mancini, 2002; Texas Instruments, 2002). The configuration of the filter was optimized until a mid-frequency of 5 MHz was achieved. The filter was dimensioned as indicated in Table 5.1. The mid-frequency gain, defined by Equation A.4 (see Appendix A3.2), is expected to be -4.01 dB.

Modified peak detector

The fourth and last stage of the echo receiver circuit is shown in Figure 5.1D. The high-frequency peak detector consists of a decoupling capacitor $C3$=1 µF, followed by a DC return path, $R9$=150 Ω. Afterwards, a half wave rectifier, composed of a ZHCS1000 Schottky diode (Diodes Incorporated, 2015), and a capacitor and resistor were placed in parallel, which were dimensioned to remove the high-frequency elements of the signal. The RC network was designed to accomplish Equation 5.1, where w_c is the angular frequency of the signal. As the signal of interest has a frequency of 5 MHz, the RC-filter network was dimensioned with $C4$=2 nF and $R10$=150 Ω.

$$RC \gg \frac{1}{w_c} \tag{5.1}$$

Echo receiver PCB design

The PCB of the echo receiver circuit was designed with the EAGLE software and externally processed and fabricated. The board is composed of two 35 µm-thick copper (Cu) layers (top and bottom) separated by a 1.55 mm-thick FR4 (fibreglass-reinforced epoxy-laminated) substrate. Both Cu-layers follow a coplanar waveguide configuration (the conductor strip is printed onto a dielectric material together with a pair of ground planes, one on each side of the conducting track, separated by a small constant gap along the line) and the total PCB area is 61×50.5 mm². The reflow soldering process was used to solder the components with the reflow oven ProtoFlow S (LPKF Laser & Electronics, Garbsen, Germany). Figure 5.2 shows the final product. The PCB schematic and the complete BoM can be found in Appendix A4.
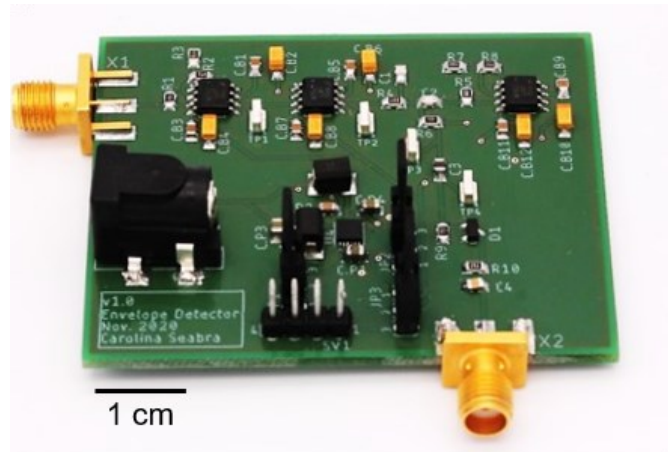
Figure 5.2: Photograph of the developed echo receiver board.

5.2 Circuit characterization

Before experimental testing, time domain and frequency domain simulations were performed in LTSpice XVII (Analog Devices Inc, 2021) to analyse the circuit behaviour. First, gain measurements (frequency range from 100 kHz to 25 MHz), were done over the first and third stages of the circuit. Additionally, a complete 2-port S-parameters simulation (S_{11}, S_{12}, S_{22}, S_{21}) was carried out in the frequency range 100 kHz – 20 MHz for the bandpass filter. For analysis of the system behaviour in the time domain to an ultrasound-like reflection signal, a burst sinusoidal signal (amplitude of 30 mV, frequency of 5 MHz, and 5 cycles) was introduced as input in the complete circuit. The output was studied at each stage through a transient simulation.

For simulation and experimental testing comparison, the same tests were performed on the manufactured board. The VNA Bode100 was used for gain measurement, as well as for S-parameters testing. For the time-domain signal test, a signal generator (Keysight 33500Bseries, Keysight Technologies Inc, California, United States) was used for introducing the burst signal and a PC-oscilloscope (PicoScope 5243D, Pico Technology Ltd, St Neots, United Kingdom), which will be described in more detail in Section 0, was used for acquiring the signals.

The total DC-power consumption of the circuit was 260 mW.

5.2.1 Non-inverting amplifier characterization

The gain spectrum of the non-inverting amplifier, containing the experimental and simulated curves, is shown in Figure 5.3. The simulated and experimental gain at low frequencies are both 20.8 dB without

any dephase between the input and output signals. At 5 MHz, the simulated and experimental curves indicate a gain of (20.6 dB, -12.5°) and (19.9 dB, -30.3°), respectively. The developed amplifier is characterized with a 3 dB bandwidth of 10.6 MHz, with a bandwidth decrement that exceeds 10 MHz when compared with the simulated value of 24.7 MHz.

Figure 5.3: Gain measurement of the non-inverting amplifier. The simulated curves (thick lines) were performed in LTSpice. The measured curves (thin lines) were measured with the Bode100. Amplifier characterized by a maximum gain of 20.8 dB.

5.2.2 Bandpass filter characterization

The bandpass filter characteristic gain spectrum is shown in Figure 5.4 and important values are included in

Table 5.2 (with the simulated and experimental results). A decrease in mid-frequency gain (8.72 dB difference) is seen between the experimental and simulated circuit, accompanied by an increase in bandwidth (filter's measured bandwidth: (2.672 to 12.196) MHz) and mid-frequency values. At frequencies outside the filters bandpass, a good agreement between the two curves is appreciated. At 5 MHz the experimental circuit is characterized with a gain of (-5.79 dB, 1.65°), as compared to the simulated gain of (2.96 dB, 10.44°).
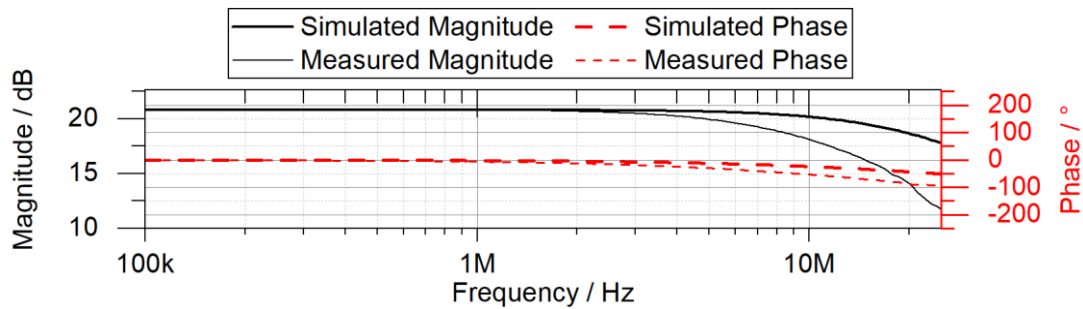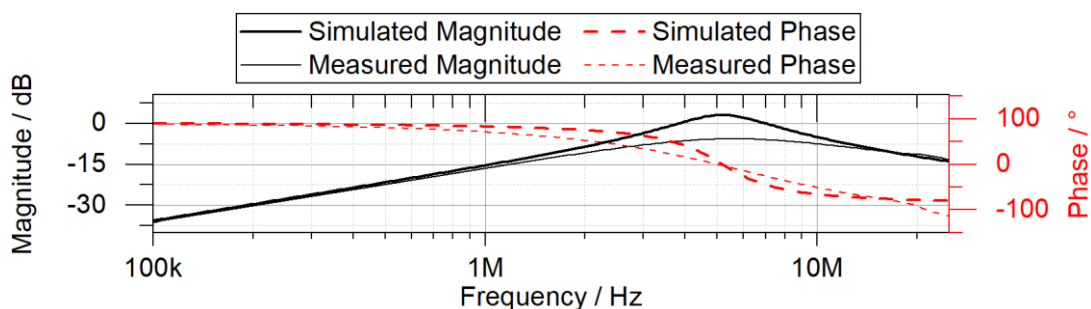

Figure 5.4: Gain measurement of the bandpass filter. The simulated curves (thick lines) were performed in LTSpice. The measured curves (thin lines) were measured with the Bode100. Bandpass filter characterized by a simulated mid-frequency gain of 3.05 dB and a measured mid-frequency gain of -5.67 dB.

Table 5.2: Characteristics of the bandpass filter.

	Mid-frequency (MHz)	Maximum gain (dB)	3 dB Bandwidth (MHz)
Simulated	4.87	3.05	3.20
Experimental	5.63	-5.67	9.52

The scattering parameters associated with the bandpass filter are shown in Figure 5.5. Overall, the simulated and measured curves have high similarities. However, it should be noted that the measured S_{12}-parameter exhibited instability at low frequencies, producing the variable signal in Figure 5.5B. The reflection coefficients (S_{11}- and S_{22}-parameter) are characterized with a magnitude close to zero, with S_{22} decaying at higher frequencies and a phase inversion in the proximity of 1 MHz. The reverse transmission coefficient (S_{12}-parameter) has a magnitude below -50 dB and the forward transmission (S_{21}-parameter) presents the same bandwidth as the gain shown in Figure 5.4 with an increase in the magnitude of approximately 6 dB.
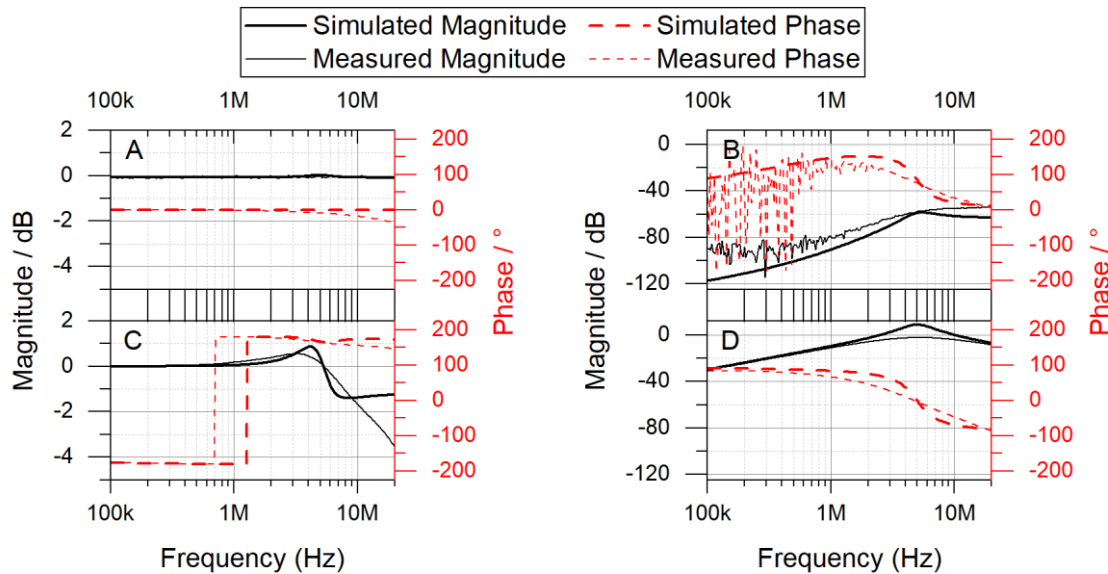
Figure 5.5: S-parameters measurements of the bandpass filter. (A) S_{11}-parameter, (B) S_{12}-parameter, (C) S_{22}-parameter and (D) S_{21}-parameter. The simulated curves (thick lines) were performed in LTSpice. The measured curves (thin lines) were measured with the Bode100.

5.2.3 Amplifier and bandpass filter block

The gain spectrum of the combined amplification and filtering stages is shown in Figure 5.6. The same relation between the simulated and measured gain is observed. The curves have a similar characteristic,

except for the gain of the bandpass filter, with an approximate increase of 20 dB and a smaller 3 dB bandwidth in the simulated results. The maximum gain and corresponding frequency, as well as the 3 dB bandwidth, are summarized in Table 5.3. At 5 MHz the measured gain was of (14.243 dB, -30.262°), a decrease in the gain of (9.753 dB, -23.237°) when compared to the simulated values.
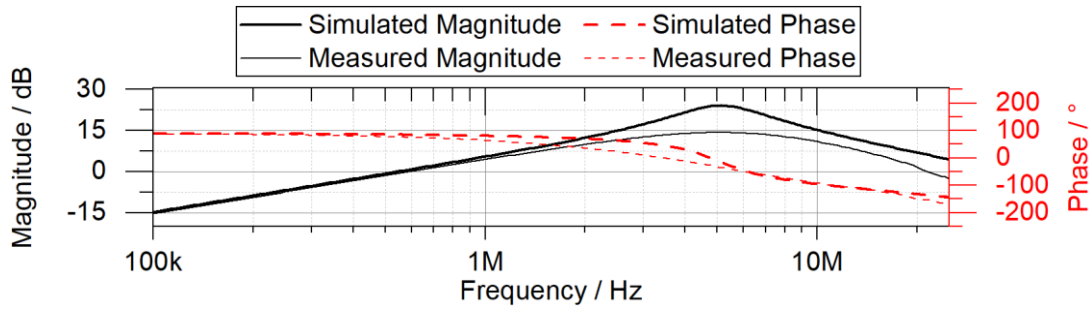
Figure 5.6: Gain measurement of the amplification and filtering stages. The simulated curves (thick lines) were performed in LTSpice. The measured curves (Exp., thin lines) were measured with the Bode100.

Table 5.3: Characteristics of the combined amplification and filtering stages.

	Mid-frequency (MHz)	Maximum gain (dB)	3 dB Bandwidth (MHz)
Simulated	5.127	24.062	2.871
Experimental	5.041	14.247	7.254

5.2.4 Transient circuit behaviour

The response to a burst signal was measured at each stage of the echo receiver circuit. Figure 5.7 shows the input signal and the simulated and experimentally measured output at the amplification and filtering stages, after the DC return path and at the output of the board. The proximity between the measured and simulated signal is observed at the output of the amplification stage, with a gain of approximately 20.6 dB and a negative phase shift of 18.36° and 25.2° in the simulated and experimental signals (respectively) to the input signal. At the output of the bandpass filter, a characteristic gain of (23.94 dB, -22.84°) in the simulated signal and (15.05 dB, -43.2°) in the experimental signal was measured, with a symmetrical offset of 100 mV in both signals. After the DC return path, the offset was removed, and the gain characteristics remained the same. In the output of the echo receiver, demonstrated in Figure 5.7D, the amplified envelope of the input signal is seen. The gain decreased to (19.52 dB, -24.61°) in the simulated signal and to (1.068 dB,- 21.6°) in the experimental signal.
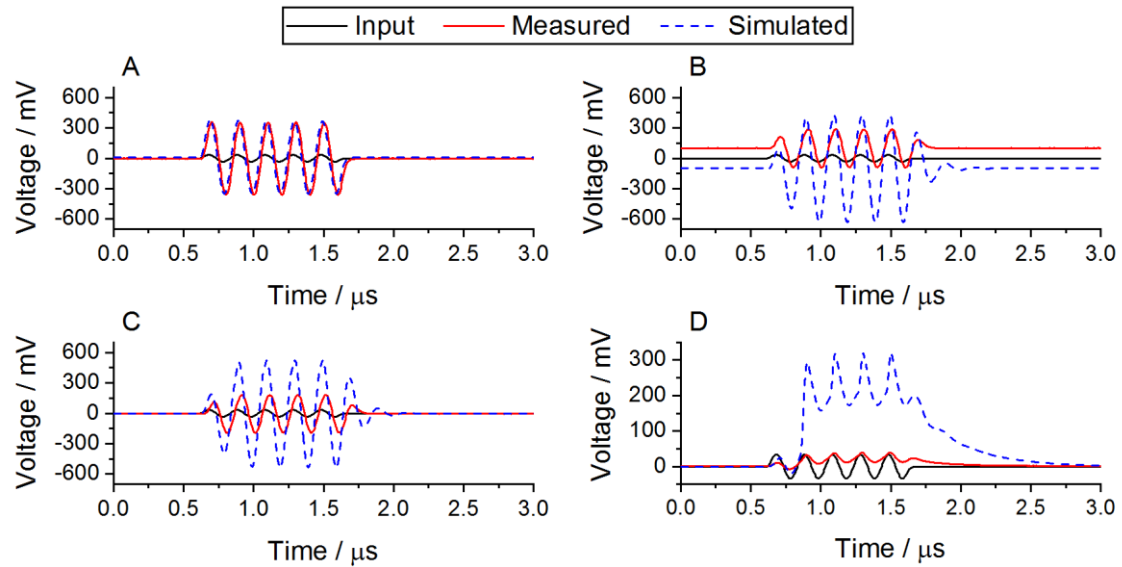
Figure 5.7: Response of the echo receiver to a burst signal. A sinusoidal burst signal (30 mV of amplitude at 5 MHz, with 5 cycles) was introduced at the input of the board. The conditioned signal is shown at the (A) output of the amplification stage, (B) output of the filtering stage, (C) output of the DC return path and (D) output of the echo receiver board.

5.3 Discussion

In the non-inverting amplifier, the decrease in gain compared to the simulated value is inferior to (1 dB, 20°) at 5 MHz, but in the bandpass filter, there is a much bigger difference between the simulated and experimental gain. Furthermore, it is noted that the experimentally measured maximum gain in the bandpass filter (-5.67 dB) has a smaller error compared to the calculated and predicted gain (-4.01 dB, see Section 5.1), than that of the simulated value (5.63 dB).

To assess why there is such a difference in the filter's gain, the bandpass filter S-parameters were measured. The reverse transmission coefficient, also known as S_{12}-parameter, is below -50 dB, meaning that there is a very small wave transmission from the output to the input, which is desired. The transmission from input to output is as expected, with a 6 dB increase in the magnitude when compared to the bandpass filter gain measurement, respecting the transmission coefficient formula $|Gain| + 20 \cdot log(2)$ (OMICRON electronics, 2017). The reflection parameters (S_{11}- and S_{22}-parameters) revealed to be approximately 0 dB, indicating that the input and output impedance is highly mismatched with the source impedance (50 Ω set by the VNA measuring device). At a first glance, it would be assumed that this is the reason for the difference between the simulated and experimental values, but the S-parameters simulation also has its values close to 0 dB, possibly meaning that the simulation models do consider the impedance mismatch between the source and the circuit in all

simulations. That being said and pointing out once more that the measured experimental gain is closer to the predicted calculated value at mid-frequency, the differences in the gain spectrum in the bandpass filter are attributed to possible errors in the simulation model (for disclosure, the amplifier model used in the simulation was extracted from the manufacturer's website) and should be closer to the experimental values. The differences between the simulated and measured behaviour might be due to inaccuracies of the LTspice models at higher frequencies, or due to the ideality of the simulations of LTspice, in which the capacitive coupling effects might not be considered.

When evaluating both stages together, the decrease in 3 dB bandwidth and mid-frequency shift is attributed to the sum of the gain spectrum of each stage, resulting in an expected characteristic gain. The differences between the experimental and simulated results are attributed to what was discussed in the previous paragraph.

Up to the filtering stage, the behaviour of the circuit in the time domain agrees with the study's prediction in the frequency domain. The small differences between the gain measured at each stage in the frequency and time domain might be due to calculation errors. The introduced offset by the bandpass filter is removed after the DC return path without dampening the signal. An acute decrease in gain was measured between the modified envelope detector stage, after the DC return path and the output of the board. The decrease was tremendously more noticeable in the measured signal, where the difference was approximately 14 dB than in the simulated curve (gain decrease of approximately 4.5 dB). The differences are due to the response of the envelope detector to different gains between the simulated and measured signal in the previous stage. Nonetheless, the envelope of the input signal for the detection of the echo-signals with high accuracy was accomplished.

A second version of the echo receiver circuit was designed and fabricated, featuring a voltage gain amplifier, which would allow adapting the gain of the system to each user's dampening tissue response. Due to time constraints, the board was not characterized and validated. Refer to Appendix A5 for the design of the circuit and PCB fabrication.

6 SYSTEM VALIDATION

In this chapter, a preliminary validation procedure of the designed system was developed, answering RQ3. The system prototype, made up of a US sensor complex, a signal acquisition block, and the offline post-processing, was tested on three different mimicking arm setups. A commercial piezoresistive pressure sensor was introduced to validate and calibrate the developed device.

First, the pressure acquisition setups and protocols implemented for the diameter-based pressure measurements are delineated. Then, the results of a silicone tube and porcine artery distension in different experimental setups with signal conditioning provided by the echo receiver are presented, followed by the derived pressure waveform. Finally, the diameter extraction algorithm is reviewed.

6.1 Pressure acquisition setup

To determine the validity of the study, measurements with the most accurate pressure model (selected methodologically through the process described in Section 3.2.3), were performed in various experimental setups. The mechanism for pressure control, type of vessel and blood-mimicking fluid used changes between setups. A brief description of the setups' development follows.

Initially, the pressure was manually controlled through a syringe and the distending diameter of a silicone tube was determined with the PUT and specific algorithm (see Section 6.1.4). Next, the setup was altered by switching the syringe to a centrifugal heart-like pump (see Section 6.1.5). In a final test, the silicone tube was substituted by a porcine artery and the fluid used was changed to a saline solution (see Section 6.1.6). Pressure values acquired by the ultrasound sensor were validated through a commercially available piezoresistive silicon pressure sensor.

Overall, the experimental setups consisted of three parts: a mimicking arm, the ultrasound sensor complex and the acquisition block. Only the mimicking arm setup changed between tests and the evaluation of each specific mimicking arm will be further described in Sections 6.1.4-6.1.6. Section 6.1.1 approaches the ultrasound sensor complex, while Section 6.1.2 introduces the acquisition block. The post-processing algorithm is described in Section 6.1.3. The diagram block shown in Figure 6.1 represents a generic experimental setup with offline post-processing. The experimental methodology is the same for each test and is as follow:

1. The pulser sends a bipolar pulse to the transducer with a certain pulse repetition frequency (PRF).

2.	An ultrasound wave is produced by the piezoelectric material and sent perpendicularly to the vessel.

3.	The reflections produced by the vessel's walls are received by the transducer and converted into a gaussian electric signal.

4.	The signal is transmitted to the pulser/receiver, where it is subjected to internal amplification and filtering.

5.	The modified signal is transmitted to the echo receiver circuit. After further signal conditioning, a modified envelope of the signal is extracted.

6.	Digital signal acquisition is performed by connecting the output of the circuit board to the PC-oscilloscope (channel 1). In parallel, the output of the commercial pressure sensor is also connected to the scope (channel 2).
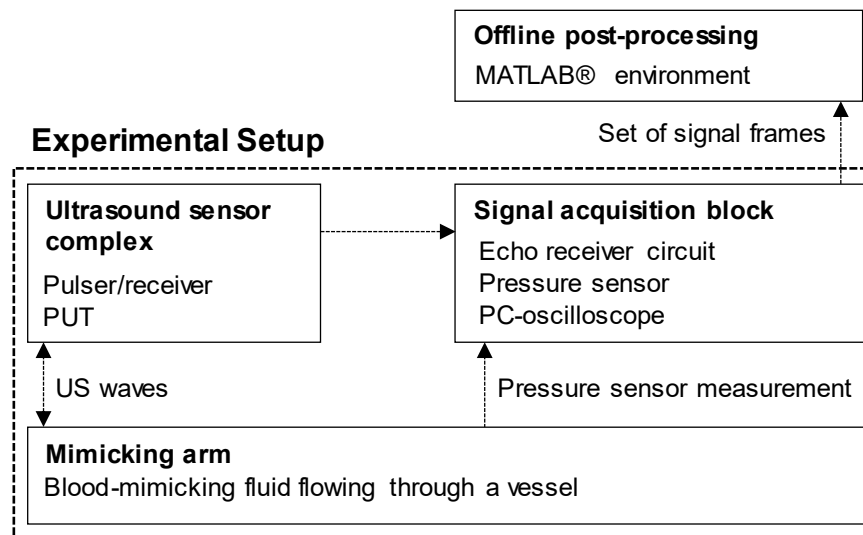
Figure 6.1: Block diagram of the generic experimental setup. The ultrasound sensor complex emits US waves to the mimicking arm, which are reflected to the complex. The US echoes, along with the pressure measurement of the mimicking arm, are acquired by the acquisition block in a set of frames and saved for offline post-processing.

The PC-oscilloscope captures various frames until its memory is full, calling it a test set. Afterwards, post-processing is applied individually to each channel. In channel 1, the diameter of the vessel is extracted from each frame by the TOF between the anterior and posterior walls and the selected pressure model is applied to the diameter waveform. Finally, the diameter-derived pressure waveform is compared to the pressure waveform extracted in channel 2 from the commercially available pressure sensor.

6.1.1 Ultrasound sensor complex

The ultrasound sensor complex is responsible for emitting the ultrasound pulses and receiving the echoes from the vessel's walls. The custom-made US-probe, described and characterized in Chapter 4, was used together with a general-purpose ultrasonic pulser/receiver (DPR300 Pulser/Receiver, Imaginant Inc, Pittsford, United States). The device, with a description of the front panel and a schematic of the rear panel, is seen in Figure 6.2. The pulses sent by the DPR300 are configured in the bottom row of the front panel and the receiving module of the DPR300 is configured by the first row. A summary of the applied controls is shown in Table 6.1.
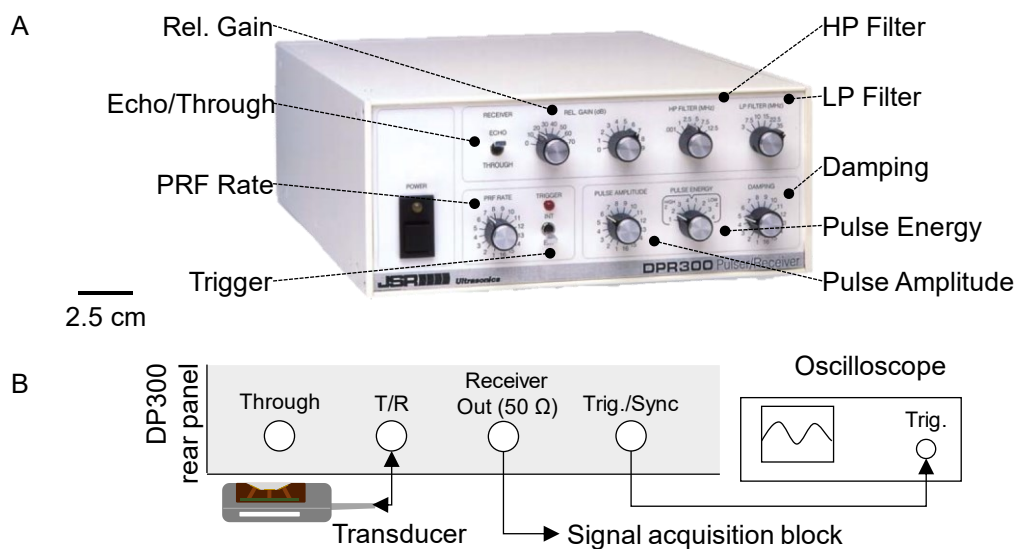
Figure 6.2: Pulser/Receiver panels. (A) DPR300 front panel (adapted from (Imaginant Inc, 2011)) and (B) rear panel in echo-mode operation configuration.

Table 6.1: DPR300 manual controls configuration.

Echo/Through	Rel. Gain	HP Filter	LP Filter	PRF Rate
Echo	36 dB	2.5 MHz	7.5 MHz	2 kHz
Trigger	Pulse Amplitude	Pulse Energy	Impedance	Damping
Internal	-475 V	152.78 µJ	low-Z	59 Ω

In addition to setting the front panel manual controls, the rear panel must be connected to the correct desired configuration. For a pulse-echo mode operation, the Tx/Rx transducer is connected to the BNC

connector labelled T/R. For an internal trigger configuration, the DPR300 Trig./Sync connector is connected to the external trigger input of the monitoring device. The DPR300 BNC connector labelled Receiver Out is connected to the input of the signal acquisition block (the echo receiver circuit). The connections are shown in Figure 6.2B.

6.1.2 Signal acquisition block

The signal acquisition block takes as input the US echoes, received from the output of the DPR300, and the signal of a commercial pressure sensor. The US echoes are conditioned by the echo receiver peak detector circuit (as described in Chapter 5) and, in combination with the pressure signal, is acquired by a two-channel PC-oscilloscope and saved for offline post-processing.

The commercial pressure sensor ABPDANT005PGAA5 (Honeywell International Inc, 2020), depicted in Figure 6.3A, was used for pressure validation. The piezoresistive silicon pressure sensor is supplied with 5 V and has a pressure range from 0 psi to 5 psi. It is necessary to bypass the voltage supply with a 0.1 µF capacitor and the output with a 0.001 µF capacitor, both connected to the ground, as seen in Figure 6.3B.
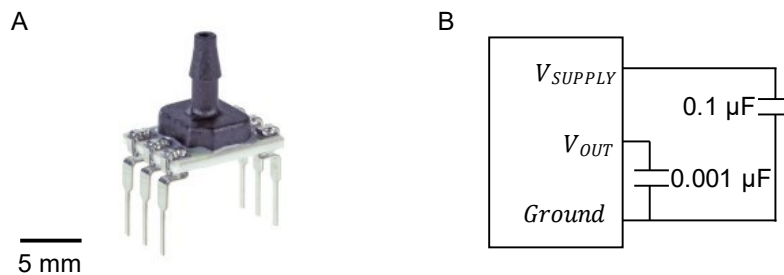
Figure 6.3: Commercial pressure sensor. The (A) piezoresistive silicon pressure sensor, with (B) external capacitors connected for voltage bypassing, was used for pressure measurement validation in the experimental setup. Adapted from (Honeywell International Inc, 2020).

The transfer function of the pressure sensor is given by Equation 6.1, where $P_{applied}$ is the pressure measured by the sensor and V_{out} is the voltage at the output that is proportional to the difference between applied pressure and atmospheric (ambient) pressure.

$$P_{applied} = (V_{out} - 0.5) \cdot 1.25 \tag{6.1}$$

A PicoScope 5243D was used for digitizing and saving the analog signals. The two-channel PC-oscilloscope, shown in Figure 6.4, is connected to the computer through a 3.0 USB cable in the rear

panel. Furthermore, as previously mentioned, a connection between the DPR300 BNC Trig./Sync and the scope External Trigger is established.
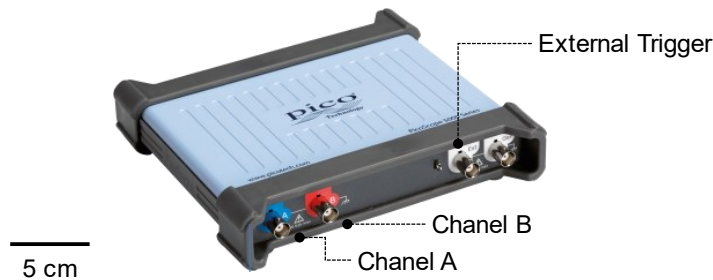
Figure 6.4: PC-oscilloscope. The PicoScope 5243D was used for acquiring the ultrasound signal echoes and the pressure measurements. Adapted from (Pico Technology Ltd, 2018).

The PicoScope features the Pico FlexRes, a system of flexible resolution that allows reconfiguration of the scope hardware to increase either the sampling rate (<1 Gsamples/s) or the resolution (8-16 bits) (Pico Technology Ltd, 2018, 2020). A study of the cost between sampling rate and resolution (shown in Appendix A6) revealed that the best configuration was to set the sampling frequency (f_s) to 500 MHz and the vertical resolution to 8 bits. The scope window was set to 50 μs (expect for the test with pressure controlled by the syringe, in which the window was set to 20 μs), in which both vessel wall reflections are captured. After defining an optimized trigger, rapid mode triggering is selected and the buffer is set to the maximum, saving the highest number of frames possible, each frame containing a triggering event (one pulse and corresponding reflections). As the scope has limited memory (capture memory shared between active channels: 256 Msamples in 8 bits mode, 128 Msamples in 12 bits or higher mode), the number of frames saved in the buffer depends on the resolution configuration. For a time resolution of f_s=500 MHz, an ADC resolution of 8 bits, and a PicoScope window of 50 μs, the maximum number of frames allowed to be saved correspond to 5,349. A total of 5,000 frames were captured, resulting in a test time of 2.5 s, as each frame is captured at the PRF rate. With the same PicoScope resolution and a scope time window of 20 μs, it is possible to capture 10,000 frames (5 s of running test time). Each frameset was saved in MAT-file format.

6.1.3 Offline post-processing

With the data signals saved in MAT-file format, offline post-processing can be initiated. All processing was performed in the MATLAB® environment. Post-processing is first applied at each frame containing both channels and then in the set of frames from one experimental test. Different algorithms are applied to

each channel dataset in parallel. Figure 6.5 shows the process implemented on the pressure signal channel, from which the pressure waveform measured from the commercial pressure sensor is extracted, and Figure 6.6 summarizes the process implemented on the echo signal channel, in which a derived pressure waveform is extracted.
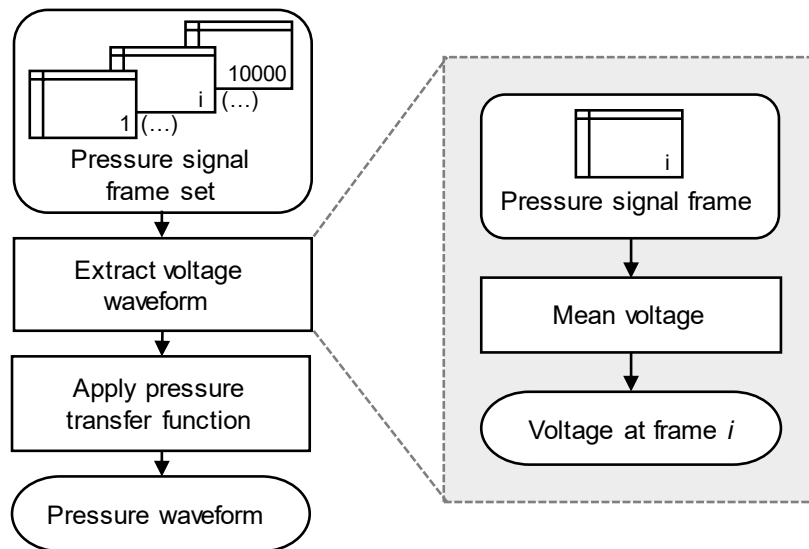
Figure 6.5: Offline post-processing of the voltage pressure signal. The mean voltage of each frame is calculated, and the voltage waveform of the test is extracted. After applying the pressure transfer function (Equation 6.1), the pressure waveform measured by the piezoresistive pressure sensor is derived.

The post-processing of the pressure sensor channel, described in Figure 6.5, is simple. At each frame, the pressure voltage signal is constant, only varying through the set of frames. A mean value of each frame, for the last 1,000 samples acquired, is calculated and used as the pressure voltage of the corresponding frame. After applying the process to every frame, a voltage waveform can be extracted and the pressure sensor transfer function is applied (Equation 6.1), obtaining the final pressure waveform.

Offline post-processing of the US echo signal frames starts by extracting a diameter value from each frame, as seen in Figure 6.6. First, each frame is studied individually. A digital lowpass filter ($fpass$=5 MHz, with a stopband attenuation of 60 dB and 3 dB bandwidth of 19.836 MHz) is applied over the data to increase the SNR. Then, an anterior and posterior time window extract the data of interest, containing the reflection from the anterior and posterior vessel wall, respectively. A local maxima function is applied over each window, determining the echo time at which the maximum voltage amplitude happens. TOF is calculated by subtracting the voltage peak timestamp of the posterior wall from the voltage peak timestamp of the anterior wall. Now, the diameter value of the frame under test can be

calculated by applying Equation 2.25, where 1,543 m/s was used as the speed of sound in distilled water and was determined experimentally (see Appendix A7).
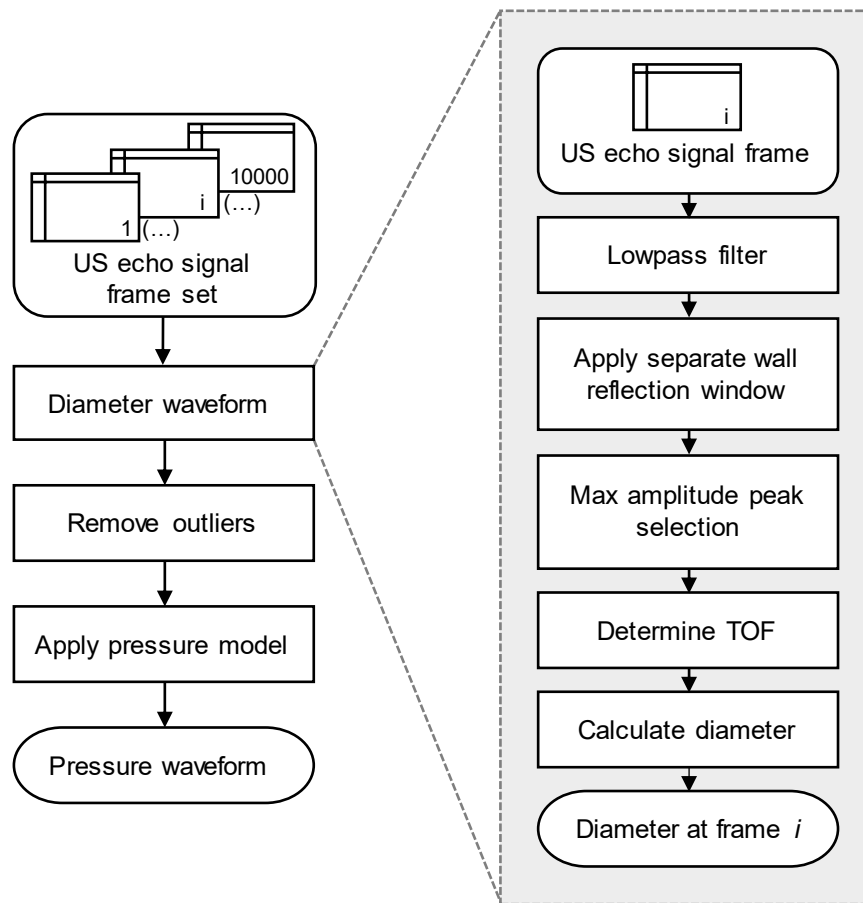
Figure 6.6: Offline post-processing of the US echo signals. The TOF between the anterior and posterior wall is determined by extracting the maximum peak timestamp in each reflection window. The diameter at each frame is calculated through the TOF and the distension waveform of the test is extracted. Outliers are removed and the pressure model is applied. The pressure waveform has been derived through the diameter waveform.

After implementing the process above to each frame, a diameter waveform has been determined, with a sampling rate corresponding to the PRF. Due to possible interferences or unusual wall reflection acquisition, a diameter frame reading could be incorrect, so removal of outliers from the diameter waveform is necessary. A moving median filtering, with a window size of 50 elements, is applied to the diameter waveform. After filtering, the diameter waveform is taken as input in the BP model and calibration is done with the minimum and mean pressure (with FF=0.412 in Equation 2.2) calculated from the pressure waveform acquired from the commercial pressure sensor. Finally, the diameter-derived pressure waveform is obtained.

6.1.4 Mimicking arm: syringe-controlled pressure experimental test

The first experimental test was conducted with a mimicking arm composed of a fixed silicone tube immersed 4 mm deep in a tank filled with distilled (DI) water. The silicone tube, with an inner diameter of 2.8 mm and thickness of 1 mm that were measured with electronic callipers (Powerfix, OWIM GmbH, Neckarsulm, Germany), mimics the radial artery. The DI-water emulates the forearm and is also used as the blood mimicking fluid. Pressure is manually controlled with a syringe and, to maintain pressure, two valves are introduced at the inlet and outlet of the mimicked artery. Figure 6.7 shows the described mimicking arm, ultrasound sensor complex and signal acquisition block for the first test.
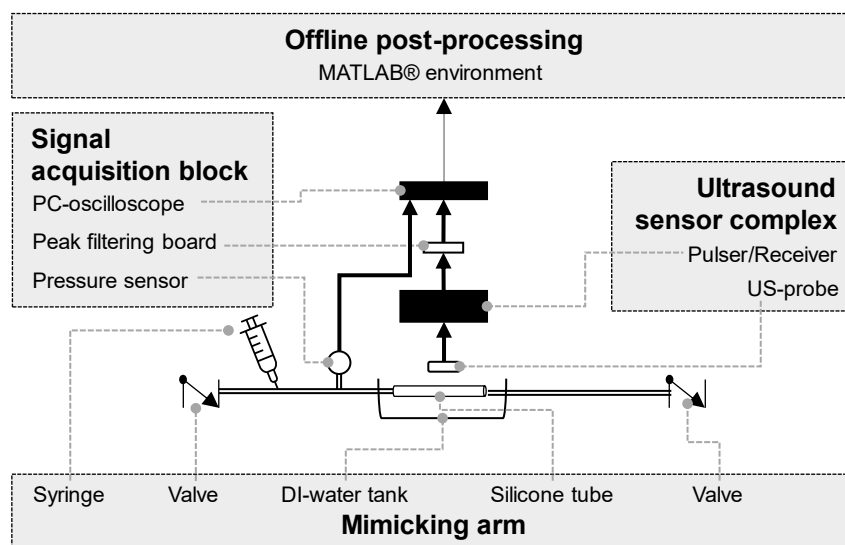
Figure 6.7: Syringe-controlled pressure experimental setup. The double line corresponds to the blood mimicking fluid flow path, thick arrows correspond to the analogue signal path, thin arrow corresponds to the digital data path and dashed lines indicate the components legend.

Before carrying out any test, a measurement at resting diameter was first performed, where the raw ultrasound echoes, before peak detection filtering, were taken as input into the PicoScope instead of the pressure sensor signal. This served as verification of probe positioning and US echo quality.

After validation of probe positioning, the test began. The pressure was manually applied before the pressure sensor saturation point (5 V), while the PC-oscilloscope was acquiring the consecutive frames until its buffer was full. Data underwent post-processing, and the derived pressure waveform from the ultrasound sensor was compared to the pressure waveform recorded by the commercial pressure sensor.

6.1.5 Mimicking arm: cardiovascular pressure experimental test

A centrifugal heart-like pump, the Zentrifugalpumpe MultiFlow (GAMPT mbH, Merseburg, Germany), replaced the syringe in the previously described setup as the pressure controlling device. The pump, shown in Figure 6.8A, can be set to five different programs that change the pumping flow pattern. Mode 0 and 1 (m0 and m1) sets the pump to a constant flow, but while m0 displays the flow velocity in revolutions per minute (rpm), m1 displays the flow speed in litres per minute. Mode 2 (m2) regulates the flow to a negative sawtooth configuration (see Figure 6.8B), which requires, additionally to the flow velocity, the configuration of a pulse duration time. The pump's mode m2 was chosen for heart-mimicking due to its characteristic heart-like pumping waveform. The remaining pump modes were not used during this work. Every time the pump is turned on, the flow velocity must be slowly increased, starting at zero until the desired value. For this reason, every test that is conducted with the pump was initiated in mode m0 and after reaching the needed flow velocity, the mode was changed to m2.
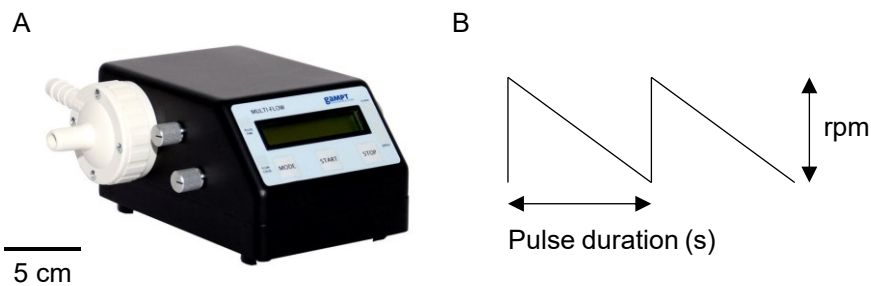
Figure 6.8: Heart-like centrifugal pump. (A) The pump is used for heart-mimicking with (B) its characteristic heart-like negative sawtooth pulse configuration in mode 2 (m2). Adapted from (GAMPT mbH, 2020).

Aside from replacing the syringe with the centrifugal pump, the experimental setup remained the same, as seen in the schematic shown in Figure 6.9.

After validation of probe positioning, as described in the previous section, the pump was set to m2, a pulse duration of 1 s was selected and a flow velocity of 800 rpm was adopted. As the scope's buffer memory is limited (256 Msamples shared between active channels), 5,000 frames were collected, corresponding to 2.5 heartbeat cycles (sampling rate at 0.5 ms, PRF set to 2 kHz).
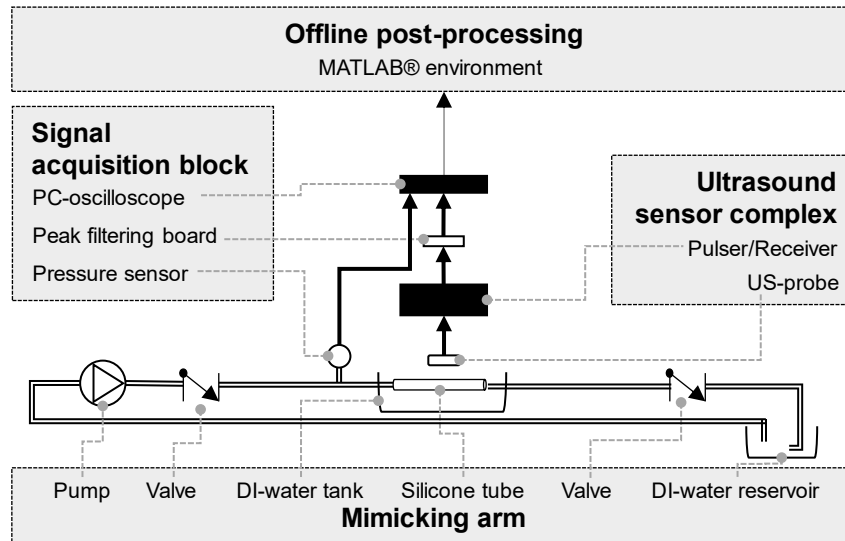
Figure 6.9: Cardiovascular pressure experimental setup. The double line corresponds to the flow path, thick arrows correspond to the analogue signal path, thin arrow corresponds to the digital data path and dashed lines indicate the components legend.

6.1.6 Mimicking arm: porcine artery experimental test

In a final test, the experimental setup shown in Figure 6.9 was adapted with slight changes, where the silicone tube was substituted by a porcine artery. The inlet and outlet of the artery were attached by ligation with a suture thread to two metal male hose barb adapters acting as a connector between the artery and the flow circuit. The mimicked radial artery had a wall thickness of (0.68±0.10) mm, an inlet inner diameter of (5.13±0.11) mm, and an outlet inner diameter of (3.67±0.05) mm (measured with electronic callipers). The liquid used for forearm and blood mimicking was changed to a saline solution ($\%w/w$=0.9 %) in order to prolong the artery's viability by maintaining a similar physiological osmotic pressure (Widman et al., 2016).
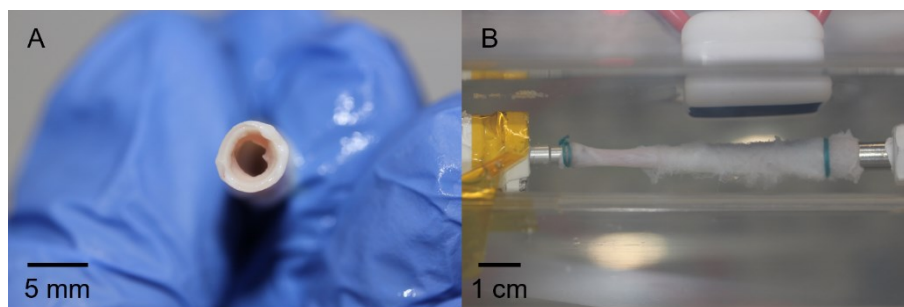
Figure 6.10: Porcine artery experimental test. A porcine artery (A) with an outlet inner diameter of 3.67 mm and wall thickness of 0.68 mm was (B) placed in the experimental setup by ligation to the male hose fitting metal parts.

After finding the probe's optimal position, the pump was set to m2 (pulse duration at 1 s and flow velocity at 800 rpm). The *ex-vivo* test was performed, post-processed and the results were afterwards analysed.

6.2 Results

In this section, the results of the experimental setups are presented. First, an example of the ultrasound reflections and corresponding signal filtering with the designed board is shown. Second, an example frame of the acquired signals (the echo receiver output and the pressure voltage signal) is depicted. Third, the diameter and pressure measurements from each designed setup are shown. Additionally, a comparison between the silicone tube and the porcine artery walls' reflections is made.

6.2.1 Ultrasound signal and echo receiver filtering

The pulser sends a pulse to the transducer and through the piezoelectric effect, the electric signal is converted to ultrasound waves. The signal is then reflected to the transducer at each acoustic impedance interface. An exemplary ultrasound signal and the corresponding filtered signal by the echo receiver circuit are depicted in Figure 6.11. The signals were extracted from the experimental setup with the silicone tube. The PicoScope sampling frequency is 500 MHz with a voltage resolution of 39.063 mV.
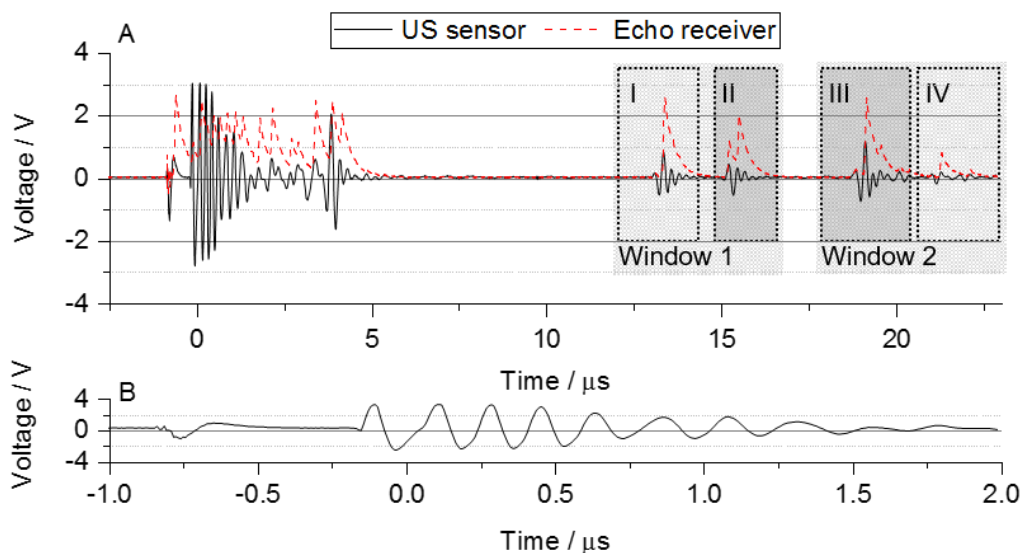
Figure 6.11: Ultrasound echo signal and filtering. (A) The reflections received by ultrasound are a combination of the transmitted pulse and PUT reflections inside the package, followed by the vessels' walls reflections. The echoes produced by the anterior wall (window 1: echo I and echo II) and posterior wall (window 2: echo III and echo IV) are distinguished by a temporal interval. The reflections of the inner walls are identified by a dark-grey shaded area. The signal is filtered and amplified (dashed line) by the echo receiver circuit. (B) Transmitted pulse.

The first group of reflections corresponds to the transmitted pulse (represented in Figure 6.11B) and the echoes from the transducer package. After approximately 13 µs, the first refection from the vessel's walls is received by the transducer. Two windows of echoes are distinguished by a temporal interval where no reflection is recorded. The two echoes in the first window correspond to the reflection of the vessel's anterior wall, that is, echo I is the reflection from the outer wall of the anterior wall and echo II is the echo produced by the inner wall of the anterior wall. The second window of reflections happens at the posterior wall, echo III corresponds to the inner wall and echo IV to the outer wall. Furthermore, a phase inversion in the echo-signals at each wall reflection is noted.

6.2.2 Echo receiver signal and pressure sensor

In the experimental setups, both the US signal, after being filtered and amplified, and the pressure voltage signal measured with the commercial pressure sensor were acquired in parallel by the PC-oscilloscope at each triggering event. A representative frame is depicted in Figure 6.12. Interference noise is seen on the pressure sensor signal at each pulse emitted by the transducer. Post-processing was applied to each frame to determine the pressure signal's mean voltage (of the last 1,000 samples) and the wall's reflections TOF from the US signal.
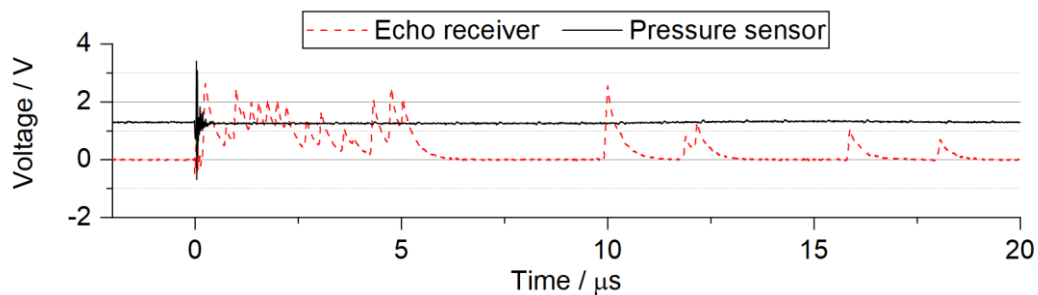
Figure 6.12: Exemplary frame acquired by the PC-oscilloscope. During the experimental tests, frames were acquired when a triggering event was captured by the scope (at the pulser PRF rate). Each frame was composed of the US signals after amplification and filtering and of a constant voltage value measured by the commercial pressure sensor. The PicoScope sampling frequency is 500 MHz with a voltage resolution of 39.063 mV.

6.2.3 Syringe-controlled pressure experimental test

The first experimental test consisted of manually applying pressure to the syringe connected to a silicone tube (see experimental setup description in Section 6.1.4). Figure 6.11 is one exemplary frame measurement taken from this test, with the silicone tube as the mimicking radial artery. The calculated tube's luminal diameter, depicted in Figure 6.13A, was determined by the vessel's walls TOF, and the

curve was used to derive the pressure waveform by applying the linear model (M1). The diameter derived pressure is compared to the pressure measured by the piezoresistive pressure sensor in Figure 6.13B. An initial resting diameter (with no positive pressure applied) of 4.450 mm was measured and converted to 26.118 mmHg, increasing to a maximum of 4.500 mm and 247.160 mmHg for the highest diameter distension. The diameter measured at the end of the test and converted pressure were inferior to the initial value. The pressure sensor measured an initial and final pressure of -23.384 mmHg and a maximum of 247.160 mmHg.

Figure 6.13: Syringe-controlled pressure test results. (A) Diameter waveform measured through the TOF of the wall's reflections. (B) Pressure waveform measured through the piezoresistive pressure sensor (dashed line) and the derived pressure from the diameter curve (straight line). Diameter resolution of 1.5 μm (determined with $c_{DI\text{-}water}$=1,513.226 m/s), pressure resolution of 2.5 mmHg (in the measurement with the pressure sensor) and 0.5 ms of temporal sampling.

6.2.4 Cardiovascular pressure experimental test

The diameter, US derived pressure and measured pressure in the cardiovascular experimental test are seen in Figure 6.14. The diameter waveform is characterized by a fundamental negative sawtooth configuration with a characteristic two-peak at the maximum value of the sawtooth and one small peak close to the end of the cycle. The minimum diameter measured was 4.435 mm, to which maximum diameter distension of 28 μm was obtained. When comparing the pressure curves, the US derived pressure waveform overestimates the pressure measured by the piezoresistive sensor during the whole cycle. The minimum and maximum pressure values of the first full "heart" cycle were determined from the pressure waveform measured by the piezoresistive pressure sensor for calibration of the linear

pressure model (M1). Diastolic and systolic values of 7.707 mmHg and 279.346 mmHg, respectively, were then attributed to the MAP calculation, and its value used for calibration. The derived pressure waveform has its minimum and maximum value at 7.707 mmHg and 360.127 mmHg, respectively, obtaining an error of 80.781 mmHg at the maximum peak. When looking at the second peak in the first curve, the US derived pressure overestimates the actual pressure by 28.813 mmHg. The mean curve error was (27.450±22.377) mmHg.
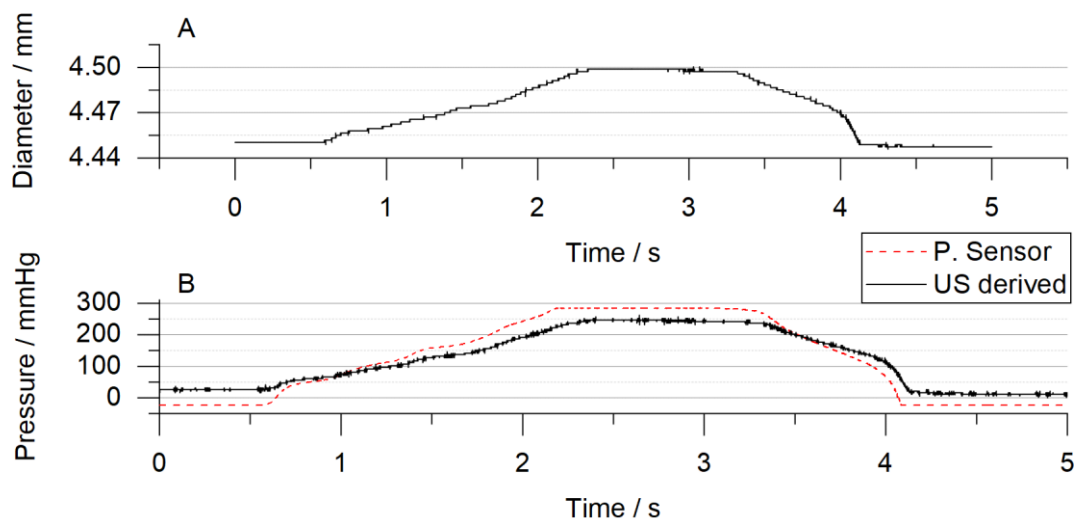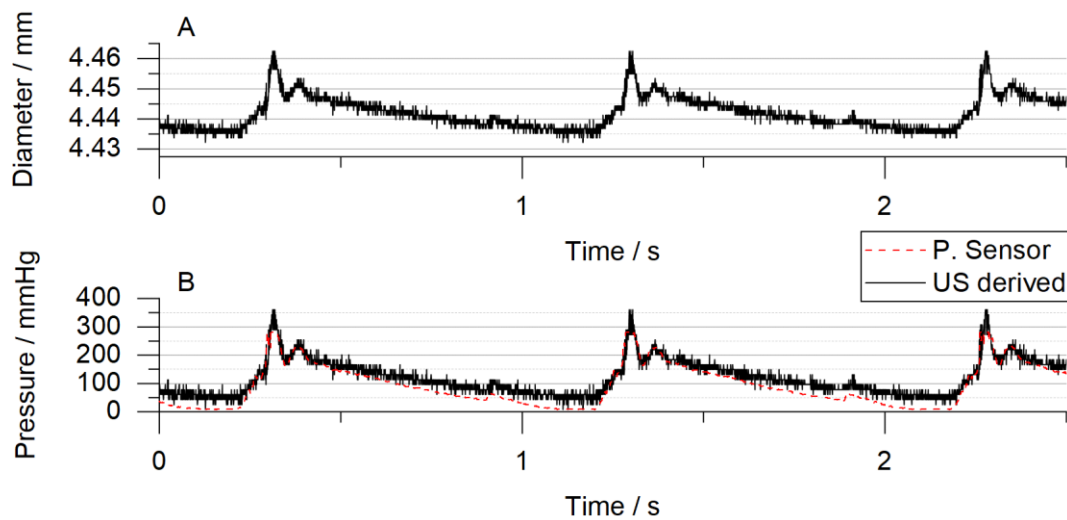

Figure 6.14: Cardiovascular pressure test results. (A) Diameter waveform measured through the TOF of the wall's reflections. (B) Pressure waveform measured by the piezoresistive pressure sensor (dashed line) and the derived pressure from the diameter curve (straight line). Diameter resolution of 1.5 μm (determined with $c_{DI\text{-}water}$=1,513.226 m/s), pressure resolution of 2.5 mmHg (in the measurement with the pressure sensor) and 0.5 ms of temporal sampling.

6.2.5 Comparison between vessels

The comparison of the echo measurements in the silicone tube with the porcine artery is shown in Figure 6.15. The amplitude of the echoes in the porcine artery (0.43 V for the inner anterior wall and 0.19 V for the inner posterior wall) is reduced if compared to the silicone tube (0.44 V and 1.55 V, respectively). Furthermore, it is noticeable that the phases at each interface are inverted between the silicone tube and the porcine artery (e.g., the phase of the echo I is inverted when comparing both vessels). When looking at the anterior wall window, echo I had the highest amplitude, whilst in the porcine artery, it was echo II. The time between inner and outer wall echoes also decreased considerably in the porcine artery but both echoes remain distinguishable.
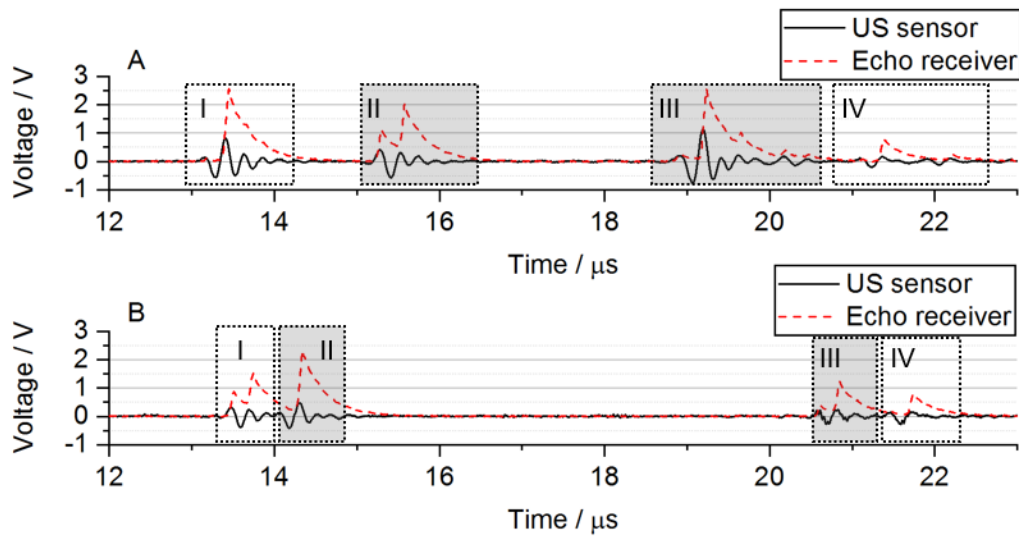
Figure 6.15: Comparison of the echo profile between vessels. (A) Echo profile from the silicone tube. (B) Echo profile from the porcine artery. The PicoScope sampling frequency is 500 MHz with a voltage resolution of 39.063 mV.

6.2.6 Cardiovascular pressure with the porcine artery experimental test

The silicone tube in the experimental setup described in Figure 6.9 was exchanged by a porcine artery and the diameter was acquired by the custom fabricated ultrasound sensor (described in Chapter 4) and developed algorithm (described in Section 6.1.3). In Figure 6.16 the signals of the echo receiver for 1,120 frames (0.56 s) are depicted, where the red dots indicate the maximum peak of each window in each frame. Figure 6.16B is a custom representation of an M-Mode ultrasound image, in which the time motion of the ultrasound wave along a chosen ultrasound line is displayed. Figure 6.17 shows the results of the determined diameter curve, the commercial pressure sensor measurements and the pressure curve when applying M1 to the artery's distension measurements. The minimum diameter measured was 4.115 mm, distending up to 5.528 mm. The US derived curve follows the pressure curve measured with the commercial sensor with an initial underestimation (during the systolic phase of the cycle). The Pearson's linear correlation between the obtained pressure waveform when applying M1 and the pressure measured by the commercial pressure sensor was of r=0.994 and mean difference of (0.544±2.315) mmHg. The SBP error was of -2.131 mmHg.
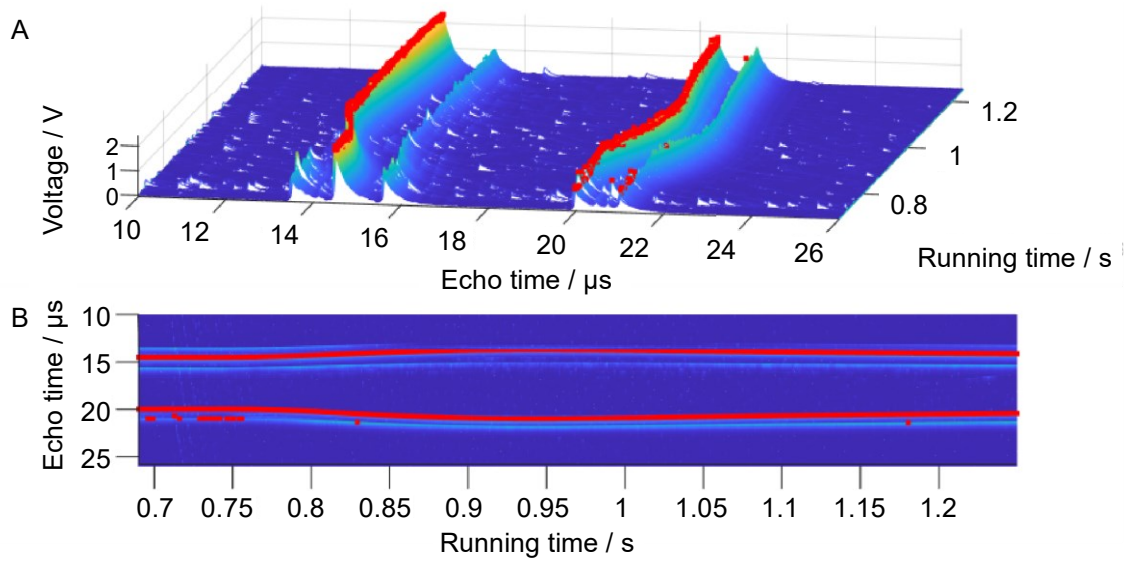
Figure 6.16: Multi-dimensional representation of a section of frames. The chosen peaks (maximum voltage on each reflection window) by the algorithm are identified in red. (A) 3D representation of the echo receiver output. (B) 2D representation of the amplitude of the echo receiver output (similar to an M-Mode image in a medical ultrasound device). The PicoScope sampling frequency is 500 MHz with a voltage resolution of 39.063 mV, and 0.5 ms of temporal sampling.
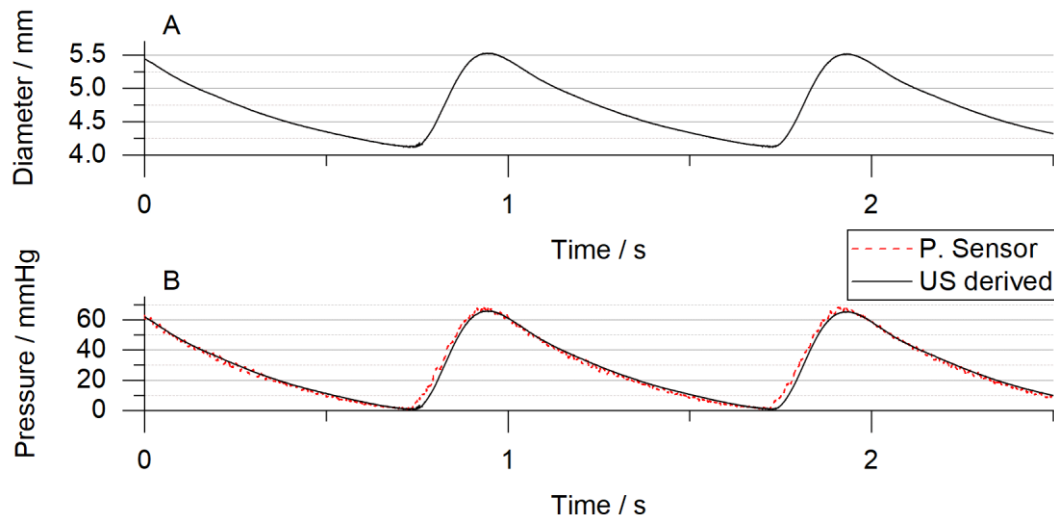
Figure 6.17: Cardiovascular pressure test results with an artery. (A) Diameter waveform measured through the TOF of the wall's reflections. (B) Pressure waveform measured by the piezoresistive pressure sensor (dashed line) and the derived pressure from the diameter curve (straight line). Diameter resolution of 1.5 μm (determined with $c_{DI\text{-}water}$=1,513.226 m/s), pressure resolution of 2.5 mmHg (in the measurement with the piezoresistive sensor) and temporal sampling of 0.5 ms.

6.3 Diameter acquisition analysis

In this section, analysis of the diameter acquisition system is discussed for both types of mimicking radial arteries, the silicone tube and porcine artery. Furthermore, the echoes from both vessels are compared.

6.3.1 Silicone tube diameter assessment

For both experiments with the silicone tube, the measured resting diameter was approximately 1.6 mm higher than the true value (2.8 mm of true inner diameter manually measured with callipers, see Section 6.1.4). This error happened because the TOF of the maximum peaks of each vessel wall reflection window did not correspond to the inner diameter of the tube, but the sum of the inner diameter and the thickness of the anterior wall. The diameter calculation algorithm extracts the maximum of each window (see Figure 6.11), and in most measurements with the silicone tube, this corresponded to the outer wall of the anterior wall (window 1) and the inner wall of the posterior wall (window 2). The inner diameter plus the thickness of the tube is 3.8 mm, which is still higher than the measured distance (4.44 mm). In the algorithm for diameter extraction, the speed of sound was assumed to be constant and equal to the measured value of speed in DI-water (1,513.226 m/s, see Appendix A7). The velocity of sound in silicone (919 m/s (Yamashita et al., 2007)) is smaller than in water, and therefore, for a correct assessment of the tube's thickness contribution in the measured distance, the TOF between the outer and inner anterior wall should be calculated with the correct velocity. If taking into account the actual speed of sound in silicone, and extracting the TOF between the peaks of the outer and inner wall of the anterior wall (echo I and echo II in Figure 6.11), the calculated thickness is of 989.76 μm, and the calculated inner diameter (by extraction of TOF between the inner anterior and posterior wall, echo II and III, respectively) is of 2.821 mm. This accounts for 21 μm diameter error and a smaller error in thickness (10.24 μm). For the pressure derivation, the errors in overestimation of the absolute diameter measurement do not account for an incorrect pressure conversion, as the mathematical pressure model employs a linear relationship of the diameter curve and calibrates it to diastolic and mean pressure. If the same peaks are being taken into TOF calculation at each frame for the whole set, the conversion to pressure waveform is correct.

6.3.2 Porcine tube diameter assessment

The echoes from the wall in the silicone tube were larger than from the porcine artery, which is due to a higher acoustic impedance mismatch and corresponding intensity of the reflection coefficient (by applying

Equation 2.23, silicone/DI-water: I_r=42.81·10⁻⁵; soft tissue/saline solution: I_r=3.585·10⁻⁵). However, these differences in acoustic impedances are not the only influencing factor, it is highly probable that the decrease in echo amplitude in the porcine artery is in part due to probe positioning. Moreover, whilst in the experimental setup with the silicone tube, the "soft-boundary" and phase inversion happens at the silicone/DI-water interface, in the porcine artery setup it happens at the saline solution/porcine artery setup, due to the relation between acoustic impedances (refer to Section 2.3.1 for US propagation boundary theory).

With the maximum peaks of each window at the inner wall of the anterior and posterior wall, the algorithm was capable of correctly determining the diameter of the porcine artery. Bearing in mind that between the cardiovascular pressure measurement with a silicone tube and the porcine artery, the device's parameters were the same, the diameter curve measured with the porcine artery was smoother and a maximum distension of 1.413 mm was measured. The disappearance of the second peak in each cycle and the smooth characteristic of the diameter curve in the porcine artery is due to the high distensibility of the vessel, allowing for more storage of fluid volume.

6.4 Pressure acquisition analysis

The derived pressure in each experimental test is analysed in this section, as well as the stiffness of each vessel used (silicone tube and porcine artery).

6.4.1 Silicone tube stiffness

In both experimental tests with the silicone tube, the maximum distension that was possible to obtain was 63.875 μm (with the syringe). The tube revealed to be too stiff, with a much higher stiffness index (β=543.420, calculated through Equation 2.5, data from the test with the syringe) if compared to the radial artery (β=9.5, calculated through Equation 2.5, data from the database). For further research, a tube or mimicked artery (phantom) should be used with characteristics more similar to an artery, with a higher distensibility.

6.4.2 Syringe-controlled pressure and compliance

When using the mimicking arm with the syringe-controlled pressure (setup description in Section 6.1.4), the commercial pressure sensor measured an initial and final pressure that was negative and of the same value (refer to Section 6.2.3). The negative pressure reading is possible to be due to a vacuum pressure

applied to the syringe by pulling the plunger back whilst both valves in the setup were closed and, therefore, creating a negative pressure. However, it should be noted that the diameter measured at the beginning and end of the test was different, and, consequently, there was a different pressure in the tube at both moments of the test. The piezoresistive pressure sensor working pressure range is from 0 psi to 5 psi, but the output voltage is clipped at a lower limit of 0.125 V, corresponding to -0.469 psi (pressure sensor transfer function in Equation 6.1). It is concluded that at the beginning and end of this test, the sensor was saturated at its minimal value.

The diameter waveform is converted to pressure waveform by applying the best performing model, which calibrates the curve to the diastolic and mean pressure measured by the piezoresistive pressure sensor. In a physiological setting, no negative blood pressure would be measured, and therefore it was attributed a safeguard in the processing algorithm. If the measured pressure was negative, the wave would be calibrated to an end-diastolic pressure of 1 mmHg to ensure a positive pressure waveform. The positive initial and end value in the derived pressure is attributed then to the processing algorithm. Although this calibration safeguard wouldn't be expected to come into play in a clinical setting, it should be revised to incorporate possible failure modes.

6.4.3 Cardiovascular pressure with silicone tube

As the curve is calibrated to the diastolic (minimum) value measured by the pressure sensor for the first full "heart cycle", the error associated with the minimum curve value is zero. However, at the tests performed with mimicking arm composed of a silicone tube and a heart-like pump (refer to Section 6.2.4), it is noted that due to the stiffness of the tube and small distension, the variability of the derived pressure is very high. A variability of 3 μm (two times the resolution), when converted to the derived pressure is 26.808 mmHg. Therefore, it can be said that the mean curve error is due to the variability of the diameter reading. Additionally, more errors can be attributed to the saturation of the maximum pressure measured by the piezoresistive sensor. The pressure sensor was not able to measure the maximum pressure in the tube, and the pressure waveform is saturated. The maximum diameter derived pressure is higher than the saturated pressure value, and an error of 80 mmHg was measured between the derived and measured pressure. However, it is expected that the real systolic value error would be inferior if the pressure measurement had not saturated.

6.4.4 Cardiovascular pressure and stiffness index with the porcine artery

The initial underestimation seen between the US derived pressure and the pressure curve measured by the pressure sensor at the test with the porcine artery (refer to Section 6.2.6), followed by a slight overestimation in pressure during the diastolic phase is due to the characteristic hysteresis in the compliance curve of arteries. The pressure curves are much smoother when compared to those extracted from the silicone tube, which was due to a much smaller stiffness index (β=15.360, calculated through Equation 2.5, data from the test with the porcine artery) and highly more compliant vessel, which more closely predicts the assessment of the measurement principle at the radial artery for a wrist wearable sensor. When using the compliant porcine artery, a completely different error profile is seen when compared to the silicone tube. The decrease in stiffness of 97.173 % (from the silicone tube to the porcine artery) led to an acute decrease in error, now with a 2.131 mmHg of underestimation in the systolic pressure and a mean curve error of (0.544±2.315) mmHg.

The *ex-vivo* study revealed a better correlation (r=0.994) than *in-silico* (r=0.978). This may be because the models' calibration in *ex-vivo* was done by using the in-site pressure sensor's DBP and MAP recordings. Thus, the calibration was performed specifically to the measured artery (radial) and not to the brachial artery, which decreases the error of the derived pressure, but it is not a realistic calibration procedure in a practical application.

6.5 Ultrasound-based diameter assessment algorithm analysis

The ultrasound-based diameter assessment algorithm presented in Figure 6.6 determines TOF between the vessel's inner walls by selecting the maximum peak on each reflection wall window. However, the amplitude of each reflection and its ratio to other reflections are directly related to the very sensitive PUT positioning and angling towards the vessel. That is, while with one position, the inner wall might have the highest amplitude of the reflection window, with a slightly different position, it would be the vessel's outer wall. This problem could be resolved by introducing an array of PUTs, which with signal processing, would allow the selection of the piezo directly over the artery and extraction of the corresponding measured signals. The introduction of an array of US sensors would, however, increase drastically the complexity of the system. It should also be noted that with a more sophisticated signal processing algorithm, all diameters could be extracted from the signal, that is, the inner and outer diameter, as well as the thickness of each wall.

Furthermore, a phase inversion is often seen in the ultrasound echo signal. Theory dictates that an inversion in the phase of the reflection happens at a "soft boundary" when the acoustic impedance in which the wave is propagating is higher than the impedance of the reflecting material. In the initial setup, the water/silicone interface is a "soft boundary". In the setup with the porcine artery, the artery/saline solution is a "soft boundary". In the human body the same is true, with blood instead of saline solution (see Appendix A1 for acoustic impedance values). No matter which material the ultrasound is travelling through, in a conceptual "vessel wall/fluid/vessel wall" pair of interfaces, there will always be a phase inversion in one of the inner walls. That is, the pair of gaussian echoes corresponding to the vessel's inner walls will always be out of phase with each other and the positive maximum peak of each reflection will not correspond to the same position in each waveform echo. During this work, only a half-wave rectifier was employed, and the maximum peaks are chosen for TOF calculation. A full-wave rectifier should be developed to solve the mentioned out-of-phase issue, and its envelope or maximum peak should be then efficiently detected for a correct TOF assessment between the vessel's walls.

6.6 Key findings

Three different experimental setups were created, in which the mimicking arm was modified, with pressure controlled either by a syringe or a heart-like pump in a silicone tube as a mimicking radial artery or the heart-like pump combined with a porcine artery. The simple mimicking arms allowed for preliminary system validation, addressing RQ3, from which assessments were made about the system.

First, the theoretical working principle (introduced in Section 3.5) when paired with the echo receiver circuit (discussed in Chapter 5) and combined with the rest of the setup was validated. The measurements with the porcine artery provided the best results (mean error difference of (0.554±2.315) mmHg), due to a stiffness index closer to the real value of the radial artery.

On one hand, if the echo receiver circuit is not modified to include a full-wave rectifier, improvements in the diameter extraction algorithm should be focused on taking into account the phase inversions of the US wave at "soft" acoustic boundaries. On the other hand, additional arterial information could be extracted from the conditioned acquired US signal that should also be explored. For instance, the thickness of the arterial wall can also be extracted from the acquired conditioned echo signal, by enhancing the post-processing algorithm.

7 CONCLUSION AND OUTLOOK

The present work provides a novel *in-silico* analytical comparison between different models that relate arterial pulse waves to the pressure waveform for continuous, non-invasive monitoring of arterial health parameters. An electronic system for BP measurement through US was developed and validated with a commercial pressure sensor in an *ex-vivo* experimental setup. The most important reflections and findings follow:

- To the best of my knowledge, it was the first time BP models were analysed and qualitatively compared in a variable dataset at different arteries. The study enabled a site-specific approach for calibration design.

- The linear model was revealed to be the most accurate for measurements at the radial artery. The results showed an *in-silico PP* correlation of 0.978 and a mean difference of (-2.134±2.477) mmHg.

- The developed echo receiver circuit was able to filter the raw US signals to the required conditions for signal post-processing. A specific post-processing algorithm was employed and correctly determined the maximum peaks of each reflection window.

- The developed system enabled the extraction of the diameter waveform and local stiffness, functioning in both the silicone tube mimicking artery and in the porcine artery.

- The *ex-vivo* system validation revealed a pressure correlation of 0.994 and a mean difference of (0.554±2.315) mmHg. Thus, with the linear model, the US measurement complies with the ISO standard (ISO 810-602:2018, 2018), with deviations lower than 5 mmHg.

The proposed hypothesis was: can an electronic system be developed to measure BP through a US-based approach that extracts hemodynamic pulse waves? This work resulted in a proof-of-concept for such a device, where many issues during the study were uncovered and need to be further researched. Nonetheless, the hypothesis has been validated. First insights into a clinical device and improved software/hardware development have been accomplished. This project brought the ultrasound device development a step closer to a real wearable device that can be used to non-invasively and continuously measure blood pressure and other critical vital parameters.

Future work can be approached from two different fronts: the improvement of the system developed here and advancing the research in the standardization of non-invasive devices for measurement of BP.

The improvement of the processing algorithm depends on the analogue signal output. If a full-wave rectifier is developed, then there is more confidence in the correct selection of each reflection's peak. Furthermore, different methods should be studied to derive the most accurate TOF between the reflections of each inner wall. A more sophisticated algorithm could derive additional vessel's characteristics, including the vessel's outer diameter and each wall's thickness change during the cardiac cycle.

In future work, all subsystems, including the pulser, switch-receiver block and data processing should be incorporated into a wrist-wearable. The challenge of the conversion of circuitry to a flexible PCB for easier adaptation to the wrist curvature should be studied (Y. Chen et al., 2020; Cho et al., 2020; Sterken et al., 2011), including adapting the working sensor to a soft ultrasonic probe (Dagdeviren et al., 2016; Park et al., 2016; Peng et al., 2021; Sempionatto et al., 2021; Wang et al., 2018). After the system integration, clinical human trials for validation of the device should be the next step. When successful, the goal of continuous recording of BP signals in a comfortable, long-term, and non-invasive manner would be achieved.

In recent years, a new hypothesis suggests that it is the central waveform that indicates the stress on the major organs, rather than the peripheral pulse wave. Additionally, various clinical anti-hypertension treatments are reported to exert different influences on the central and peripheral arteries (Laurent et al., 2016). Due to its possible greater clinical relevance, central BP could provide superior diagnostic and prognostic value. A transfer function could be applied to derive central BP from a radial BP waveform (Gao et al., 2016). However, there are no standardized protocols for device validation regarding PW recording, transfer functions/model use, and calibration procedure (Sharman et al., 2017; Stergiou et al., 2016), making way for future research and development in this field.

REFERENCES

Alastruey, J., Parker, K. H., & Sherwin, S. J. (2012). Arterial Pulse Wave Haemodynamics. In S. Anderson (Ed.), *11th International Conference on Pressure Surges* (pp. 401–443). Virtual PiE Led t/a BHR Group.

Alkins, R., & Hynynen, K. (2014). Ultrasound Therapy. In *Comprehensive Biomedical Physics* (pp. 153–168). Elsevier. https://doi.org/10.1016/B978-0-444-53632-7.01010-8

Amado-Rey, A. B., Goncalves Seabra, A. C., Becker, F. J., Fournelle, M., & Stieglitz, T. (2021). Extraction of Radial-Artery Strain and Stiffness by using Non-invasive Ultrasound and a Low-Power Peak Detector. *IEEE Sensors Letters*, *5*(8), Article 7002904. https://doi.org/10.1109/LSENS.2021.3096640

Analog Devices Inc. (2021). *LTSpice XVII* (Version v.17.0.28.0,) [Computer software].

Arakawa, T. (2018). Recent Research and Developing Trends of Wearable Sensors for Detecting Blood Pressure. *Sensors (Basel, Switzerland)*, *18*(9), Article 2772. https://doi.org/10.3390/s18092772

Armstrong, M. K., Schultz, M. G., Picone, D. S., Black, J. A., Dwyer, N., Roberts-Thomson, P., & Sharman, J. E. (2019). Brachial and Radial Systolic Blood Pressure Are Not the Same. *Hypertension (Dallas, Tex. : 1979)*, *73*(5), 1036–1041. https://doi.org/10.1161/HYPERTENSIONAHA.119.12674

Autodesk Inc. (2020). *Autodesk EAGLE* (Version v.9.6.2) [Computer software]. USA.

Baltgaile, G. (2012). Arterial Wall Dynamics. *Perspectives in Medicine*, *1*(4), 146–151. https://doi.org/10.1016/j.permed.2012.02.049

Bramwell, J. C., & Hill, A. V. (1922). The Velocity of Pulse Wave in Man. *Proceedings of the Royal Society of London. Series B, Containing Papers of a Biological Character*, *93*(652), 298–306. https://doi.org/10.1098/rspb.1922.0022

Charlton, P. H., Mariscal Harana, J., Vennin, S., Li, Y [Ye], Chowienczyk, P., & Alastruey, J. (2019). Modeling Arterial Pulse Waves in Healthy Aging: A Database for In Silico Evaluation of Hemodynamics and Pulse Wave Indexes. *American Journal of Physiology. Heart and Circulatory Physiology*, *317*(5), H1062-H1085. https://doi.org/10.1152/ajpheart.00218.2019

Chen, W.-K. (2005). *The Electrical Engineering Handbook*. Elsevier Academic Press.

Chen, Y [Ying], Zhang, Y., Liang, Z., Cao, Y., Han, Z., & Feng, X. (2020). Flexible Inorganic Bioelectronics. *Npj Flexible Electronics*, *4*(1). https://doi.org/10.1038/s41528-020-0065-1

Cho, D., Kim, J., Jeong, P., Shim, W., Lee, S. Y., Choi, Y., & Jung, S. (2020). Highly Integrated Elastic Island-Structured Printed Circuit Board with Controlled Young's Modulus for Stretchable Electronics. *Micromachines*, *11*(6). https://doi.org/10.3390/mi11060617

Dagdeviren, C., Joe, P., Tuzman, O. L., Park, K.-I., Lee, K. J., Shi, Y., Huang, Y., & Rogers, J. A. (2016). Recent Progress in Flexible and Stretchable Piezoelectric Devices for Mechanical Energy Harvesting, Sensing and Actuation. *Extreme Mechanics Letters*, *9*(1), 269–281. https://doi.org/10.1016/j.eml.2016.05.015

Demirkan, I., Unlu, M. B., & Bilen, B. (2019). Determining Sodium Diffusion Through Acoustic Impedance Measurements using 80 MHz Scanning Acoustic Microscopy: Agarose Phantom Verification. *Ultrasonics*, *94*, 10–19. https://doi.org/10.1016/j.ultras.2018.12.013

Ding, X., & Zhang, Y.-T. (2019). Pulse Transit Time Technique for Cuffless Unobtrusive Blood Pressure Measurement: From Theory to Algorithm. *Biomedical Engineering Letters*, *9*, 37–52. https://doi.org/10.1007/s13534-019-00096-x

Diodes Incorporated. (2015). *ZHCS2000: 40V Surface Mount Schottky Barrier Diode*. https://www.diodes.com/assets/Datasheets/ZHCS2000.pdf

Dukhin, A. S., & Goetz, P. J. (2010). *Characterization of Liquids, Nano- and Microparticulates, and Porous Bodies using Ultrasound* (2nd ed.). *Studies in interface science: Vol. 24*. Elsevier. http://site.ebrary.com/lib/alltitles/docDetail.action?docID=10417641

Esper, S. A., & Pinsky, M. R. (2014). Arterial Waveform Analysis. *Best Practice & Research. Clinical Anaesthesiology*, *28*(4), 363–380. https://doi.org/10.1016/j.bpa.2014.08.002

Ewy, G. A., Rios, J. C., & Marcus, F. I. (1969, May). The Dicrotic Arterial Pulse. *Circulation*, *39*(5). https://doi.org/10.1161/01.CIR.39.5.655

Feldman, M. K., Katyal, S., & Blackwood, M. S. (2009). Us Artifacts. *Radiographics : A Review Publication of the Radiological Society of North America, Inc*, *29*(4), 1179–1189. https://doi.org/10.1148/rg.294085199

GAMPT mbH. (2020). *Zentrifugalpumpe MultiFlow.*

Gao, M., Rose, W. C., Fetics, B., Kass, D. A., Chen, C.-H., & Mukkamala, R. (2016). A Simple Adaptive Transfer Function for Deriving the Central Blood Pressure Waveform from a Radial Blood Pressure Waveform. *Scientific Reports*, *6*, Article 33230. https://doi.org/10.1038/srep33230

Gavish, B., & Izzo, J. L. (2016). Arterial Stiffness: Going a Step Beyond. *American Journal of Hypertension*, *29*(11), 1223–1233. https://doi.org/10.1093/ajh/hpw061

Harkness, M. L., Harkness, R. D., & McDonald, D. A. (1957). The Collagen and Elastin Content of the Arterial Wall in the Dog. *Proceedings of the Royal Society of London. Series B, Containing Papers of a Biological Character*, *146*(925), 541–551. https://doi.org/10.1098/rspb.1957.0029

Hayashi, K., Handa, H., Nagasawa, S., Okumura, A., & Moritake, K. (1980). Stiffness and Elastic Behavior of Human Intracranial and Extracranial Arteries. *Journal of Biomechanics*, *13*(2), 175–184. https://doi.org/10.1016/0021-9290(80)90191-8

Hoeks, A. P. (1993). Non-invasive Study of the Local Mechanical Arterial Characteristics in Humans. In M. E. Safar & M. F. O'Rourke (Eds.), *Developments in Cardiovascular Medicine. The Arterial System in Hypertension* (Vol. 144, pp. 119–134). Springer Netherlands. https://doi.org/10.1007/978-94-011-0900-0_9

Hoeks, A. P., Brands, P. J., Willigers, J. M., & Reneman, R. S [R. S.] (1999). Non-invasive Measurement of Mechanical Properties of Arteries in Health and Disease. *Proceedings of the Institution of Mechanical Engineers. Part H, Journal of Engineering in Medicine*, *213*(3), 195–202. https://doi.org/10.1243/0954411991534924

Honeywell International Inc. (2020). *Basic Board Mount Pressure Sensors ABP Series - Datasheet.* https://sensing.honeywell.com/honeywell-sensing-basic-board-mount-pressure-abp-series-datasheet-32305128.pdf

Huang, H., & Bednorz, T. (2014). Introducing S-parameters for Ultrasound-based Structural Health Monitoring. *IEEE Transactions on Ultrasonics, Ferroelectrics, and Frequency Control*, *61*(11), 1856–1863. https://doi.org/10.1109/TUFFC.2014.006556

Hughes, S. (2001). Medical Ultrasound Imaging. *Physics Education*, *36*(6), 468–475. https://doi.org/10.1088/0031-9120/36/6/304

Imaginant Inc. (2011). *DPR300 Ultrasonic Pulser/Receiver*. http://www.imaginant.com/dpr300

ISO 810-602:2018 (11.2018). *Non-invasive Sphygmomanometers — Part 2: Clinical Investigation of Intermittent Automated Measurement Type* (ISO ISO 810-602:2018). https://www.iso.org/standard/73339.html

Jensen, H. (1986). *Calculations for Piezoelectric Ultrasonic Transducers*. Risø National Laboratory.

Kiers, H. D., Hofstra, J. M., & Wetzels, J. F. M. (2008). Oscillometric Blood Pressure Measurements: Differences Between Measured and Calculated Mean Arterial Pressure. *The Netherlands Journal of Medicine*, *66*(11), 474–479.

Koelwyn, G. J., Currie, K. D., MacDonald, M. J., & Eves, N. D. (2012). Ultrasonography and Tonometry for the Assessment of Human Arterial Stiffness. In P. Ainslie (Ed.), *Applied Aspects of Ultrasonography in Humans.* InTech. https://doi.org/10.5772/39193

Laurent, S [Stéphane], Sharman, J., & Boutouyrie, P. (2016). Central Versus Peripheral Blood Pressure: Finding a Solution. *Journal of Hypertension*, *34*(8), 1497–1499. https://doi.org/10.1097/HJH.0000000000001000

Mahieu, D., Kips, J., Rietzschel, E. R., Buyzere, M. L. de, Verbeke, F., Gillebert, T. C., Backer, G. G. de, Bacquer, D. de, Verdonck, P., van Bortel, L. M [Luc M.], & Segers, P. (2010). Noninvasive Assessment of Central and Peripheral Arterial Pressure (Waveforms): Implications of Calibration Methods. *Journal of Hypertension*, *28*(2), 300–305. https://doi.org/10.1097/HJH.0b013e3283340a1a

The Mathworks Inc. (2021). *MATLAB* (Version v.9.10.0.1613233 (R2021a)) [Computer software]. Natick, Massachusetts.

McDonald, D. A. (1968). Regional Pulse-Wave Velocity in the Arterial Tree. *Journal of Applied Physiology*, *24*(1), 73–78. https://doi.org/10.1152/jappl.1968.24.1.73

Meinders, J. M., & Hoeks, A. P. (2004). Simultaneous Assessment of Diameter and Pressure Waveforms in the Carotid Artery. *Ultrasound in Medicine & Biology*, *30*(2), 147–154. https://doi.org/10.1016/j.ultrasmedbio.2003.10.014

Michael Margraf. (2021). *QucsStudio* (Version v.4.2.2) [Computer software]. http://qucsstudio.de

Mtcv. (2008). *File:Heart systole.svg*. https://commons.wikimedia.org/wiki/File:Heart_systole.svg

Mukherjee, R., Ghosh, S., Gupta, B., & Chakravarty, T. (2018). A Literature Review on Current and Proposed Technologies of Noninvasive Blood Pressure Measurement. *Telemedicine Journal and E-Health : The Official Journal of the American Telemedicine Association*, *24*(3), 185–193. https://doi.org/10.1089/tmj.2017.0068

Ng, A., & Swanevelder, J. (2011). Resolution in Ultrasound Imaging. *Continuing Education in Anaesthesia Critical Care & Pain*, *11*(5), 186–192. https://doi.org/10.1093/bjaceaccp/mkr030

Nirmalan, M., & Dark, P. M. (2014). Broader Applications of Arterial Pressure Wave form Analysis. *Continuing Education in Anaesthesia Critical Care & Pain*, *14*(6), 285–290. https://doi.org/10.1093/bjaceaccp/mkt078

OMICRON electronics. (2017). *Bode 100 User Manual*. https://www.omicron-lab.com/fileadmin/assets/Bode_100/Manuals/Bode-100-User-Manual-ENU10060503.pdf

Papaioannou, T. G., Protogerou, A. D., Vrachatis, D., Konstantonis, G., Aissopou, E., Argyris, A., Nasothimiou, E., Gialafos, E. J., Karamanou, M., Tousoulis, D., & Sfikakis, P. P. (2016). Mean Arterial Pressure Values Calculated Using Seven Different Methods and their Associations with Target Organ Deterioration in a Single-Center Study of 1878 Individuals. *Hypertension Research : Official Journal of the Japanese Society of Hypertension*, *39*(9), 640–647. https://doi.org/10.1038/hr.2016.41;

Park, S.-H., Lee, H. B., Yeon, S. M., Park, J., & Lee, N. K. (2016). Flexible and Stretchable Piezoelectric Sensor with Thickness-Tunable Configuration of Electrospun Nanofiber Mat and Elastomeric Substrates. *ACS Applied Materials & Interfaces*, *8*(37), 24773–24781. https://doi.org/10.1021/acsami.6b07833

Pauca, A. L., O'Rourke, M. F., & Kon, N. D. (2001). Prospective Evaluation of a Method for Estimating Ascending Aortic Pressure From the Radial Artery Pressure Waveform. *Hypertension (Dallas, Tex. : 1979)*, *38*(4), 932–937. https://doi.org/10.1161/hy1001.096106

Peng, C., Chen, M., Sim, H. K., Zhu, Y., & Jiang, X. (2021). Noninvasive and Nonocclusive Blood Pressure Monitoring via a Flexible Piezo-Composite Ultrasonic Sensor. *IEEE Sensors Journal*, *21*(3), 2642–2650. https://doi.org/10.1109/JSEN.2020.3021923

Peter, L., Noury, N., & Cerny, M. (2014). A Review of Methods for Non-invasive and Continuous Blood Pressure Monitoring: Pulse Transit Time Method is Promising? *Ingénierie Et Recherche Biomédicale*, *35*(5), 271–282. https://doi.org/10.1016/j.irbm.2014.07.002

Pico Technology Ltd. (2018). *PicoScope 5000D Series Flexible Resolution Oscilloscopes User's Guide*. https://www.picotech.com/download/manuals/picoscope-5000d-series-users-guide.pdf

Pico Technology Ltd. (2020). *PicoScope 6 User's Guide*. https://www.picotech.com/download/manuals/picoscope-6-users-guide.pdf

Poole, C., & Darwazeh, I. (2015). *Microwave Active Circuit Analysis and Design* (1st Edition). Academic Press is an imprint of Elsevier.

Rathod, V. T. (2019). A Review of Electric Impedance Matching Techniques for Piezoelectric Sensors, Actuators and Transducers. *Electronics*, *8*(2), Article 169. https://doi.org/10.3390/electronics8020169

Reneman, R. S [Robert S.], Meinders, J. M., & Hoeks, A. P. (2005). Non-invasive Ultrasound in Arterial Wall Dynamics in Humans: What Have We Learned and What Remains to be Solved. *European Heart Journal*, *26*(10), 960–966. https://doi.org/10.1093/eurheartj/ehi177

Ron Mancini (Ed.). (2002). *Op Amps for Everyone: Design Reference* (1st Edition). Texas Instruments. https://web.mit.edu/6.101/www/reference/op_amps_everyone.pdf

Rumack, C. M. (2005). *Diagnostic Ultrasound* (3rd Edition). Elsevier/Mosby.

Schäberle, W. (2011). *Ultrasonography in Vascular Diagnosis*. Springer Berlin Heidelberg. https://doi.org/10.1007/978-3-642-02509-9

Sempionatto, J. R., Lin, M., Yin, L., La Paz, E. de, Pei, K., Sonsa-Ard, T., Loyola Silva, A. N. de, Khorshed, A. A., Zhang, F., Tostado, N., Xu, S., & Wang, J [Joseph] (2021). An Epidermal Patch for the Simultaneous Monitoring of Haemodynamic and Metabolic Biomarkers. *Nature Biomedical Engineering*, *5*(7), 737–748. https://doi.org/10.1038/s41551-021-00685-1

Seo, J., Pietrangelo, S. J., Lee, H.-S., & Sodini, C. G. (2015). Noninvasive Arterial Blood Pressure Waveform Monitoring Using Two-Element Ultrasound System. *IEEE Transactions on Ultrasonics, Ferroelectrics, and Frequency Control*, *62*(4), 776–784. https://doi.org/10.1109/TUFFC.2014.006904

Sharma, M., Barbosa, K., Ho, V., Griggs, D., Ghirmai, T., Krishnan, S., Hsiai, T., Chiao, J.-C., & Cao, H. (2017). Cuffless and Continuous Blood Pressure Monitoring: A Methodological Review. *Technologies*, *5*(2), Article 21. https://doi.org/10.3390/technologies5020021

Sharman, J. E., Avolio, A. P., Baulmann, J., Benetos, A., Blacher, J., Blizzard, C. L., Boutouyrie, P., Chen, C.-H., Chowienczyk, P., Cockcroft, J. R., Cruickshank, J. K., Ferreira, I., Ghiadoni, L., Hughes, A., Jankowski, P., Laurent, S [Stephane], McDonnell, B. J., McEniery, C., Millasseau, S. C., . . . Vlachopoulos, C. (2017). Validation of Non-invasive Central Blood Pressure Devices: Artery Society Task Force Consensus Statement on Protocol Standardization. *European Heart Journal*, *38*(37), 2805–2812. https://doi.org/10.1093/eurheartj/ehw632

Soleimani, E., Mokhtari-Dizaji, M., Fatouraee, N., & Saberi, H. (2017). Assessing the Blood Pressure Waveform of the Carotid Artery Using an Ultrasound Image Processing Method. *Ultrasonography (Seoul, Korea)*, *36*(2), 144–152. https://doi.org/10.14366/usg.16019

Stanaway, J. D., & GBD 2017 Risk Factor Collaborators (2018). Global, Regional, and National Comparative Risk Assessment of 84 Behavioural, Environmental and Occupational, and Metabolic Risks or Clusters of Risks for 195 Countries and Territories, 1990–2017: A Systematic Analysis for the Global Burden of Disease Study 2017. *The Lancet*, *392*(10159), 1923–1994. https://doi.org/10.1016/S0140-6736(18)32225-6

Stergiou, G. S., Parati, G., Vlachopoulos, C., Achimastos, A., Andreadis, E., Asmar, R., Avolio, A., Benetos, A., Bilo, G., Boubouchairopoulou, N., Boutouyrie, P., Castiglioni, P., La Sierra, A. de, Dolan, E., Head, G., Imai, Y., Kario, K., Kollias, A., Kotsis, V., . . . O'Brien, E. (2016). Methodology and Technology for Peripheral and Central Blood Pressure and Blood Pressure Variability Measurement: Current Status and Future Directions - Position Statement of the European Society of Hypertension Working Group on Blood Pressure Mnitoring and Cdiovascular Vriability. *Journal of Hypertension*, *34*(9), 1665–1677. https://doi.org/10.1097/HJH.0000000000000969

Sterken, T., Vanfleteren, J., Torfs, T., Beeck, M. O. de, Bossuyt, F., & van Hoof, C. (2011). Ultra-Thin Chip Package (UTCP) and Stretchable Circuit Technologies for Wearable ECG System. In *EMBC 2011: 33rd Annual International Conference of the IEEE EMBS* (pp. 6886–6889). https://doi.org/10.1109/IEMBS.2011.6091734

Sun, C.-K. (2013). Cardio-Ankle Vascular Index (CAVI) as an Indicator of Arterial Stiffness. *Integrated Blood Pressure Control*, *6*, 27–38. https://doi.org/10.2147/IBPC.S34423

Texas Instruments. (2002). *Analysis of the Sallen-Key Architecture (Rev. B)*. https://www.ti.com/lit/pdf/sloa024

Texas Instruments. (2014). *LM7171 Very High Speed, High Output Current, Voltage Feedback Amplifier datasheet (Rev. C)*. https://www.ti.com/lit/gpn/lm7171

Tofighi, M.-R., Li, C., Schreurs, D., & Horng, T. J. (Eds.). (2017). *Principles and Aplications of RF/Microwave in Healthcare and Biosensing*. Elsevier/AP Academic Press is an imprint of Elsevier.

StatPearls Publishing (2021).

Unger, T., Borghi, C., Charchar, F., Khan, N. A., Poulter, N. R., Prabhakaran, D., Ramirez, A., Schlaich, M., Stergiou, G. S., Tomaszewski, M., Wainford, R. D., Williams, B., & Schutte, A. E. (2020). 2020 International Society of Hypertension Global Hypertension Practice Guidelines. *Hypertension (Dallas, Tex. : 1979)*, *75*(6), 1334–1357. https://doi.org/10.1161/HYPERTENSIONAHA.120.15026

van Bortel, L. M [L. M.], Balkestein, E. J., van der Heijden-Spek, J. J., Vanmolkot, F. H., Staessen, J. A., Kragten, J. A., Vredeveld, J. W., Safar, M. E [M. E.], Struijker Boudier, H. A., & Hoeks, A. P. (2001). Non-invasive Assessment of Local Arterial Pulse Pressure: Comparison of Applanation Tonometry and Echo-Tracking. *Journal of Hypertension*, *19*(6), 1037–1044. https://doi.org/10.1097/00004872-200106000-00007

van Bortel, L. M [Luc M.], Backer, T. de, & Segers, P. (2016). Standardization of Arterial Stiffness Measurements Make Them Ready for Use in Clinical Practice. *American Journal of Hypertension*, *29*(11), 1234–1236. https://doi.org/10.1093/ajh/hpw084

Vappou, J., Luo, J., Okajima, K., Di Tullio, M., & Konofagou, E. (2011, October 18). Pulse Wave Ultrasound Manometry (PWUM): Measuring Central Blood Pressure Non-invasively. In *2011 IEEE International Ultrasonics Symposium* (pp. 2122–2125). IEEE. https://doi.org/10.1109/ULTSYM.2011.0526

Wang, C [Chonghe], Li, X., Hu, H., Zhang, L [Lin], Huang, Z., Lin, M., Zhang, Z., Yin, Z., Huang, B., Gong, H., Bhaskaran, S., Gu, Y., Makihata, M., Guo, Y., Lei, Y., Chen, Y [Yimu], Wang, C [Chunfeng], Li, Y [Yang], Zhang, T., . . . Xu, S. (2018). Monitoring of the Central Blood Pressure Waveform via a Conformal Ultrasonic Device. *Nature Biomedical Engineering*, *2*(9), 687–695. https://doi.org/10.1038/s41551-018-0287-x

Westerhof, N., Stergiopulos, N., Noble, M. I. M., & Westerhof, B. E. (2010). Wave Travel and Pulse Wave Velocity. In N. Westerhof, N. Stergiopulos, M. I. M. Noble, & B. E. Westerhof (Eds.), *Snapshots of Hemodynamics: An Aid for Clinical Research and Graduate Education* (Vol. 71, pp. 165–173). Springer International Publishing. https://doi.org/10.1007/978-3-319-91932-4_21

Widman, E., Maksuti, E., Amador, C., Urban, M. W., Caidahl, K., & Larsson, M. (2016). Shear Wave Elastography Quantifies Stiffness in Ex Vivo Porcine Artery with Stiffened Arterial Region. *Ultrasound in Medicine & Biology*, *42*(10), 2423–2435. https://doi.org/10.1016/j.ultrasmedbio.2016.05.021

Wolbarst, A. B., Wyant, A. R., & Capasso, P. (2013). *Medical imaging: Essentials for Physicians*. John Wiley & Sons.

World Health Organization. (2021). *Hypertension*. https://www.who.int/news-room/fact-sheets/detail/hypertension

Yamashita, Y., Hosono, Y., & Itsumi, K. (2007). Low Sound Velocity and Acoustic Attenuation Silicone Rubber Lens Based on Nano-Powder-Composite for Medical Echo Ultrasound Array Probes. In *2007 Sixteenth IEEE International Symposium on the Applications of Ferroelectrics* (pp. 752–753). IEEE. https://doi.org/10.1109/ISAF.2007.4393391

APPENDIX

A1   List of publications

A1.1   Article 1

Authors: A. B. Amado-Rey; A. C. Gonçalves Seabra; F. J. Becker; M. Fournelle; T. Stieglitz

Title: Blood Pressure Models for Wearable Sensors

Abstract: Ultrasound (US) is one of the newest methods used to measure critical arterial parameters, such as blood pressure (BP). Continuous, non-invasive, and accurate measurements are very attractive for the patient and clinicians. US sensors developed up to now extract non-invasively BP by using algorithms based on a constant brachial stiffness, leading to wrong values. Due to the nonlinear viscoelasticity properties of the radial-artery, high variations on the strain and stiffness of this artery during one cardiac cycle are expected. Thus, in this letter, stiffness measurements of a mimicked radial artery are performed by using a custom fabricated US-sensor and the high influence of the stiffness variations in the systolic and diastolic BP values is demonstrated. For this purpose, an accurate 5 MHz piezo transducer, made of lead zirconate titanate, has been used. Thanks to a high accurate and ultra-broadband (1 KHz–30 MHz) modeling of the piezo based on a multiresonant Butterworth-Van-Dyke model, a high-speed and high-gain peak detector could be developed. This US system allows for continuous and non-invasive measurement of the strain and stiffness of the radial artery, which determine the biological age of the vascular tree and deliver a more relevant predictive maker of cardiovascular events and changes than brachial BP.

A1.2   Article 2

Authors: A. C. Seabra; A. F. Silva; T. Stieglitz; A. B. Amado-Rey

Title: Blood Pressure Models for Wearable Sensors

Journal: IEEE Sensors Journal

Abstract: As cardiovascular diseases are one of the most prominent illnesses, a continuous, non-invasive, and comfortable monitoring of blood pressure (BP) is indispensable. This paper investigates the best method for obtaining highly accurate BP values in non-invasive measurements when using an ultrasound (US) sensor projected for a wrist-worn device. State-of-the-art BP models were analysed and qualitatively compared. Relevant arterial parameters such as luminal area, flow velocity and pulse wave velocity, of 729 subjects were extracted from a computer simulated database and served as input parameters for the wearable US. A linear *in-silico* model calibrated to each arterial-site revealed to be most accurate model. The linear model was used for the extraction of BP by using the US sensor and validated with a commercial pressure sensor in an *ex-vivo* experimental setup. The results showed an *in-silico* pulse pressure correlation of 0.978 and mean difference of (-2.134 ± 2.477) mmHg at the radial artery and *ex-vivo* pressure correlation of 0.994 and mean difference of (0.554 ± 2.315) mmHg. Thus, with the linear model, the US measurement complies with the Association for the Advancement of Medical Instrumentation standard with deviations lower than 5 mmHg.

A2   Acoustic impedance

The density, speed of sound and acoustic impedance of a selection of materials of interest for this thesis are shown in Table A.1.

Table A.1: Density, speed of sound and acoustic impedance of a selection of materials.

Material	Density ($10^3 \cdot kg \cdot m^{-3}$)	Speed of sound ($m \cdot s^{-1}$)	Acoustic impedance (MRayl)	Ref.
Air	0.0012	330	0.0004	(Hughes, 2001)
Water	1	1430	1.43	(Hughes, 2001)
DI-water	-	-	1.48	(Alkins & Hynynen, 2014)
Blood	1.60	1050	1.68	(Wolbarst et al., 2013)
Soft tissue	1.10	1540	1.69	(Hughes, 2001)
Fat	0.95	1450	1.38	(Hughes, 2001)
Bone	1.91	4080	7.8	(Hughes, 2001)
Silicone	1.54	919	1.42	(Yamashita et al., 2007)
Saline solution (0.9 w/w%)	-	-	1.67	(Demirkan et al., 2019)

A3   Operational amplifiers design techniques

A3.1   Non-inverting amplifier

In a non-inverting amplifier configuration, the input signal is directly introduced in the OpAmp's positive port and negative feedback is provided through a voltage divider network (composed of R_f and R_g) to the negative port of the OpAmp, as shown in Figure A.1. The configuration produces an output in-phase with the input signal, and a gain (G) defined by Equation A.1.
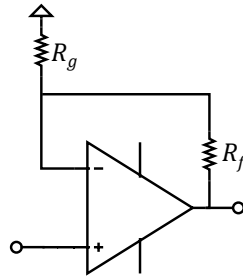
Figure A.1: Non-inverting amplifier configuration.

$$G = 1 + \frac{R_g}{R_f} \qquad \text{(A.1)}$$

A3.2   Bandpass filter Sallen-key topology

The Sallen-key bandpass filter configuration is shown in Figure A.2. The circuit constitutes of three stages: the high pass filter stage, amplification, and low pass filter stage. The bandpass mid-frequency (f_m) is calculated by Equation A.2. The filter design is based on a non-inverting OpAmp configuration, so that the filter's inner gain G is constant and defined by Equation A.1. However, due to the circuit's unique configuration, the gain can exhibit a resonant peak in the mid-frequency. The peak's height and narrowness are dependent on the quality factor Q, determined by Equation A.3. The gain at mid-frequency (A_m) is proportional to the quality factor and can be calculated through Equation A.4. Care must be taken when G approaches the value of 3, because $A_m \rightarrow \infty$ and the circuit starts to oscillate.
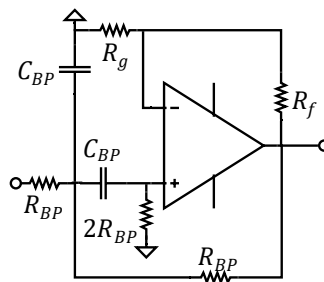

Figure A.2: Sallen-key bandpass filter configuration.

$$f_m = \frac{1}{2 \cdot \pi \cdot R_{BP} \cdot C_{BP}} \qquad \text{(A.2)}$$

$$Q = \frac{1}{3 - G} \tag{A.3}$$

$$A_m = Q \cdot G \tag{A.4}$$

A4   Echo receiver PCB

The schematic of the echo receiver PCB is shown in Figure A.3. When compared to Figure 5.1 in Section 5.1, the output of the non-inverting amplifier (see Figure 5.1A) is measured at the test point TP1, the output of the non-inverting amplifier (see Figure 5.1B) at TP2, the output of the bandpass filter (see Figure 5.1C) at TP3. Additionally, the output of the DC return path is measured at TP4. In Figure A.3B, the implemented dual supply circuit (developed in previous works) is shown.
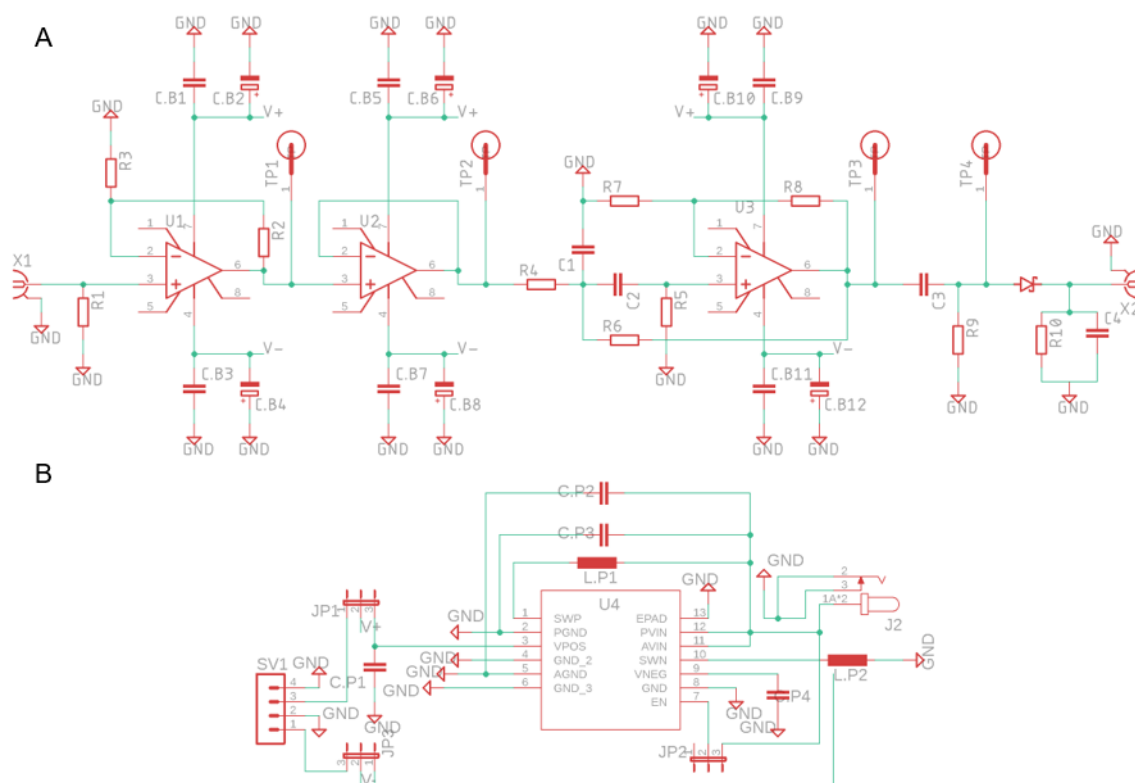
Figure A.3: Schematic of the echo receiver PCB. (A) Schematic of the developed echo receiver PCB with the output of the non-inverting amplifier at TP1, the output of the buffer at TP2, the output of the bandpass filter at TP3 and output of the DC return path at TP4. (B) Schematic of the dual supply circuit used (developed in previous works).

The complete BoM used in the echo receiver PCB is listed in Table A.2. The table is an extension of Table 2, where only the main components were listed. Bypassing capacitors, as well as components for the dual voltage supply, introduced from previous work, are listed.

Table A.2: Complete BoM of the developed echo receiver PCB.

Part	Value	Part	Value	Part	Value
C.B1	0.01 µF	C1	4.8 pF	R6	820 Ω
C.B2	2.2 µF	C2	10 pF	R7	16.2 kΩ
C.B3	0.01 µF	C3	1 µF	R8	2.49 kΩ
C.B4	2.2 µF	C4	2 nF	R9	150 Ω
C.B5	0.1 µF	D1	ZHCS1000	R10	150 Ω
C.B6	2.2 µF	J2	PJ-002AH-SMT-TR	SV1	MA04-1
C.B7	0.01 µF	JP1	Jumper	TP1	5019
C.B8	2.2 µF	JP2	Jumper	TP2	5019
C.B9	0.01 µF	JP3	Jumper	TP3	5019
C.B10	2.2 µF	L.P1	4.7 µH	TP4	5019
C.B11	0.01 µF	L.P2	4.7 µH	U1	LM7171A
C.B12	2.2 µF	R1	180 Ω	U2	LM7171A
C.P1	10 µF	R2	470 Ω	U3	LM7171A
C.P2	100 nF	R3	47 Ω	U4	TPS65133
C.P3	10 µF	R4	10 kΩ	X1	SMA
C.P4	10 µF	R5	30 kΩ	X2	SMA

A5   Echo receiver with variable gain

The degree of attenuation of the US signal depends on the characteristics of the tissue in which the wave propagates. As the body fat and tissue composition changes between individuals, the characteristics of the echoes, especially of the amplitude of the signal, is expected to be different. A device that could adapt and take into account these changes would be more accurate when tested in different people. Therefore, a revised version of the echo receiver circuit was developed, in which a variable gain amplifier replaced the simple amplifier previously used. The circuit design and PCB fabrication are described in this section. Due to time restraints, the characterization and validation of the board are not included in this work.

The echo receiver circuit consists of four stages, as seen in the simplified schematic in Figure A.4 (the complete schematic of the circuit and BoM is shown in Figure A.5 and Table A.3, respectively). At the input, the received echo signal is filtered by a bandpass filter. Next, the signal is amplified by a variable gain amplifier. Following, a buffer is needed for impedance matching to the next and final stage of the circuit, an amplitude-modulated peak detector, where the maximum of the signal is extracted through a half-wave rectifier.
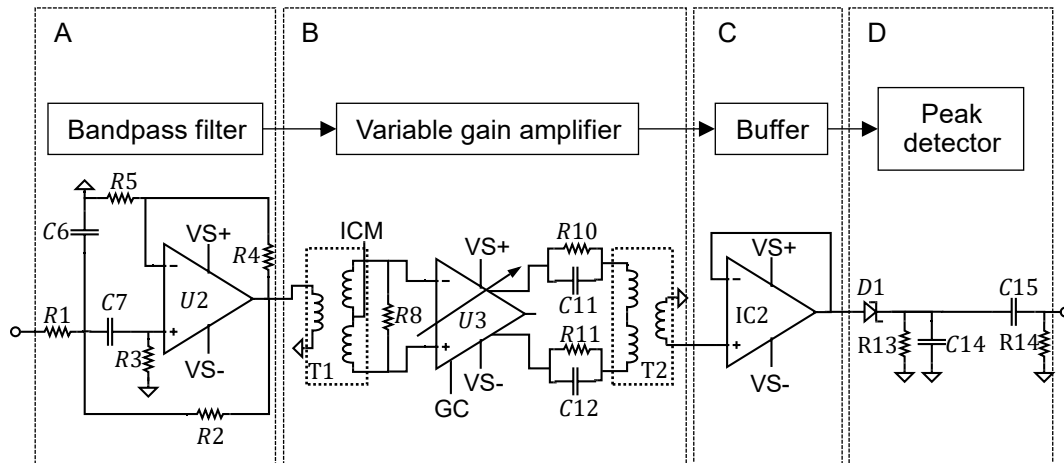
Figure A.4: Simplified schematic of the second version of the echo receiver circuit. The circuit is composed of four stages: (A) bandpass filter, (B) variable gain amplifier, (C) buffer, and (D) peak detector.

Bandpass filter

The first stage of the reviewed circuit is a second-order bandpass filter, shown in Figure A.4A, with an equal configuration to the one used in the first version of the circuit, the Sallen-Key topology. The configuration of the filter was optimized until a mid-frequency of 5 MHz was achieved.

Variable gain amplifier

The second stage is the variable gain amplifier, shown in Figure A.4B, with input and output baluns (ADT1-1WT, Mini-Circuits). The input balun is used for converting the filtered signal into differential signals with a 180° phase difference. The differential signals are taken as the input of the variable gain amplifier, the THS7530 (Texas Instruments, 2020), chosen due to its high-speed, high-bandwidth gain control, output common-control, and output voltage clamping. The gain varies linearly from 11.6 dB to 46.5 dB, controlled by the analogue input GC (see Figure A.4B) from 0 to 0.9 V. As the output of the variable gain amplifier is differential, the output balun is used in the opposite configuration of the input balun, and converts the outputs of the integrated circuit into an unbalanced signal.

Buffer

A buffer (Figure A.4C) was introduced between the variable gain amplifier and the peak detector for impedance matching and isolation between the two stages. The BUF634A (Texas Instruments, 2021) was chosen due to its high slew rate.

Modified peak detector

The fourth and last stage of the echo receiver circuit is shown in Figure A.4D. The high-frequency peak detector configuration was the same as used in the first version of the circuit. However, the DC return-path was placed after the peak detector circuit and not before as it had been previously designed. Additionally, the Schottky diode component was changed to the BAT54WS (Micro Commercial Components, 2020), due to its smaller continuous forward current.

Power supply

A common power supply of ± 5 V was applied to the three integrated circuits. The power supply can be applied in two ways, by using external ± 5 V or by applying only +5 V and using an internal voltage converter and simplifying the necessary external voltage supply. To accomplish the latter, a new dual-supply block was introduced composed of a voltage regulator and voltage converter, granting an external supply of +5 V and internal conversion into -5 V necessary for powering the bandpass filter and buffer stages. The LT1761ES5-5 (Linear Technology, 2005) was used as the 5V regulator and the ICL7660S (Renesas, 2013) as the voltage converter. Power supply bypass was necessary to guarantee low DC-impedance and high impedance response for the AC working frequency (Texas Instruments, 2014).

The schematic of the echo receiver PCB is shown in Figure A.5. When compared to Figure A.4, the output of the bandpass filter (see Figure A.4A) is measured at the test point TP2, the output of the voltage gain amplifier (see Figure A.4B) at TP5, and the output of the peak detector (see Figure A.4D) at TP7. Notice that the newly developed dual supply circuit is displayed in Figure A.5A.
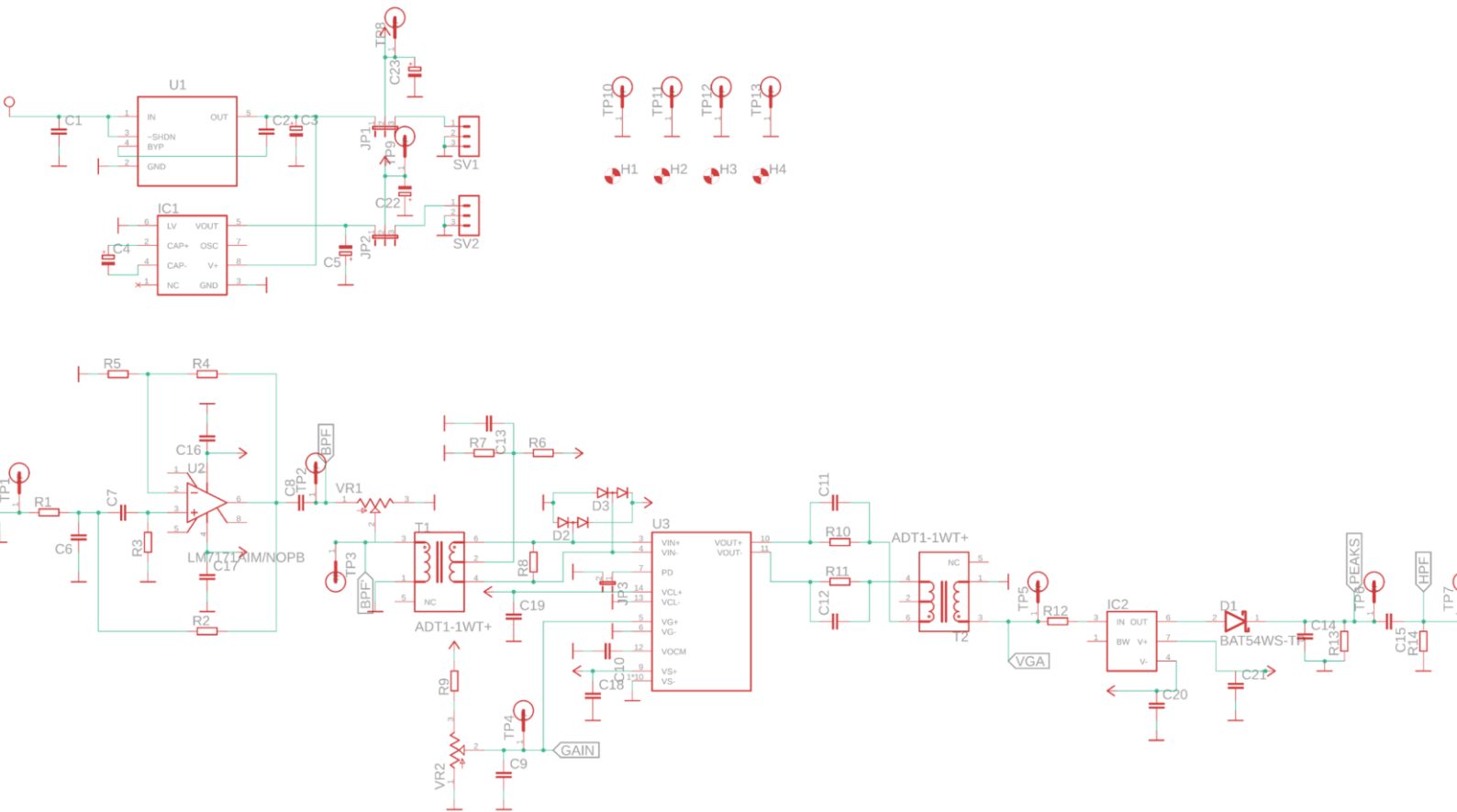
A.5: Schematic of the second version of the echo receiver PCB. (A) Schematic of the dual supply circuit, with grounded test points and mounting holes. (B) Shematic [...] d version of the developed echo receiver with the output of the bandpass filter at TP2, the output of the variable gain amplifier at TP5, and the output of the modified [...] or at TP7.

Table A.3: Complete BoM of the second version of the echo receiver PCB.

Part	Value	Part	Value	Part	Value
C1	1 µF	D3	BAV199	R14	1 kΩ
C2	0.01 µF	H1	MOUNT-HOLE	SV1	MA03-1
C3	10 µF	H2	MOUNT-HOLE	SV2	MA03-1
C4	10 µF	H3	MOUNT-HOLE	T1	MINI-CIRCU
C5	10 µF	H4	MOUNT-HOLE	T2	MINI-CIRCU
C6	15 pF	IC1	ICL7660CSA	TP1	5019
C7	15 pF	IC2	BUF634U	TP2	5019
C8	1 µF	INPUT	SMA-142-07	TP3	5019
C9	0.1 µF	JP1	Jumper	TP4	5019
C10	0.1 µF	JP2	Jumper	TP5	5019
C11	39 pF	JP3	Jumper	TP6	5019
C12	39 pF	OUTPUT	SMA-142-07	TP7	5019
C13	0.1 µF	R1	2 kΩ	TP8	5019
C14	2.2 nF	R2	2 kΩ	TP9	5019
C15	1 µF	R3	4.02 kΩ	TP10	5019
C16	0.01 µF	R4	1 kΩ	TP11	5019
C17	0.01 µF	R5	2 kΩ	TP12	5019
C18	0.1 µF	R6	1 kΩ	TP13	5019
C19	0.1 µF	R7	1 kΩ	U1	LT1761ES5-
C20	0.1 µF	R8	50 Ω	U2	TI_NATIONA
C21	0.1 µF	R9	3.92 kΩ	U3	THS7530PWP
C22	6.8 µF	R10	24.9	VR1	3362P-1-10
C23	6.8 µF	R11	24.9	VR2	3362P-1-10
D1	BAT54W	R12	50 Ω		
D2	BAV199	R13	150 Ω		

The PCB of the second version of the echo receiver circuit was produced following the same process as the first version. The total PCB area is 58×81 mm^2. Figure A.6 shows the final product.

1 cm

Figure A.6: Photograph of the second version of the echo receiver board.

A6   PicoScope sampling rate/ADC resolution study

Each frame recorded by the PicoScope is composed of two different signals, the US echo signal and the voltage reading from the piezoresistive pressure sensor. On one hand, the diameter resolution from each frame, extracted from the TOF between the maximum voltage peaks of the set reflection windows, is defined by the sampling rate of the PicoScope. On the other hand, the resolution of the voltage reading for pressure conversion depends on the ADC resolution (the number of bits) set in the PicoScope. It should be noted that the diameter resolution depends upon the value of velocity used in the calculation's and it should correspond to the speed of sound of the medium in which the US wave is propagating. During this work, the velocity of sound in DI-water was used (experimentally determined in A7). Furthermore, the voltage resolution, and corresponding pressure resolution, depends on the voltage range set in the PC-oscilloscope. A voltage range of ±5 V was sufficient. Equation A.5 and Equation A.6 indicate each resolution calculation. The PC-oscilloscope has the function of adapting the hardware resolution and sampling rate to its user's needs. A study of the compromise between the diameter's and pressure's resolution to each ADC resolution and the corresponding maximum sampling rate is shown in Figure A.7.

$$Diameter\ resolution = \frac{c \cdot (sampling\ frequency)^{-1}}{2} \qquad \text{(A.5)}$$

$$Voltage\ resolution = \frac{(Voltage\ range) \cdot 2}{2^{n\ bits}} \qquad \text{(A.6)}$$
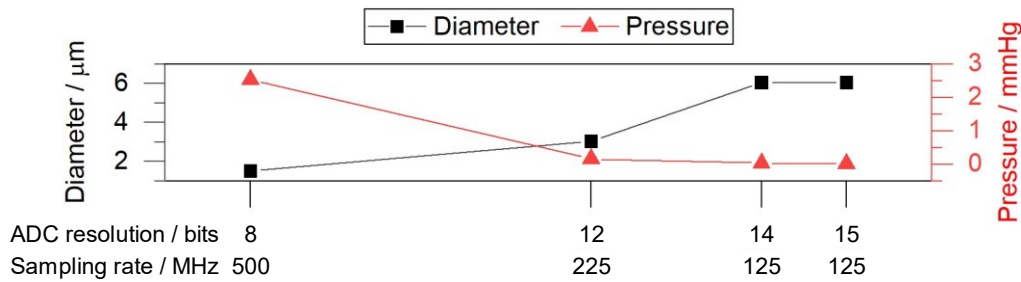
Figure A.7: PicoScope resolution study. The maximum sampling rate to each ADC resolution is shown on the x-axis. The left y-axis shows the diameter resolution (to a speed of sound in DI-water) and the right y-axis the pressure resolution (to a voltage range of ±5 V). The pair of maximum resolution in the PicoScope is plotted.

The PicoScope resolution pair of 8 bits and 500 MHz was chosen, corresponding to 1.513 µm of diameter resolution and 2.525 mmHg of pressure resolution. This configuration provides the best resolution for the diameter measurement and still a good pressure resolution. It should be noted that the calculated diameter curve is then converted to a pressure reading, being that the resolution of the diameter reading takes part in defining the resolution of the derived pressure.

A7   Speed of sound in distilled water

The speed of sound in distilled water was measured with two multifrequency probes (Multifrequenzsonde, GAMPT mbH, Merseburg, Germany). A container of 100 mm in width was filled with DI-water and placed in-between the probes that were mounted on acrylic supports. Ultrasound gel was used to dampen the acoustic impedance between the materials. A 5 MHz burst signal (produced by the signal generator Keysight 33500Bseries) was introduced in the first probe, which sent an ultrasound signal through the container. The second probe received the US waves, which converted it into an electrical signal. The burst and converted signal were acquired by an oscilloscope (DLM2024, Yokogawa Test & Measurement Corporation, Tokyo, Japan) and post-processed offline. The velocity was calculated by diving the distance between the probes (width of the container) by the TOF between the signals. A value of 1,513.226 m/s of the speed of sound in DI-water was determined.